UNIVERSITY OF CALIFORNIA, SAN DIEGO

First-principles investigation of defects and interfaces in rutile, perovskite, and fluorite-structured metal oxides

A dissertation submitted in partial satisfaction of the
requirements for the degree
Doctor of Philosophy

in

NanoEngineering

by

Maziar Behtash

Committee in charge:

Professor Kesong Yang, Chair
Professor Prabhakar R. Bandaru
Professor Jian Luo
Professor Shyue Ping Ong
Professor Francesco Paesani

2018

The dissertation of Maziar Behtash is approved, and it is acceptable in quality and form for publication on microfilm and electronically:

_____

_____

_____

_____

_____

Chair

University of California, San Diego

2018

TABLE OF CONTENTS

LIST OF FIGURES

LIST OF TABLES

ACKNOWLEDGEMENTS

I would like to express my gratitude to my thesis advisor, Professor Kesong Yang, for teaching me so very much on this journey. You were always willing to help, always ready with new ideas or suggestions that struck at the heart of matter. I have learned much more than I thought possible, and I thank you for it. Graduate study is rewarding and inspiring, but also often a humbling experience. Through it all, you were patient, generous, and kind. It has been my honor to work with you. I thank Professor Jian Luo for the opportunity to work on a Laboratory-University Collaboration with the Army Research Laboratory, and for helping me ground my theoretical results in experimental reality. I would like to thank my Committee Members, Professor Prabhakar R. Bandaru, Professor Jian Luo, Professor Shyue Ping Ong, and Professor Francesco Paesani for their support and advice in the completion of this thesis.

I thank Dr. Safdar Nazir, Dr. Jianli Cheng, Paul Joo, Dr. Shengfeng Yang, Camille Bernal, Dr. Yaqin Wang, and Yuheng Li. Much of the work in this thesis would not have been possible without the many conversations and collaborations we have shared. I thank my fellow graduate students and friends in the Yang Group for making this experience what it has been. More importantly, I thank you for your friendship. I greatly look forward to spending time with you once again, years from now, and looking back on our days as students in the pods at SME.

I thank my Mother and Father for giving me the determination to never give up. I thank you for your advice and unwavering support. I hope to make you as proud as you have made me.

I thank my spectacular wife Erica for keeping me going in these years of study. You have been with me every step of the way, in the best times and the worst. Your warmth, compassion, and intelligence have inspired me more than you know. I could not imagine a better woman on my team.

Chapter 2, in full, is a reprint of the material “Electronic Structures and Formation Energies of Pentavalent-Ion-Doped SnO_2: First-Principles Hybrid Functional Calculations” as it appears in the Journal of Applied Physics. Maziar Behtash, Paul Hyunggyu Joo, and Kesong

Yang, 117, 175101, (2015). The dissertation author was the primary investigator and author of this paper.

Chapter 3, in full, is a reprint of the material "Nb and Ta Layer Doping Effects on the Interfacial Energetics and Electronic Properties of $LaAlO_3/SrTiO_3$ Heterostructure: First-Principles Analysis" as it appears in Physical Chemistry Chemical Physics. Safdar Nazir, Maziar Behtash, Jianli Cheng, Jian Luo, and Kesong Yang, 18, 2379-2388, (2016). The dissertation author was a co-author of this paper.

Chapter 4, in full, is a reprint of the material "Polarization Effects on the Interfacial Conductivity in the $LaAlO_3/SrTiO_3$ Heterostructure: First-Principles Study" as it appears in Physical Chemistry Chemical Physics. Maziar Behtash, Safdar Nazir, Yaqin Wang, and Kesong Yang, 18, 6831-6838, (2016). The dissertation author was the primary investigator and author of this paper.

Chapter 5, in full, is a reprint of the material "Oxygen Vacancy Formation in the $SrTiO_3$ $\Sigma 5$ [001] Twist Grain Boundary from First-principles" as it appears in the Journal of the American Ceramic Society. Maziar Behtash, Yaqin Wang, Jian Luo, and Kesong Yang, 101, 3118-3129, (2018). The dissertation author was the primary investigator and author of this paper.

Chapter 6, in full, is current being submitted for publication of the material "First-Principles Study of Substitutional Impurity Segregation in Zirconia, Hafnia, and Yttria-Stabilized-Zirconia Grain Boundaries". Maziar Behtash, Jian Luo, and Kesong Yang. The dissertation author was the primary investigator and author of this paper.

VITA

2010	B. S. in BioEngineering, University of California, Berkeley
2014	M. S. in NanoEngineering, University of California, San Diego
2015-2017	Teaching Assistant, University of California, San Diego
2013-2018	Research Assistant, University of California, San Diego
2018	Ph. D. in NanoEngineering, University of California, San Diego

AWARDS AND HONORS

2016	Graduate Student Association Travel Grant Award, University of California, San Diego
2016	Achievement Reward for College Scientists Foundation Fellowship, San Diego Chapter
2018	Graduate Student Association Travel Grant Award, University of California, San Diego

PUBLICATIONS

1 **Maziar Behtash**, Jian Luo, and Kesong Yang, "First-Principles Study of Impurity Segregation in Zirconia, Hafnia, and Yttria-Stabilized-Zirconia Grain Boundaries", *submitted*, (2018).

2 **Maziar Behtash**, Yaqin Wang, Jian Luo, and Kesong Yang, "Oxygen Vacancy Formation in the $SrTiO_3$ $\Sigma 5$ [001] Twist Grain Boundary from First-principles", *Journal of the American Ceramic Society*, 101, 3118, (2018).

3 **Maziar Behtash**, Safdar Nazir, Yaqin Wang, and Kesong Yang, "Polarization Effects on the Interfacial Conductivity in the $LaAlO_3$/$SrTiO_3$ Heterostructure: First-Principles Study", *Physical Chemistry Chemical Physics* 18, 6831, (2016).

4 **Maziar Behtash**, Paul Hyunggyu Joo, Safdar Nazir and Kesong Yang, "Electronic Structures and Formation Energies of Pentavalent-Ion-Doped SnO_2: First-Principles Hybrid Functional Calculations", *Journal of Applied Physics*, 117, 175101, (2015).

5 Yuheng Li, Maziar Behtash, Joseph Wong, and Kesong Yang, "Enhancing Ferroelectric Dipole Ordering in Organic-Inorganic Hybrid Perovskite $CH_3NH_3PbI_3$: Strain and Doping Engineering", *Journal of Physical Chemistry C*, 122, 177, (2018).

6 Yaqin Wang, Jianli Cheng, Maziar Behtash, Wu Tang, Jian Luo, and Kesong Yang, "First-Principles Studies of Polar Perovskite $KTaO_3$ Surfaces: Structural Reconstruction, Charge Compensation, and Stability Diagram", *Physical Chemistry Chemical Physics*, 20, 18515, (2018).

7 Yaqin Wang, Wu Tang, Jianli Cheng, Maziar Behtash, and Kesong Yang, "Creating Two-Dimensional Electron Gas in Polar/Polar Perovskite Oxide Heterostructures: First-Principles Characterization of $LaAlO_3/A^{+}B^{5+}O_3$", *ACS Applied Materials & Interfaces*, 8, 13659, (2016).

8 Kesong Yang, Safdar Nazir, Maziar Behtash, and Jianli Cheng, "High-Throughput Design of Two-Dimensional Electron Gas Systems Based on Polar/Nonpolar Perovskite Oxide Heterostructures", *Scientific Reports* 6, 34667, (2016).

9 Safdar Nazir, Maziar Behtash, Jianli Cheng, Jian Luo, and Kesong Yang, "Nb and Ta Layer Doping Effects on the Interfacial Energetics and Electronic Properties of $LaAlO_3/SrTiO_3$ Heterostructure: First-Principles Analysis", *Physical Chemistry Chemical Physics*, 18, 2379, (2016).

10 Paul Hyunggyu Joo, Maziar Behtash, and Kesong Yang, "Energetic Stability, Oxidation States, and Electronic Structure of Bi-doped $NaTaO_3$: First-Principles Hybrid Functional Study", *Physical Chemistry Chemical Physics* 18, 857, (2016).

11 Safdar Nazir, Jianli Cheng, Maziar Behtash, Jian Luo, and Kesong Yang, "Interface Energetics and Charge Carrier Density Amplification by Sn-doping in $LaAlO_3/SrTiO_3$ Heterostructure", *ACS Applied Materials & Interfaces*, 7, 14294-14302, (2015).

12 Safdar Nazir, Maziar Behtash and Kesong Yang, "The Role of Uniaxial Strain in Tailoring Interfacial Properties of $LaAlO_3/SrTiO_3$ Heterostructure", *RSC Advances* 5, 15682, (2015).

13 Safdar Nazir, Maziar Behtash and Kesong Yang, "Towards Enhancing Two-Dimensional Electron Gas Quantum Confinement Effects in Perovskite Oxide Heterostructures", *Journal of Applied Physics*, 117, 115305, (2015).

14 Safdar Nazir, Maziar Behtash and Kesong Yang, "Enhancing Interfacial Conductivity and Spatial Charge Confinement of $LaAlO_3/SrTiO_3$ Heterostructures via Strain Engineering", *Applied Physics Letters* 105, 141602, (2014).

ABSTRACT OF THE DISSERTATION

First-principles investigation of defects and interfaces in rutile, perovskite, and fluorite-structured metal oxides

by

Maziar Behtash

Doctor of Philosophy in NanoEngineering

University of California, San Diego, 2018

Professor Kesong Yang, Chair

Defects and interfaces are ubiquitous in polycrystalline metal oxide materials, and their presence gives rise to a host of beneficial and harmful effects. In this thesis we focused on substitutional impurities, heterointerfaces, oxygen vacancies, and grain boundaries, with the goal of enhancing material properties, using first-principles density functional theory calculations.

In the first project we studied the energetic and electronic properties of pentavalent-cation-doped SnO_2 transparent conducting oxide (TCOs) materials. We found that P-doped SnO_2 (PTO), a non-toxic low-cost material, compares favorably with well-known TCOs Sb-doped SnO_2 (ATO) and Ta-doped SnO_2 (TTO). In addition, we showed that the theoretical charge carrier density (n_e)

of PTO, ATO, and TTO is nearly identical, indicating that the order-of-magnitude experimental variations in n_e for the latter two materials may instead arise from differences in experimental conditions during synthesis.

In the second project we explored the possibility of enhancing the properties of the two-dimensional electron gas (2DEG) which forms at the interface of the $LaAlO_3/SrTiO_3$ (LAO/STO) heterostructure through *n*-type layer doping with transition metal cations. We found that Ta(Nb) doping at the interfacial Ti site is energetically favorable, and can significantly enhance the charge carrier density and magnetism of the interfacial 2DEG in LAO/STO. In addition, we found that Ta(Nb) doping at the interfacial Al site can improve 2DEG charge confinement to only two TiO_2 atomic layers of the STO substrate.

In the third project we examined polarization and the effect of externally-applied strain on 2DEG properties in LAO/STO. We found that the LAO film polarization (P_{LAO}) decreases with film thickness, and that there is a critical P_{LAO} value above which 2DEG cannot form. We resolved the long-standing discrepancy between the experimental and theoretical 2DEG charge carrier density through the use of an appropriate slab model. In addition, we showed that [100] uniaxial tensile strain applied on the STO substrate can reduce P_{LAO} and thereby enhance the charge carrier density, electron mobility, and interfacial charge concentration of the LAO/STO 2DEG.

In the fourth project we studied termination stability and oxygen vacancy formation in a $\Sigma 5$ [001] twist grain boundary (GB) structure of $SrTiO_3$ (STO). We found that of the three possible GB terminations, only the SrO/SrO (S/S) and SrO/TiO_2 (S/T) can form in the chemical potential range necessary to guarantee bulk STO stability, while the TiO_2/TiO_2 (T/T) termination cannot form. We showed that oxygen vacancies tend to segregate adjacent to the GB layer in the S/S system, but at the GB layer in the S/T system. In addition, we demonstrated that oxygen vacancies form more easily in the S/T GB system than the S/S GB system, leaving the door open for possible GB engineering applications.

In the final project we considered substitutional impurity segregation to Σ5 (310)/[001] tilt grain boundary structures of ZrO_2, HfO_2, and yttria-stabilized ZrO_2 (YSZ). We discovered a fundamental difference in the characteristic segregation profiles of aliovalent and isovalent impurities which is explained by differences in the local electrostatic potential energy. We successfully generated and structurally-optimized a YSZ GB structure bearing high concentrations of yttrium dopants and oxygen vacancies. Finally, we found that Si and Ca are strong segregants in YSZ while Al, Ti, and Y are not.

Chapter 1

Introduction

Metal oxide materials play a central role in the functionality of many important technologies, from photovoltaic cells to medical implants. [14–18] Both natural and man-made metal oxides typically contain a variety of intrinsic defects, impurities, and interfaces whose presence can have very significant effects on the overall material properties. For example, transparent insulating oxide SnO_2 can become electrically conductive through *n*-type doping with as little as 1 mol% Ta. [2] The incredible influence of defects on material properties has stimulated a vast research effort over the past several decades which has aimed not only to understand these defects, but to engineer them and produce material systems with novel functionality. [19–25] In particular, defect-bearing metal oxide materials have enabled thin film material systems such as thin-film transistors, [26, 27] thin-film light-emitting diodes, [28–30] and thermal barrier coatings (TBCs) [31–33] which have revolutionized optoelectronic and aerospace technology. Further advances in the understanding of defects and interfaces at the nanoscale will no doubt lead to the discovery of materials with novel properties and unexpected applications.

Rutile, perovskite, and fluorite-structured metal oxides have drawn significant attention owing to their tremendous compositional variety and versatility of application. In this thesis our efforts center on these three materials classes, focusing on substitutional impurities, oxygen

vacancies, heterointerfaces, and/or grain boundaries. In this Chapter we will first briefly describe the structural properties and several applications of rutile, perovskite, and fluorite oxides. Next, we will discuss point defects and grain boundaries in these materials. Finally, we will describe the organization of this thesis.

1.1 Rutile, Perovskite, and Fluorite Metal Oxides

Rutile-structured metal oxides have chemical composition MO_2, where the M-site is a tetravalent transition metal or post-transition metal cation, and typically crystallize in a tetragonal structure composed of six-fold coordinated metal-oxide octahedra (see Fig. 1.1a). [34] Undoped rutile metal oxides, such as TiO_2, can serve as photocatalysts for water-splitting [35–37] or environmental remediation [38–40] owing to their wide band gaps and chemical stability. In addition, extrinsic substitutional defects (dopants) can be deliberately introduced into rutile TiO_2 to enhance its photocatalytic properties via inhibition of electron-hole recombination. [41] Doping other transparent rutile-structured insulating oxides, such as SnO_2, can produce *n*-type conductivity while preserving their transparency. [42]

Perovskite-structured metal oxides have chemical composition ABO_3, where A is an alkaline or rare-earth metal and B is a transition metal, and typically crystallize in a body-centered cubic or pseudo-cubic structure (see Fig. 1.1b). However, differences in the ionic radii of the A-site and B-site cations can lead to symmetry-breaking distortions which can in turn alter the crystal phase of the overall material to tetragonal, orthorhombic, or rhombohedral. The ionic radii of A-site and B-site cations can be related using the Goldschmidt tolerance factor ($t = r_A/(r_B\sqrt{2})$), which can predict the structural distortions in the perovskite structure with a high degree of accuracy. Specifically, $t < 1$ indicates a relatively small A-site cation which produces rotations in the BO_6 octahedra yielding an orthorhombic or rhombohedral structure; $t = 1$ indicates an ideal size A-site cation giving rise to an undistorted cubic structure; and

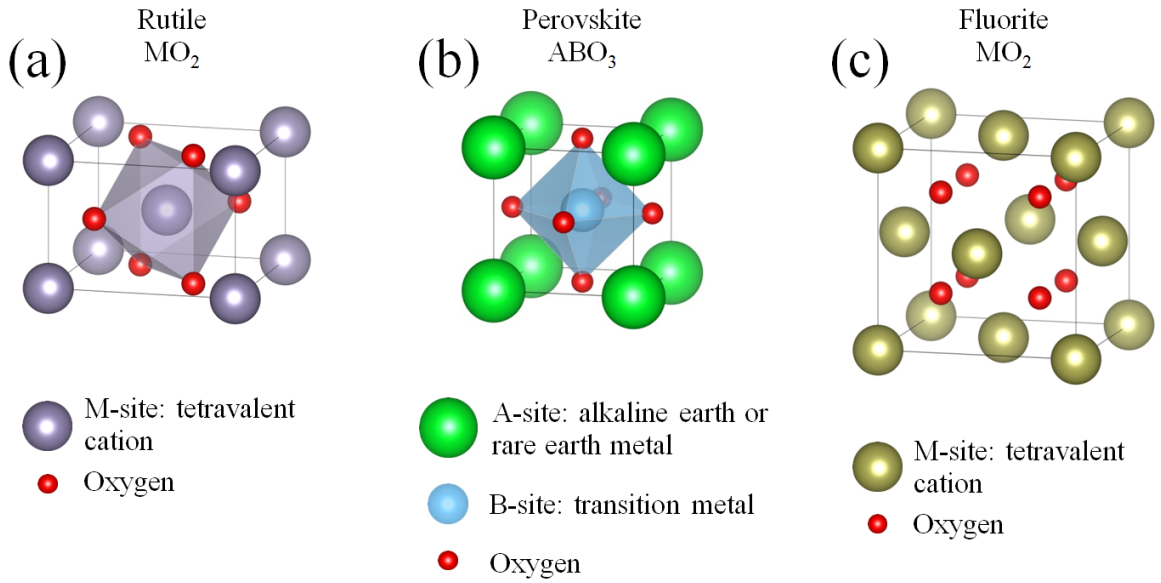

Figure 1.1: Structural schematic of the rutile (a), perovskite (b), and fluorite (c) metal oxide structures.

$t > 1$ indicates a relatively-large A-site cation which produces a lattice elongation from cubic to tetragonal. Therefore, the compositional variability of perovskite oxides leads to structural variations which in turn yield a rich landscape of materials spanning a wide range of properties. In addition, there is variability in the oxidation states of the A-site and B-site cations, such that the A site cation can be univalent, divalent, or trivalent, while the B site cation can correspondingly be pentavalent, tetravalent, or trivalent. Consequently, perovskites with different constituent elements can display different polar nature in different crystallographic orientations. For example, insulating perovskites $La^{3+}Al^{3+}O_3$ (LAO) and $Sr^{2+}Ti^{4+}O_3$ (STO) are both layered structures along [001], yet the former material is composed of polar $(LaO)^+$ and $(AlO_2)^-$ layers while the latter is composed of nonpolar $(SrO)^0$ and $(TiO_2)^0$ layers. As a consequence, when LAO is epitaxially grown atop a [001] STO substrate, a high-mobility two-dimensional electron gas (2DEG) forms at the $(TiO_2)^0/(LaO)^+$ interface which displays a number of exciting electronic and magnetic properties. Recent works have demonstrated that these properties can be significantly enhanced by the deliberate introduction of extrinsic defects near the LAO/STO interface. [43–45]

Fluorite-structured metal oxides have chemical composition MO_2, where M is a tetravalent

metal cation, and crystallize in a face-centered cubic structure with oxygen ions occupying each of the four internal tetrahedral sites (see Fig. 1.1c). Interestingly oxygen vacancies form very easily in the fluorite structure, a tendency which can be enhanced by doping with lower-valency oxides such as Y_2O_3, Yb_2O_3, or Gd_2O_3, leading to very high oxygen conductivity. The classical example of such a material is Y_2O_3-doped ZrO_2, often referred to as yttria-stabilized zirconia (YSZ), which contains high concentrations of point defects ranging from 3-40 mol%. [46] The high defect concentration and chemically-disordered nature of YSZ and certain other doped fluorite oxides also has the effect of consistently scattering phonons, leading to exceptionally low thermal conductivity. [47] These properties, in concert with their high chemical stability, physical toughness, and high-temperature strength, have enabled doped fluorite oxides to serve as refractory materials in thermal barrier coatings, with critical applications in the energy and aerospace sectors. [48–52] Like the perovskite and rutile oxide materials we have described, many applications of the fluorite oxides depend on the presence of defects. Therefore, in the next section we will briefly discuss defects in metal oxide materials.

1.2 Point Defects in Metal Oxide Materials

Real metal oxide materials contain point defects in their crystal lattice which can profoundly influence the overall material properties. In general these defects can be divided into two classes: intrinsic and extrinsic. Intrinsic point defects are present even in pure materials, and can be further subdivided into vacancies and interstitials, which may act as electron donors or acceptors. As an example let us consider an oxygen vacancy in perovskite oxide $SrTiO_3$ (STO). The absence of an O^{2-} anion leads to the injection of two free electrons into the lattice, and therefore the oxygen vacancy can be described as a donor defect. While the oxygen vacancy site is charge-neutral in an absolute sense, it carries a +2 charge *relative* to the typical anion sublattice site in $SrTiO_3$. Kröger-Vink notation is used to describe the relative charges of point

defects in a consistent manner. In this notation, an oxygen vacancy in STO is written $V_O^{\bullet\bullet}$, where each $\bullet$ represents a $+1$ relative charge with respect to the anion sublattice site which the defect occupies. By the same token, a strontium vacancy in STO is an electron acceptor, and is written $V_{Sr}^{//}$ where each / represents a –1 relative charge with respect to the cation sublattice site. Oxygen vacancies are the source of *n*-type conductivity in nominally-undoped STO, [53] and oxygen annealing of LAO/STO can reduce the charge carrier density by nearly four orders of magnitude. [54] However, oxygen vacancies do not act as electron donors in all metal oxides. For example, oxygen vacancies in $BaZrO_3$ can trap two free electrons and achieve neutrality relative to the anion sublattice site ($V_O^{\times}$). [55] In contrast to intrinsic defects, extrinsic defects arise from the presence of impurity ions in the crystal lattice of a given material. When impurity ions are deliberately introduced into a material, they are called dopants. In fact, doping is essential to the functionality of many metal oxide materials. For example, Sb-doped SnO_2 derives its *n*-type conductivity from the presence of Sb@Sn substitutional dopants ($Sb_{Sn}^{\bullet}$). [56, 57] As is briefly discussed in the next section, both intrinsic and extrinsic point defects can have complex interactions with grain boundaries in polycrystalline metal oxides.

1.3 Planar Defects – Grain Boundaries

Applied metal oxide materials are typically polycrystalline, and by definition contain interfaces between single-crystalline grains known as grain boundaries. As a class of intrinsic defect, grain boundaries are especially important because their presence influences the physical and electronic properties of bulk materials. For example, grain size has been shown to substantially affect hardness and wear mechanisms in α–Al_2O_3, [58] thermal conductivity in Y_2O_3-stabilized ZrO_2, [59] elecrical conductivity in CeO_2, [60] strength in pseudobrookite metal oxides, [61] and even the sensitivity of SnO_2-based gas sensors. [62] In addition, point defects can be enriched or depleted near grain boundaries with respect to their intra-grain concentrations, leading to a host

of beneficial or deleterious effects. These include embrittlement, [63–65] strengthening, [66, 67] or differential inter- and intra-grain conductivity. [68, 69] The complex effects arising from defect segregation to grain boundaries have recently stimulated extensive study in important metal oxide materials such as $SrTiO_3$. [70–73]

1.4 Summary

Engineered defects in metal oxide materials play a critical role in the functionality of material systems with ubiquitous applications in electronics, aerospace, and medicine. In this thesis we will detail our studies of complex metal oxide materials containing substitutional impurities, heterointerfaces, and/or grain boundaries, with the goal of improving material properties, using first-principles density functional theory calculations. In Chapter 2 we will present the electronic and energetic properties of pentavalent-cation-doped SnO_2, identifying a new and promising material. In Chapter 3 we will discuss the possibility of enhancing the properties of the two-dimensional electron gas (2DEG) which forms at the $LaAlO_3/SrTiO_3$ (LAO/STO) interface via *n*-type layer doping with transition metals. In Chapter 4, we will show that the LAO film polarization (P_{LAO}) can inhibit 2DEG formation in LAO/STO, and that the application of [100] uniaxial tensile strain can reduce P_{LAO} and thereby enhance 2DEG properties. In Chapter 5, we will examine the poorly-understood $\Sigma 5$ [001] twist grain boundary of $SrTiO_3$, and demonstrate that both the average positions and likely concentrations of oxygen vacancies can be controlled by the GB termination. In Chapter 6 we will explore the segregation of substitutional impurities to $\Sigma 5$ (310)/[001] tilt grain boundaries of ZrO_2 and HfO_2, and describe a fundamental difference in the characteristic segregation profiles of aliovalent and isovalent impurities; additionally, we will not only show that a YSZ grain boundary structure containing high concentrations of yttrium dopants and oxygen vacancies can be generated and structurally optimized via DFT, but also that our structure can serve as a testbed for segregation energy calculations with extrinsic impurities.

Finally, in Chapter 7, we will summarize the results of this thesis and suggest some future directions.

Chapter 2

Electronic Structures and Formation Energies of Pentavalent-Ion-Doped SnO_2: First-Principles Hybrid Functional Calculations

As discussed in Chapter 1, defects can significantly influence the bulk properties of oxide materials. Among these materials, *n*-type doped SnO_2 transparent conducting oxides (TCO) have attracted considerable attention due to the ubiquity of flat panel displays, light-emitting diodes, and solar cells. However, the reported charge carrier densities (n_e) for doped SnO_2 TCOs tend to vary widely, even for films doped with the same element. For example, Nakao *et al*. found that n_e for Ta-doped SnO_2 (TTO) films grown on bare glass is 30% lower than that for TTO films grown on an anatase TiO_2 seed layer. [2] Nakao *et al*. speculated that the TTO films grown on bare glass contain polar (110) and (101) grain boundary surfaces enriched with Sn^{2+}, which serve as traps for free carriers, while the films grown on TiO_2 favor (200) grain boundary surface orientations which contain no such traps. Shamala *et al*. reported that increasing the film deposition rate of

antimony-doped SnO_2 (ATO) from 1.5 to 2 Å/s leads to a doubling of the sheet n_e, most likely due to increased crystallinity. [74] Elsewhere in the TCO literature, seemingly-innocuous variations in experimental procedure such as film deposition rate are often unreported, confounding any comparative analyses of TCO films synthesized by different groups. These questions motivated the study which comprises this chapter, in which we present electronic and energetic properties of pentavalent-ion-doped SnO_2 via first-principles calculations. We found that phosphorus-doped SnO_2 (PTO) compares favorably with well-known TCOs ATO, FTO, and TTO, in terms of its charge carrier density and energetic favorability. In addition, we discovered the presence of impurity states in the electronic structure of iodine-doped SnO_2 which narrow the optical band gap. Finally, we found that the theoretical charge carrier densities of the doped SnO_2 systems we examined are nearly identical, indicating that the order of magnitude n_e variations reported in experimental studies may instead arise from differences in experimental conditions during material synthesis. Our calculations reveal a new potential TCO material, PTO, and emphasize the necessity for congruence in experimental conditions before comparing different TCO materials.

2.1 Introduction

Transparent conducting oxides (TCOs) are a unique class of materials that exhibit both optical transparency and electronic conductivity simultaneously. They have a wide range of applications in the devices such as flat panel displays, light-emitting diodes, and solar cells. [75] Currently, the main strategy to develop TCOs is to use wide-band-gap oxides doped with a significant amount of mobile charge carriers, either holes (p-type) or electrons (n-type). The reference TCO, indium tin oxide (Sn-doped In_2O_3, ITO), is the most commonly used due to its high optical transparency and electron mobility. [76] However, indium's rarity and an increasing demand for high-performance TCOs has motivated a number of efforts to develop new transparent conducting materials. [77, 78] In recent years, pentavalent-ion (Ta^{5+} and Nb^{5+}) doped TiO_2 and

SnO_2 have shown some promise in this regard, though some unexpected experimental phenomena arise. For example, a series of experiments showed that pentavalent-ion-doped anatase TiO_2 is highly conductive, but identically doped rutile TiO_2 remains insulating. [79–83] Later first-principles computational studies further confirmed this phenomenon, and attributed the different conductive behavior to differences in the symmetry of the local TiO_6 structure. [84, 85] SnO_2 shares the same crystal structure type with the rutile-phase TiO_2. [86, 87] One Sn atom and six adjacent O atoms form a distorted SnO_6 octahedra, which has the exact same local structure character with that of the TiO_6 unit in the rutile-phase TiO_2. Moreover, the Sn cation shares the same valence state (+4) with the Ti cation in TiO_2. Absent knowledge to the contrary, one might speculate whether pentavalent-ion doping of SnO_2 would yield insulating properties, as in the case of rutile TiO_2.

On the one hand, a number of experiments have been carried out to explore the possibility of achieving competitive TCO properties by doping SnO_2. [1–11] For example, transparent conductive Ta-doped SnO_2 has been prepared using film growth techniques such as Chemical Vapor Deposition (CVD) [88] and Pulsed Laser Deposition (PLD). [2–4] High charge carrier densities on the order of 10^{20}–10^{21} [cm^{-3}] were measured with Ta doping levels of 3-10 mol%, along with suitable optical transparency. [2–4, 88] Nb-doped SnO_2 (NTO) has been investigated in a similar fashion in recent years. [89,90] Nakao *et al.* prepared NTO thin films using the PLD, and found that unstrained films grown on glass exhibited relatively low charge carrier density because of the formation of deep impurity levels below the conduction band minimum (CBM). [89] They also observed that in-plane tensile strain could significantly enhance the charge carrier density of NTO films. In another recent experiment, Turgut *et al.* found that the resistivity of NTO films varied with Nb doping concentration. [90] They explained these variations by suggesting that Nb dopants could exist in several different valence states (Nb^{3+}, Nb^{4+}, and Nb^{5+}) in the SnO_2, and that doping concentration influences the probability of each state. The authors proposed that at low doping concentrations, Nb^{5+} ions dominate at Sn sites and donate free electrons into

the system, producing the marked decrease in sheet resistance; at high doping concentrations (>3 mol%), some of the Nb^{5+} ions are reduced to Nb^{3+}, reducing the charge carrier density and increasing sheet resistance. Despite this plausible explanation, a solid determination of Nb valence states is still required to deeply understand the conducting mechanism of NTO. Besides Ta- and Nb-doped SnO_2, Sb-doped SnO_2 has also been frequently synthesized to explore its transparent conducting properties, with encouraging results. [8–10] By contrast, P-doped SnO_2 has been a subject of very few experimental investigations, none of them recent.

On the other hand, corresponding first-principles computational studies have been done to explore the effects of pentavalent dopants on the electronic properties of SnO_2. [91, 92] Cheng *et al*. screened a variety of dopants (including F, I, P, Sb, Nb, and Ta) using standard density functional theory (DFT) calculations, investigating their potential to produce desirable TCO behavior in SnO_2. [92] They found that the band gaps of P-, Sb-, F-, and I-doped SnO_2 decreased relative to that of bulk SnO_2, while those of Nb- and Ta-doped SnO_2 increased. This contradicts Turgut *et al*.'s experimental findings that the effective optical gap of SnO_2 was progressively reduced from 3.98 to 3.73 eV when doped with increasing concentrations of Nb (1-4 mol%). [90] By using first-principles hybrid functional calculations, Varley *et al*. assessed the possibility of obtaining *p*-type SnO_2 by doping with N, P, As, and Sb, but found that P, As, and Sb could serve as *n*-type dopants instead. [93] We noted that standard DFT calculations within either the local density approximation (LDA) or generalized gradient approximation (GGA) severely underestimate the band gap of oxides such as SnO_2, and cannot accurately describe strongly correlated *d* electrons. [94, 95] Despite the fact that 4*d* and 5*d* electrons have much weaker electron correlation strength compared to 3*d* electrons, [96] the electron correlation character of Nb 4*d* and Ta 5*d* electrons still plays a crucial role not only in tuning the electronic properties of doped SnO_2 but also in determining the valence state of the Nb and Ta dopants. Therefore, to elucidate the electronic structure of pentavalent-ion doped SnO_2 and the valence state of Nb dopant in SnO_2, systematic computational studies using advanced DFT calculations such as the

hybrid functional approach are essential.

In this work, by using first-principles hybrid DFT calculations, we studied the doping effects of pentavalent ions (Ta, Nb, P, Sb, and I) on the electronic properties of SnO_2, and explore their potential to yield transparent conductivity. To account for the band-gap underestimation in standard DFT calculations, we began by calibrating the hybrid functional method to match the experimental band gap of SnO_2, and then examined the electronic structure of each doped SnO_2 system. The theoretical charge carrier density for each system and a systematic comparison between these values and experimental data were represented. Finally, we estimated the defect formation energies of the each doped SnO_2 system.

2.2 Methods

In this work, the doped SnO_2 systems were modeled using 72-atom $2 \times 2 \times 3$ supercells, with a single Sn replaced by a pentavalent ion (Ta, Nb, P, Sb, or I). This amounts to a doping concentration of 4.17 mol%. Only the neutral charge state of the dopants was considered. Undoped SnO_2 was modeled using a 6-atom primitive cell. The projector augmented wave (PAW) [97] pseudopotentials were used to treat electron-ion interactions and the GGA parametrized by Perdew-Burke-Ernzerhof (PBE) [98] was used to describe the electron exchange and correlation interactions. A 440 eV cut-off energy for the plane wave basis set was used. $2 \times 2 \times 2$ and $6 \times 6 \times 10$ Γ-centered k-point meshes were used for supercell and primitive cell electronic structure calculations, respectively. The convergence threshold for self-consistent-field iteration was set at 10^{-4} eV. The density of states (DOS) for each optimized doped SnO_2 structure was calculated using the tetrahedron method with Blöchl corrections. [99] All the structure models are first optimized using the standard DFT calculations within the GGA-PBE framework based on the well-known fact that standard DFT calculations can predict experimental structures for many compounds, including SnO_2, quite well. [100, 101] Lattice parameters and atomic positions

were relaxed until all components of the residual forces were smaller than 0.01 eV/Å. In the subsequent single-point total energy calculations, the Heyd-Scuseria-Ernzerhof (HSE06) [102] hybrid functional was used to produce the exact band gaps of SnO_2. As discussed later, the exact Hartree-Fock (HF) exchange contribution to the hybrid functional was tuned to 33% to match experimental values. All the spin-polarized calculations were carried out using the Vienna *Ab-initio* Simulation Package (VASP). [103, 104]

2.3 Results and Discussion

2.3.1 Selection of HSE06 Mixing Parameter

Standard DFT calculations typically underestimate band gaps, primarily because the LDA or GGA functionals cannot properly describe the electron-electron correlation-exchange interaction. [105] The underestimation is particularly severe in SnO_2, due to an abnormally large underestimation of the binding energy of Sn *d* states. [94] The hybrid functional approach has been shown to be significantly better than standard DFT calculations at producing accurate band gaps. [106, 107] Previous hybrid functional calculations using a standard 25% mixing parameter have yielded a band gap of approximately 2.96 eV [108] for SnO_2, as compared to the GGA-PBE value of 0.7 eV [101] and the experimental value of 3.6 eV. [109] Varley *et al.* have produced a band gap of 3.50 eV using a 32% HF mixing parameter, though they provided no explanation of how they derived that mixing parameter. [93] To elucidate the dependence of the band gap on the HF mixing parameter, we performed four hybrid functional calculations on the SnO_2 primitive cell using a 0% (standard DFT), 13%, 25%, and 45% contribution of the exact HF exchange. It is noted that the optimized lattice structure of the primitive SnO_2 cell from the standard DFT calculation within the GGA-PBE framework is used in each set of the static hybrid functional calculation. This can produce a rigorous relationship between the band gap and HF mixing parameters. The dependence of the band gap on the HF mixing parameter is displayed in Fig. 1.

The resulting band gap shows a nearly linear dependence on the percent contribution of the exact HF exchange. Based on this trend, by referencing the experimental band gap of SnO_2 (3.6 eV), the ideal exact hybrid functional contribution was found to be 33%, which is in a good agreement with the prior HF mixing parameter. [93] It is noted that the optimized mixing parameter based on the band gap tuning works well for the undoped bulk structure, but it is not necessarily ideal for the doped systems, particularly for the non-band-gap-related material properties. A detailed elucidation of the influence of the HF mixing parameter on the non-band-gap-related material properties might be worthy of further studies. In this work, however, the hybrid functional calculations with the optimized HF mixing parameter are expected to produce reliable results on the relative band-gap variation and impurity states caused by doping.

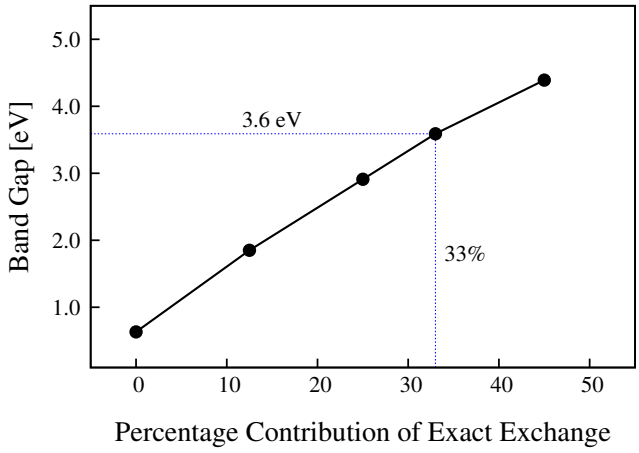

Figure 2.1: Dependence of calculated SnO_2 band gap on the percent contribution of exact Hartree-Fock (HF) exchange. The dashed blue line indicates HF percentage at which the experimental band gap is reproduced.

In addition, it is noted that a new HSE+U method was recently proposed to overcome the underestimation of the band gap. [110] In this approach, instead of adjusting the percentage contribution of the exact exchange, the fraction of exact exchange energy is fixed at 0.25 and the hybrid functional is combined with an optimal U value. The advantage of this approach is that strongly localized and delocalized states are treated differently, which leads to a more accurate description of the electronic structure than that solely using either the HSE or GGA+U approach.

2.3.2 Electronic Structure

Bulk SnO_2

Bulk SnO_2 crystallizes in a tetragonal structure (space group no. 136, $P4_2/mnm$) with experimental lattice constants a = 4.74 Å and c = 3.19 Å. [109, 111] We began by estimating the equilibrium lattice constants of bulk SnO_2 using standard DFT calculations within the GGA-PBE framework, based on the well known fact that the standard DFT calculations can well predict geometrical structures of many compounds. [100, 101] Our calculated lattice parameters within this scheme are a = 4.81 Å and c = 3.25 Å, which are slightly overestimated compared with the experimental lattice parameters. [101]

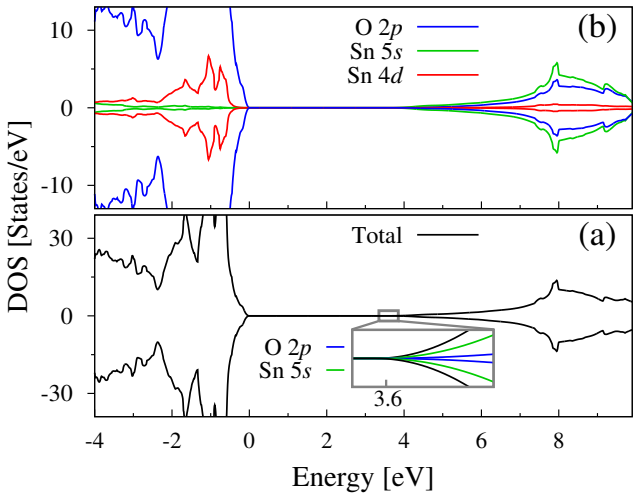

Figure 2.2: Calculated TDOS (a) and PDOS (b) plots for SnO_2 using the HSE06 functional with a 33% HF mixing parameter.

Next we calculated the electronic structure of bulk SnO_2 within the hybrid functional framework. Using a 33% mixing parameter, the hybrid functional calculations produce a band gap of 3.6 eV. The resultant total density of states (TDOS) and partial density of states (PDOS) are depicted in Fig. 2. The PDOS demonstrates that the valence band is mainly composed of O 2*p* orbitals, and that the conduction band is composed of strongly hybridized Sn 5*s* and O 2*p* orbitals. The extremely shallow curve of states near the CBM (see Fig. 2a – Inset) indicates deep

wells in the band structure, as first reported by Arlinghaus. [112] This implies that *n*-type SnO_2 possesses a relatively small electron effective mass and thus high electron mobility, making it an excellent TCO material. The electronic structure characteristics derived from this work are consistent with previous computational studies using either standard DFT or hybrid functional calculations. [101, 113–116]

Ta- and Nb-Doped SnO_2

We next studied the electronic properties of Ta- and Nb-doped SnO_2. The calculated TDOS of Ta-doped SnO_2 is depicted in Fig. 3a. It shows that no impurity states appear within the band gap and that the Fermi level lies just above the CBM, revealing typical *n*-type conducting character. The PDOS (Fig. 3b) demonstrates that the majority of Ta 5*d* states are located in the conduction band. This implies that each Ta dopant atom has an electron configuration resembling that of a $Ta^{5+}(5d^0)$ cation in SnO_2, injecting one free electron into the system per dopant and producing the *n*-type conductivity. These additional electrons occupy the lowest conduction band states below the Fermi level, and hence Pauli blocking prevents electron transitions into these occupied states. For this reason the electron excitation with the accompanying optical absorption can take place only from the valence band states to higher conduction band states above the Fermi level. This effect is also known as the Burstein-Moss shift, [117, 118] which leads to a widening of the effective optical band gap. Ta-doped SnO_2 displays an effective optical band gap of 4.5 eV that is substantially larger than that of the undoped SnO_2 (3.6 eV). This and all subsequent optical gaps were calculated by measuring the position of the Fermi level with respect to the VBM. The widened optical band gap implies that a significant blueshift ($\approx$0.9 eV) of the optical absorption edge would occur in this system. It is noted that such a determination of the Burstein-Moss shift by comparing the optical band gaps between the undoped and doped SnO_2 may be incomplete because the experimental optical absorption shift also depends on other factors not visible from the DOS. Nevertheless, the calculation-derived blueshift in Ta-doped

SnO_2 of 0.9 eV compares favorably with experimental blueshifts in Sb-doped SnO_2 of roughly 0.6 eV [10, 119]. As discussed later, the Ta-doped and Sb-doped SnO_2 systems show similar electronic structure characters. The widened optical gap also guarantees that the system remains transparent to visible light. In short, due to its excellent *n*-type conductivity and visible-light transparency, Ta-doped SnO_2 is a promising candidate TCO material. [3, 4, 88]

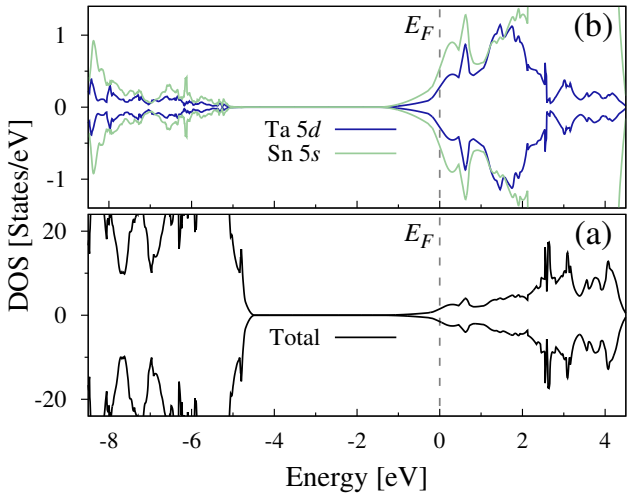

Figure 2.3: Calculated TDOS (a) and PDOS (b) plots for Ta-doped SnO_2. The grey dashed line indicates the Fermi level in this and each subsequent DOS plot.

By taking Ta-doped SnO_2 as an example, we also examined the influence of the doping concentration on the electronic properties of doped SnO_2. We doubled the Ta doping concentration by replacing two Sn atoms with two Ta atoms in the SnO_2 supercell model, and calculated the electronic structure (not shown here). We found that increasing the doping concentration had no obvious effect on the energy gap between the VBM and CBM, and very little effect on the general shape of the DOS. However, the charge carrier density was increased due to the additional free electron injected by the second Ta dopant atom. The free electron further increased the occupation of Sn 5*s* orbitals in the conduction band, pushing the Fermi level deeper into the conduction band relative to the less strongly doped system, thus increasing the effective optical band gap.

The calculated spin-polarized TDOS and PDOS of Nb-doped SnO_2 are shown in Fig. 4a, and an enlarged view near the Fermi level is shown in Fig. 4b. Unlike Ta-doped SnO_2, Nb-doped

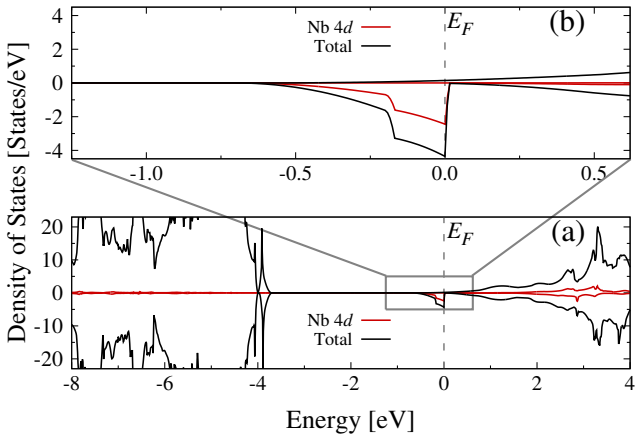

Figure 2.4: Calculated DOS plot for Nb-doped SnO_2 (a) and enlarged near the Fermi level (b).

SnO_2 has some moderately localized down-spin-polarized impurity gap states just below the Fermi level, spanning an energy range of roughly 0.5 eV. These gap states are mainly composed of Nb 4*d* orbitals (see Fig. 4b), and the Nb dopant itself carries a magnetic moment of 0.56 μ_B. This is remarkably different from Ta-doped SnO_2, in which Ta 5*d* orbitals are delocalized throughout the conduction band and no localized gap states are found. Nb dopant atoms in SnO_2 are typically assumed to exist as Nb^{5+} ions at Sn sites, leading to an expected injection of one free electron per dopant and ultimately similar *n*-type conductivity. In this work, the existence of the occupied Nb 4*d* gap states imply that the Nb dopant exists in an oxidation state close to $Nb^{4+}(4d^1 5s^0)$. Interestingly, Morante *et al.* found [120] that Nb exists in both its +4 and +5 oxidation states when doped into TiO_2, while Turgut *et al.* [90] suggested that Nb could exist in +3, +4, or +5 valence states when doped into SnO_2, depending on the doping concentration. Moreover, the Nb gap states also indicate that the Nb 4*d* orbital is more localized than the Ta 5*d* orbital, as 4*d* orbitals typically are. [121, 122] The Nb 4*d* gap states below the conduction band bottom are detrimental to the system's electron transport properties because they reduce not only the charge carrier density but also electron mobility due to the increase in electron effective mass. In fact, Nakao *et al.* found that Nb-doped SnO_2 displayed far lower charge carrier density than Ta-doped SnO_2 because of the formation of a deep localized Nb impurity states, [89] which is

consistent with our hybrid functional calculations. Taken together, our theoretical calculations and these experimental findings indicate that Nb is not likely to be an ideal dopant for developing *n*-type SnO_2-based TCO materials.

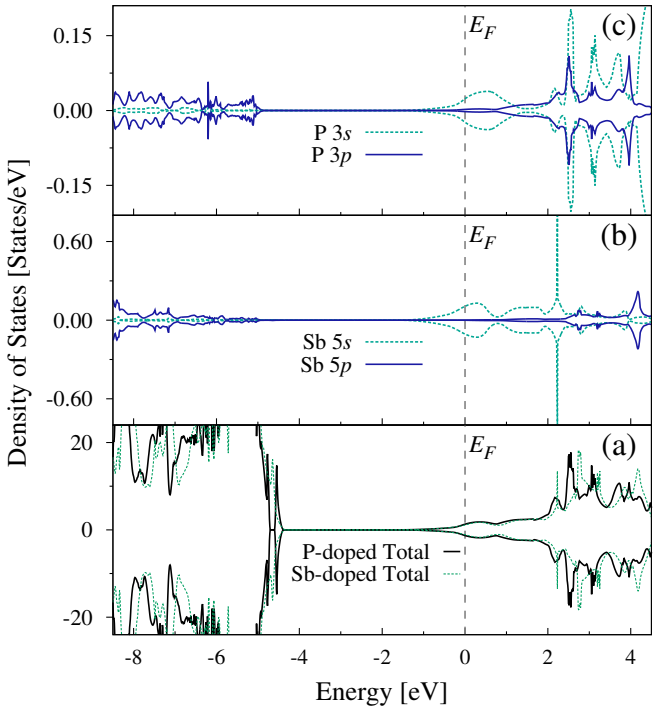

Figure 2.5: Calculated TDOS (a) and PDOS plots for Sb- (b) and P- (c) doped SnO_2.

P- and Sb-Doped SnO_2

Here we studied the electronic structure of SnO_2 doped with group VA elements P, As, and Sb. Despite prior intense investigations on Sb-doped SnO_2, [8–11, 123] we calculated its electronic structure as a point of comparison with that of the P-doped SnO_2. As's toxicity precludes its usage in widespread TCO materials. Its electronic structure was, however, included in the supporting information section. The calculated TDOS and PDOS of P- and Sb-doped SnO_2 are depicted in Fig. 5. The TDOS in Fig. 5a clearly shows typical *n*-type conductivity, an absence of impurity gap states, and a wide optical band gap of roughly 4.5 eV for both doped systems. The calculated PDOS for P-doped SnO_2 (Fig. 5c) demonstrates that the majority of

P 3*s* and 3*p* orbitals are in the conduction band, indicating that the P dopant atoms exist as $P^{5+}(3s^0 3p^0)$ cations which introduce one free electron each. As in the case of Ta-doped SnO_2, the free electrons introduced by the P^{5+} ions lead to the *n*-type conductivity. Sb yields an extremely similar electronic structure as a dopant (see Fig. 5b), provoking identical conclusions about its valence state in SnO_2. Given that Ta- and Sb-doped SnO_2 have been shown as promising TCOs in the experiments, P-doped SnO_2 seems an excellent choice for further experimental investigation.

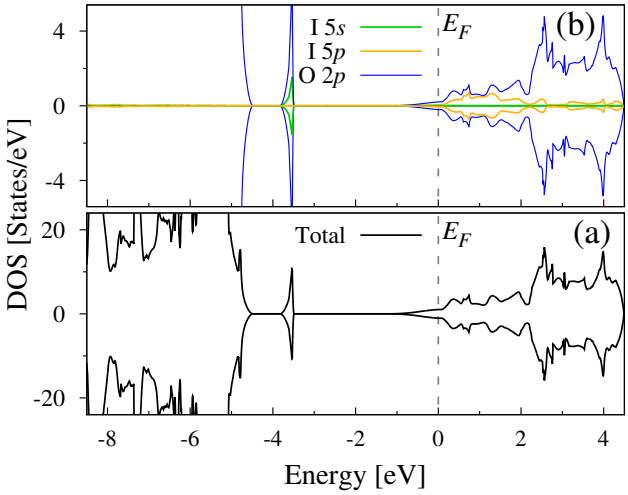

Figure 2.6: Calculated TDOS (a) and PDOS (b) plots for I-doped SnO_2.

I-doped SnO_2

Next we considered the case of I-doped SnO_2. The calculated TDOS and PDOS plots are presented in Figs. 6a and 6b, respectively. As expected, I-doped SnO_2 also shows *n*-type conducting character, with the Fermi level lying within the conduction band just above the CBM. However, a group of isolated states appears within the band gap just above the VBM. The PDOS shown in Fig. 6b demonstrates that these new gap states come mainly from O 2*p* orbitals, with a smaller–but still significant–contribution from I 5*s* orbitals. The strong orbital hybridization between O 2*p* and I 5*s* orbitals implies that each I dopant forms strong I-O bonds in SnO_2. I 5*p* states are mainly located above the Fermi level, having no contribution to the gap states. This

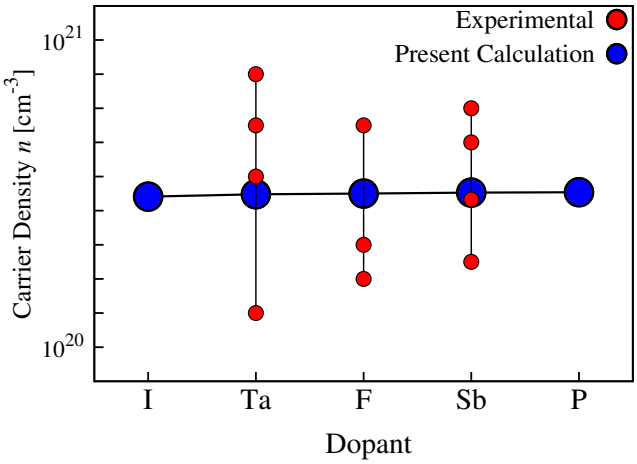

Figure 2.7: Calculated (blue) and experimentally derived (red) charge carrier densities n for doped SnO_2. The doping levels are 4.17 mol% for the theoretical calculation and about 4-5 mol% for experiments. [1–11].

suggests that the I dopant has an electron configuration of $5s^2 5p^0$ and exists as an I^{5+} cation at Sn sites, as in the case of I-doped TiO_2. [84] The effective optical gap from the new gap states to the Fermi level is roughly 3.5 eV, corresponding to a photon energy in the UV spectrum ($\approx$357 nm). Thus I-doped SnO_2, despite having a narrower effective gap than the other systems, is still transparent to visible light [124] and still has potential as a TCO material.

2.3.3 Charge Carrier Density

In this section, we calculated the charge carrier density for each system (barring As- and Nb-doped SnO_2) by integrating their DOS from the CBM to the Fermi level. Carrier density for F-doped SnO_2 (FTO) was also calculated and included as a baseline comparison, given FTO's long history as a robust TCO in industry. [125] It should be noted that in FTO, F replaces O instead of Sn because of its high electronegativity. Each F atom accepts one fewer electron than each O, and thus substitutional F doping at the O site yields one free electron per dopant atom, just as in pentavalent cation doping at the Sn site. In addition, we collected some available experimental charge carrier density values for these doped systems for a more direct comparison. [1–11] All the calculated and experimental values of the charge carrier density are plotted in Fig. 7.

It is immediately evident that all of these calculated values are remarkably similar, especially relative to the large experimental variations. The source of those variations, however, bears close attention. It has been decisively proven that film deposition rate, substrate temperature, film thickness, oxygen partial pressure, and other frequently unreported experimental conditions can cause multi-fold changes in the carrier density of TCO films. [74, 126–128] Additionally, while we have selected data from systems with a narrow range of doping concentrations, slight differences still remain. In our simulation, the doping concentration for each doped system is identical (4.17 mol%), and each doped SnO_2 system has one free electron per dopant atom. The calculated results indicate that Ta-, I-, P-, and Sb-doped SnO_2 all possess charge carrier densities comparable to that of FTO. Furthermore, our calculated values for Ta-, F-, and Sb-doped SnO_2 at 4.17 mol% doping compare favorably with the aggregate data at similar doping levels in the literature, lending further support to the validity of our calculations.

2.3.4 Defect Formation Energy

To evaluate the relative stability of these pentavalent-ion-doped SnO_2 systems, we calculated the formation energy for each doped system within the hybrid functional calculations framework. In this work, only the neutral state of each dopant was considered. Since all the considered dopants typically occupy Sn-sites in SnO_2, we used the following formula to calculate the formation energy:

$$E_f^X = E_{doped}^X - E_{undoped} - \mu_X + \mu_{Sn} \tag{2.1}$$

E_{doped}^X is the total energy of the $2 \times 2 \times 3$ supercell of X-doped SnO_2 (X=Ta, Nb, Sb, P, and I), while $E_{undoped}$ is the total energy of the $2 \times 2 \times 3$ supercell of undoped SnO_2. μ_X is the chemical potential of dopant X, calculated from the energy per atom of the most stable low-pressure and low-temperature elemental phase for each dopant, *i.e.,* E_X. The defect formation energy is not fixed, but depends on the chemical potential of Sn, μ_{Sn}. In fact, defect formation is

often controlled by tuning the chemical potential of O in the materials preparation process. This is because the chemical potentials of Sn and O are linked by the stability of the SnO_2 phase:

$$\mu_{Sn} + \mu_{O_2} = E_{SnO_2} \tag{2.2}$$

μ_{Sn} and μ_O represent the chemical potentials of Sn and O, respectively, and E_{SnO_2} refers to the total energy of an SnO_2 formula unit, *i.e.*, the chemical potential of SnO_2. To avoid confusion regarding the chemical potential references, we have included the following two equations:

$$\Delta\mu_{Sn} = \mu_{Sn} - E_{Sn} \tag{2.3}$$

$$\Delta\mu_O = \mu_O - \frac{1}{2}E_{O_2} \tag{2.4}$$

E_{Sn} is the total energy per atom of bulk Sn, and E_{O_2} is the total energy of the ground state O_2 molecule. The formation enthalpy of SnO_2 is defined as:

$$\Delta H_f(SnO_2) = E_{SnO_2} - E_{Sn} - E_{O_2} \tag{2.5}$$

Using these definitions, Equation (5) becomes:

$$\Delta\mu_{Sn} + 2\Delta\mu_O = \Delta H_f(SnO_2) \tag{2.6}$$

The extreme O-rich limit is characterized by μ_O=$\frac{1}{2}E_{O_2}$, *i.e.*, $\Delta\mu_O = 0$ and $\Delta\mu_{Sn} = \Delta H_f(SnO_2)$. The O-poor (Sn-rich) limit is defined as μ_{Sn}=E_{Sn}, *i.e.*, $\Delta\mu_{Sn} = 0$ and $\Delta\mu_O = \frac{1}{2}\Delta H_f(SnO_2)$. Our HSE calculated formation enthalpy is -5.4 eV, which is in a good agreement with the experimental value of -6.0 eV. [129] Hence, the theoretical value of $\Delta\mu_O$ is in the range of -2.7 eV $\leq \Delta\mu_O \leq 0$ eV.

The calculated defect formation energies of the X-doped SnO_2 systems (X=Ta, Nb, Sb, P,

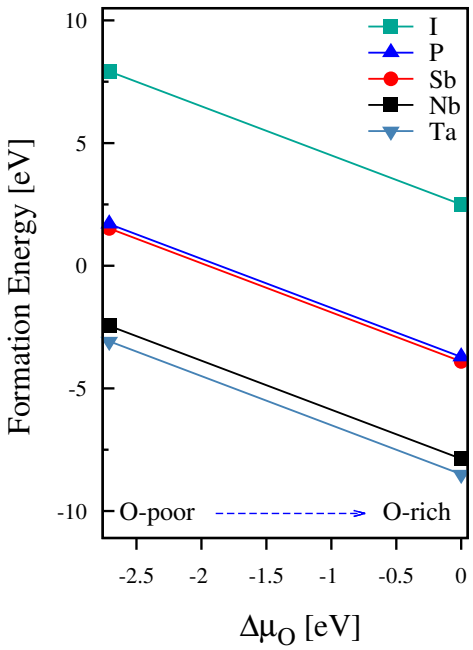

Figure 2.8: Calculated formation energies of the pentavalent cation-doped SnO_2 with respect to $\Delta\mu_O$.

and I) are plotted with respect to $\Delta\mu_O$ in Fig. 8. The following trends can be derived:

(1) The substitution of dopant X for an Sn atom in SnO_2 (referred to as "X@Sn" doping) is energetically more favorable under O-rich conditions than under O-poor. In other words, as $\Delta\mu_O$ increases, the defect formation energy tends to decrease.

(2) For X-doped SnO_2, in the whole range of $\Delta\mu_O$, defect formation energies can be ordered from least to greatest as follows: Ta<Nb<Sb<P<I. For both group VA and VB dopants, formation energy increases with electronegativity: Nb is a less favorable dopant than Ta, while P is a less favorable dopant than Sb. The overall trend of formation energies is consistent with prior computational results within the standard DFT framework reported by Cheng *et al*. [92] In fact, Varley *et al*. previously reported formation energies of Sb- and P-doped SnO_2 considering multiple dopant charge states using the hybrid functional, and their results also fit the present trend. [93] According to Varley *et al*.'s results, the defect formation energy of substitutional Sb doping at the Sn site is much lower than that of P doping under both O-poor and O-rich conditions. Despite the difference in the absolute values of defect formation energy between our

work and that of Varley *et al*. caused by the different models, the trend of formation energies is still the same: substitutional Sb doping at the Sn site is more thermodynamically favorable than substitutional P doping under both O-poor and O-rich conditions.

(3) I@Sn doped SnO_2 has the highest formation energy, implying that I@Sn doping is the least energetically favorable among the dopant substitutions considered. In principle, an I^- ion can substitute an O^{2-} (referred to as "I@O") in SnO_2, and release a free electron into the system, leading to *n*-type conductivity, just as in the case of F@O doped SnO_2. As a result, one may be interested in the energetic favorability of substitutional I@O doped SnO_2. Our prior computational study on the closely related oxide TiO_2 suggested that under O-rich conditions, I@Ti substitutions are more energetically favorable than I@O, while under O-poor conditions I@O substitutions are more favorable than I@Ti. [130] Moreover, the I@Ti doped TiO_2 system has the lowest formation energy in the O-rich limit. A similar case is expected to occur in I-doped SnO_2, and thus in this work, only I@Sn doping was considered. In fact, Cheng *et al*. used standard DFT calculations to determine the formation energy of I@O doped SnO_2 under O-rich conditions, and produced a formation energy of 9.28 eV, which is much larger than our calculated value for I@Sn doped SnO_2 (2.50 eV) under O-rich conditions.

In addition, it is worth mentioning that we have adopted the chemical potential μ_X from the total energy per atom of the most stable bulk elemental phase of each dopant, which is consistent with the approach of prior theoretical studies. [92] This aims to produce a qualitative comparison of the defect formation energy for each system with respect to $\Delta\mu_O$ in a direct way, and in fact yields a useful trend describing the relative thermodynamic stabilities of the doped systems. This is, however, a simplified description of the experimental reality. In practice, the competitive formation of secondary oxides such as P_2O_5 can significantly hinder experimental synthesis of doped SnO_2. [93] To avoid the formation of these secondary phases and maintain the stability of SnO_2, $\Delta\mu_X$ ($\Delta\mu_X = \mu_X - E_X$) and $\Delta\mu_O$ must satisfy the following condition: $2\Delta\mu_X + 5\Delta\mu_O < \Delta H_f(X_2O_5)$.

2.4 Conclusions

The electronic properties and relative thermodynamic stability of pentavalent-ion (Ta, Nb, Sb, P, and I) doped SnO_2 were examined using first-principles hybrid density functional theory calculations. These pentavalent-ion-doped SnO_2 systems are energetically more favorable under O-rich conditions than under O-poor. Additionally, the dopants can be arranged in descending order of thermodynamic favorability in SnO_2 as follows: Ta, Nb, Sb, P, I. Ta- and Sb-doped SnO_2 show typical *n*-type conductivity with wide effective optical gaps (>4 eV) and high charge carrier densities. I-doped SnO_2 has isolated occupied gap states below the Fermi level consisting of O 2*p* and I 5*s* orbitals, which narrow the optical band gap to 3.5 eV. Nb-doped SnO_2 exhibits relatively localized Nb 4*d* states below the conduction band bottom, implying that the Nb dopant exists as an Nb^{4+}-like cation, which is in good agreement with recent experimental findings. P-doped SnO_2 shows similar *n*-type electronic structure character with that of Ta- and Sb-doped SnO_2, and thus P-doped SnO_2 could be a promising candidate TCO for further experimental investigation.

2.5 Acknowledgements

Chapter 2, in full, is a reprint of the material "Electronic Structures and Formation Energies of Pentavalent-Ion-Doped SnO_2: First-Principles Hybrid Functional Calculations" as it appears in The Journal of Applied Physics. Maziar Behtash, Paul H Joo, Kesong Yang, 117, 175101, (2015). The dissertation author was the primary investigator and author of this paper.

Chapter 3

Nb and Ta Layer Doping Effects on the Interfacial Energetics and Electronic Properties of $LaAlO_3/SrTiO_3$ Heterostructure: First-Principles Analysis

In Chapter 2 we have examined the bulk material properties of *n*-type doped transparent conducting oxide (TCO) materials, and identified phosphorus-doped SnO_2 as a new potential TCO. However, we have noted that the experimental charge carrier density of these materials is acutely sensitive to interfacial factors. We now turn to the study of perovskite oxide heterointerfaces, specifically the $LaAlO_3/SrTiO_3$ (LAO/STO) heterostructure (HS). While both LAO and STO are insulating oxides, a two-dimensional electron gas (2DEG) is formed at the $(LaO)^{+1}/(TiO_2)^0$ interface with many exciting properties, including the coexistence of magnetism and superconductivity. [131–133] Prior experimental studies have indicated that the electronic properties of the LAO/STO 2DEG can be enhanced, for example by $ATiO_3$ (A = Ca, Sr, Sn, or Ba) layer insertion at the interface, [134] or *n*-type doping of STO near the interface by transition

or rare earth metals. [43, 44, 135–137] In this Chapter we explore the possibility of enhancing the electronic and magnetic properties of the LAO/STO 2DEG through *n*-type layer doping with transition metal cations at both sides of the interface, via first-principles calculations. We found that Nb (Ta) doping is most energetically favorable at the interfacial Ti site, and that the interfacial charge carrier density in these doped systems is significantly enhanced with respect to the undoped LAO/STO HS. In addition, we found that Nb (Ta) doping at the interfacial Al site can enhance the charge confinement of the interfacial 2DEG to only two TiO_2 atomic layers of the STO substrate. Finally, we found that the interfacial magnetism can also be increased via Nb (Ta) layer doping in the LAO/STO system.

3.1 Introduction

In recent years, perovskite oxide heterostructures (HS) have been paid much attention due to the emergence of unexpected physical properties at their interfaces, which were absent in their individual parent compounds. For example, a considerable high charge carrier density ($\sim 10^{13}$ cm^{-2}) and highly-mobile ($\sim 10^{4}$ cm^{2} V^{-1} s^{-1}) two-dimensional electron gas (2DEG) is observed at the *n*-type $(LaO)^{+1}/(TiO_2)^{0}$ interface between two insulating non-magnetic perovskite oxides, polar $LaAlO_3$ (LAO) and non-polar $SrTiO_3$ (STO). [138] The LAO/STO HS system also exhibits other material properties such as interfacial ferromagnetism and superconductivity, [131–133, 139, 140], colossal magnetoresistance [141, 142] and electric-field controlled insulator-to-metal transition. [143, 144] One of the widely accepted mechanisms behind the formation of metallic interfacial states in the STO-based HS systems is the *"polar catastrophe"* theory, in which charge transfers from the polar $(LaO)^{+1}$ layer of LAO to the non-polar $(TiO_2)^{0}$ layers of the STO substrate. [145] In addition, surface/interface defects such as oxygen vacancies [146–149] and cation-intermixing [150, 151] were also proposed to be able to produce 2DEG.

Despite the variety of mechanisms implicated in 2DEG formation, recent concerted re-

search efforts have been made to further tailor the electronic properties of 2DEG in the LAO/STO HS. [152–155] For example, applying an external electric field was found to be capable of tuning both carrier concentration and the required critical thickness of LAO to form a 2DEG at the interface. [144, 156–159] Along with this, strain also shows prominent effects on the interfacial charge carrier density, electron confinement effects, and the LAO critical thickness for forming the 2DEG. [152, 153, 155, 160, 161] Another effective way to tune the electron transport properties of 2DEG in the LAO/STO HS is through transition-metal and rare-earth metal doping, which can significantly improve the electron transport properties. [43, 44, 135–137] For example, it has been experimentally and theoretically observed by Choi *et al.* [43] that fractional δ-doping of La at Sr site in STO/STO ($La_xSr_{1-x}TiO_3$/STO) HS system near the interfacial region could produce a high-mobility 2DEG. This is because one La^{3+} ion at a Sr^{2+} site releases one an extra electron into the system, and the additional electron occupies the Ti 3*d* orbitals, leading to the formation of 2DEG. Blamire *et al.* [134] also found that inserting one unit cell of $ATiO_3$ (A = Ca, Sr, Sn, and Ba) at the interface between LAO and STO could significantly modulate the sheet carrier density of 2DEG. Their experimental measurements show that the Sn doping at La sites in the LAO/STO HS has the maximum carrier density. This conclusion is consistent with recent first-principles electronic structure calculations that reveals the Sn doping near the interfacial region can significantly enhance the charge carrier density of 2DEG in LAO/STO HS system. [162] The main reason is that the Sn^{4+} doping at Al^{3+} sites introduces one additional electron into the HS system, which leads to the higher charge carrier density and even large magnetic moments on Ti ions. Hwang *et al.* [154] also found that inserting $LaTiO_3$(LTO) layers between LAO and STO can improve the charge carrier density in the LAO/STO HS, which is in agreement with first-principles calculations. [163] Very recently, Chen *et al.* found that a layer doping using $La_{1-x}Sr_xMnO_3$ (x=0, 1/8, and 1/3) at the interface (corresponds to the Mn doping at Al sites) between the disordered $LaAlO_3$ and crystalline $SrTiO_3$ could enhance the electron mobility by more than two orders of magnitude. [164] This experimental finding is very surprising,

because the electron doping often plays a bigger role in improving the electron carrier density than in improving the electron mobility. Nevertheless, one possible underlying reason for the high electron mobility is that the Mn doping introduces Mn 3*d*-orbital related conducting states, which has a lower effective mass that Ti 3*d* orbitals related ones. [165] In spite of this intriguing experimental finding, one may speculate that the layer doping using 4*d* or 5*d*-based elements would be more effective in enhancing the electron transport property of the 2DEG in LAO/STO system since these less localized nature of 4*d*- and 5*d* orbitals will result in a smaller electron effective mass and thus potentially lead to a higher mobility. Consequently, it turns out that Nb and Ta doping at either Ti sites [166] in the STO substrate or Al sites in the LAO film would be a promising way to enhance the electron transport property of the LAO/STO HS system based on the two following considerations: i) Nb^{5+} (Ta^{5+}) doping at either Ti^{4+} sites or Al^{3+} doping would increase the interfacial charge carrier density; ii) Nb 4*d*- and Ta 5*d*-related conducting states may have high electron mobility. Hence, from the above viewpoints, it is necessary to study the Nb (Ta) doping influences on the materials properties of the LAO/STO HS system.

In this paper, thermodynamic stability, electronic, and magnetic properties of *n*-type $(LaO)^{+1}/(TiO_2)^0$ interfaces in LAO/STO HS systems were studied with respect to Nb(Ta)-doping at the Ti (Nb@Ti)/(Ta@Ti) and Al (Nb@Al)/(Ta@Al) sites near the interfacial region using first-principles electronic structure calculations. Our results indicate that Ta-doping at the Ti site (Ta@Ti) is more energetically favourable compared to the undoped and other doped LAO/STO HS systems. We predict that partial occupation of DOS effectively increases near the Fermi energy for Nb(Ta)@Ti doped LAO/STO HS systems, resulting in higher electron carrier density at the TiO_2 terminated $(LaO)^{+1}/(TiO_2)^0$ *n*-type interfaces. Furthermore, our calculations demonstrate that the mobile charges of 2DEG is confined within two TiO_2 atomic layers of the STO substrate for Nb@Al and Ta@Al doped LAO/STO HS systems, which improves the quantum confinement effects. Finally, the changes in calculated magnetic moments in undoped and Nb(Ta)-doped systems also show a similar pattern to that of exhibited by the partial occupation of DOS.

3.2 Calculation Methods and Structural Details

Our electronic structure calculations were performed in the framework of density functional theory using the Vienna *Ab-Initio* Simulation Package. [167] The spin-polarized generalized gradient approximation (GGA) parameterized by Perdew-Burke-Ernzerhof (PBE) [98] plus on-site Coulomb interaction approach (GGA+U) was applied for the exchange-correlation functional with U = 5.8 eV and 7.5 eV for Ti 3d and La 4f orbitals, respectively. The U value for Ti 3d states calculated from the constrained density functional theory [168] was proven accurate enough to provide a realistic description of the Ti 3d states. [152, 166, 169] The applied U value on La 4f electrons in this study is also suitable as discussed in prior work. [170, 171] It is well-known that the on-site Coulomb repulsion energy U is much smaller for 4d and 5d electrons than for 3d electrons because the 4d and 5d orbitals are less localized. [172] The prior work shows that for the system with the co-existence of the Ti 3d and Nb 4d (Ta 5d) electrons, in which the electronic properties of the material system are mainly determined by Ti 3d orbitals, the U values for the 4d/5d orbitals can be neglected. [166]Hence, in this work, no U values are applied for Nb 4d and Ta 5d orbitals. The cut-off kinetic energy of 450 eV was used for the electronic wave function expansion. A $10 \times 10 \times 1$ k-space grid with 21 points in the irreducible wedge of the Brillöuin zone was found to converge appropriately. All crystal structures were optimized by minimizing the atomic forces upto 0.02 eV/Å, and self-consistency was assumed for a total energy convergence of less than 10^{-5} eV. A Gaussian smearing of 0.05 eV was used for density of states (DOS) calculations.

The parent compounds LAO and STO crystallize in cubic structures with space group no. 221 ($Pm\bar{3}m$). The experimental lattice parameters and energy gaps of these compounds are 3.789 Å/3.905 Å and 5.6 eV/3.2 eV for LAO and STO, respectively. [138] The calculated band gaps within the GGA+U scheme were 3.12 and 2.29 eV for LAO and STO, respectively. These values are underestimated compared to the experimental values and can be correctly

predicted using hybrid functional calculations. [173–176] However, the underestimation of the band gap has no influence on our conclusions regarding the interfacial metallic states because the Ti 3*d* electronic states forming the metallic states can be well reproduced from the GGA+*U* calculations. [152, 166, 169] Moreover, previously it was confirmed that both the GGA+*U* [160] and HSE06 [177] methods produced similar electronic properties regarding 2DEG in LAO/STO HS system. This indicates that the GGA+*U* approach is acceptable in estimating the Ti 3*d*-orbitals related electronic states. A supercell approach is used to model the $(LAO)_{6.5}/(STO)_{11.5}$ HS, where the subscripts 6.5 and 11.5 denote the number of unit cells of LAO and STO, respectively. The supercell is a single unit cell wide in the *a*- and *b*-directions, and contains two periodic *n*-type $(TiO_2)^0/(LaO)^{+1}$ symmetric interfaces. The experimental lattice constant of STO, 3.905 Å, is fixed in the *ab*-plane to construct all the HS systems, which lead to a lattice mismatch of 2.97% between the LAO film and the STO substrate. The Nb (Ta)-doped LAO/STO HS are modeled by replacing Ti (Nb@Ti)/(Ta@Ti) and Al (Nb@Al)/(Ta@Al) cations with Nb (Ta) near the interfacial region. Given that two symmetric interfaces are present in the periodic model, two such doped layers were introduced. This amounts to an intra-layer doping concentration of 100%, corresponding to the layer-doping model. [154, 162–164, 178] In fact, recent experimental work shows that the layer doping can be experimentally feasible via atomic layer control, which can be one effective approach to tune electronic properties for new functionalists in the designed HS. [154, 164, 178]

3.3 Results and Discussion

3.3.1 Structural Relaxation and Energetic Stability

It was already known that there is a significant octahedral distortion near the interfacial region of the LAO/STO HS, which substantially influence the interface electronic states. [170, 179–181] To properly investigate this distortion, it is necessary to relax the undoped and doped

Table 3.1: Calculated Ti−O, Nb−O, Ta−O bond length (Å) along the *c*-axis, La−O bond length (Å) along the *ac*-plane and O−Ti−O, O−Nb−O, and O−Ta−O bond angles in the *ab*-plane near the interfacial region for undoped and Nb(Ta)-doped LAO/STO HS systems.

Bond	Undoped	Nb@Ti	Ta@Ti	Nb@Al	Ta@Al
Ti−O	2.04	-	-	2.16	2.19
Nb−O	-	2.11	-	-	-
Ta−O	-	-	2.14	-	-
La−O	2.72	2.86	2.83	2.59	2.53
O−Ti−O	172.4^o	-	-	169.4^o	167.9^o
O−Nb−O	-	175.2^o	-	-	-
O−Ta−O	-	-	174.3^o	-	-

HS systems. We accomplished this by fixing the *ab*-plane lattice parameters to that of the STO substrate (3.905 Å), while relaxing the atomic positions along the *z*-direction until the atomic forces were below 0.02 eV/Å. This approach has been used successfully on undoped LAO/STO systems in the past, mirroring experimental electronic properties quite well. [152, 160, 161] The calculated Ti−O, Nb−O, Ta−O bond distances along the *c*-axis, La−O bond distances in the *ac*-plane, and O−Ti−O, O−Nb−O, and O−Ti−O bond angles in the *ab*-plane near the interfacial regions are listed in Table 1 for undoped and Nb(Ta)-doped LAO/STO HS systems. In the Nb@Ti, Ta@Ti, Nb@Al, and Ta@Al doped systems, interfacial Nb−O, Ta−O, and Ti−O bond distances increased by 0.07, 0.10, 0.12, and 0.15 Å, respectively, compared to Ti-O bond in the undoped system. In contrast, the interfacial O−Nb−O and O−Ta−O bond angles decreased by 2.8^o and 1.9^o for the Nb@Ti and Ta@Ti doped systems, respectively, compared to O−Ti−O bond angle in undoped LAO/STO system. Similarly, O−Ti−O bond angles decreased by 3.0^o and 4.5^o for Nb@Al and Ta@Al doped systems. This means that TiO_6 octahedra is more distorted near the interfacial region when Ta is doped at the Al site (Ta@Al) than that of all the other doped and undoped LAO/STO HS systems. On the other hand, interfacial La−O bond distance along the *ac*-plane in the Nb@Al and Ta@Al doped systems substantially decreases by 0.13 and 0.19 Å, respectively, with respect to that of the undoped system, suggesting that the interfacial La−O bond becomes stronger if Nb or Ta substitutes on Al sites. In contrast, substitution of Nb or Ta on

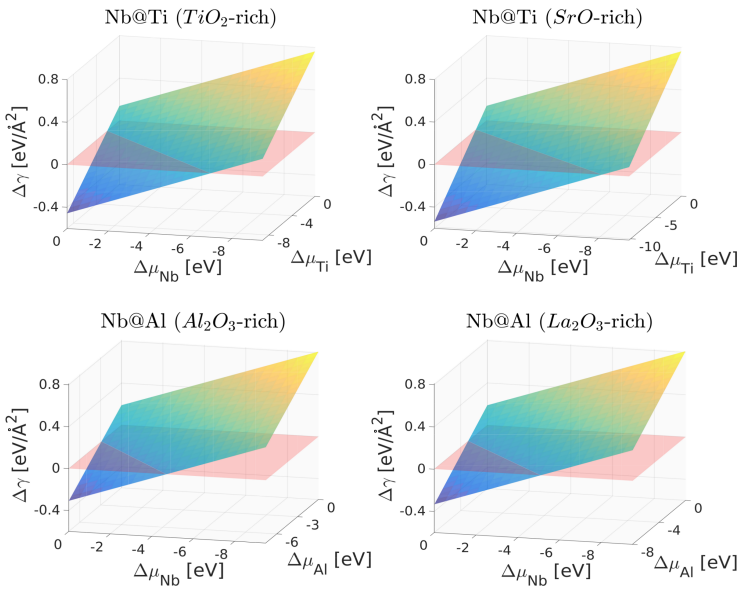

Figure 3.1: Calculated change of the interfacial energy between Nb@X (X=Ti and Al) doped and undoped LAO/STO HS systems. The Nb@Ti doping (top row) was considered under TiO_2 and SrO-rich conditions, respectively. The Nb@Al doping (bottom row) was considered under Al_2O_3 and La_2O_3-rich conditions, respectively. The translucent red plane delineates $\Delta\gamma = 0$, the value below that means that doping is energetically favorable.

Ti sites appears to weaken the La-O bonds as interfacial La$-$O bond length increases by 0.14 and 0.11 Å in the case of Nb@Ti and Ta@Ti doped HS systems, respectively.

Next we evaluated the change of interfacial energetics between the undoped and Nb(Ta)-doped LAO/STO systems under various thermodynamic conditions using the following formula:

$$\Delta\gamma = \gamma_{Nb@X} - \gamma_{undoped} \tag{3.1}$$

where $\Delta\gamma$ is the interfacial energy difference between the Nb-doped ($\gamma_{Nb@X}$) and undoped ($\gamma_{undoped}$) LAO/STO systems (at 0 K) and X is the host ions that Nb replaces (X = Sr, Ti, La, and Al). If $\Delta\gamma$ is less than zero, it means the doped LAO/STO system is energetically more favorable than the undoped system, that is, the doped system can be formed spontaneously. If $\Delta\gamma$ is larger than zero, it indicates that the doped LAO/STO system is energetically less favorable than the undoped system, that is, the doped system cannot be formed. As seen in the following

equation, $\Delta\gamma$ depends on two variable chemical potentials (that of the dopant and host ions) which themselves depend on the thermodynamic condition. [162, 182]

$$\Delta\gamma = (E_{HS}^{Nb@X} - E_{HS}^{undoped} + 2\mu_X - 2\mu_{Nb})/2A \tag{3.2}$$

$E_{HS}^{Nb@X}$ and $E_{HS}^{undoped}$ represent the total energies of the doped and undoped HS systems, respectively. It is noted here that all energies used to determine the thermodynamic stability were derived from standard DFT calculations (without applying U parameters). μ_X (X = Sr, Ti, La, or Al) is the chemical potential of the host ion, while μ_{Nb} is the chemical potential of the Nb dopant. A is the interfacial area, while the factor of 2 preceding is due to the presence of two symmetrical interfaces in our model. Similarly, the factor of 2 preceding the chemical potentials indicates that two interfacial host ions are replaced by Nb.

Let us begin by considering the case of substitutional doping within the STO portion of the interface. As mentioned above, $\Delta\gamma$ is not fixed but depends on the chemical potentials of the dopants and host ions. In fact, the chemical potentials of the relevant elements are determined by the synthesis process in the experiment. In the STO portion, the chemical potentials of various elements are linked by its thermodynamic equilibrium condition:

$$\mu_{Sr} + \mu_{Ti} + 3\mu_O = E_{STO} \tag{3.3}$$

where μ_{Sr}, μ_{Ti}, and μ_O represent the chemical potentials of Sr, Ti, and O, while E_{STO} refers to the total energy of STO formula unit. It is important to note that for any particular dopant substitution, only the chemical potential of the displaced host ion is used in Equation 2. Determining this chemical potential at specific thermodynamic conditions, however, often requires consideration of the other linked chemical potentials as well. To avoid confusion regarding the chemical potential references, we have included the following definitions:

$$\Delta\mu_{Sr} = \mu_{Sr} - E_{Sr} \tag{3.4}$$

$$\Delta\mu_{Ti} = \mu_{Ti} - E_{Ti} \tag{3.5}$$

$$\Delta\mu_{O} = \mu_{O} - \frac{1}{2}E_{O_2} \tag{3.6}$$

E_{Sr} and E_{Ti} are the per-atom energy of the most stable low-temperature phases of elemental Sr and Ti, while E_{O_2} is the total energy of the isolated ground state O_2 molecule, both at 0 K. The formation enthalpy of STO is defined as:

$$\Delta H_f(STO) = E_{STO} - E_{Sr} - E_{Ti} - \frac{3}{2}E_{O_2} \tag{3.7}$$

which, using the aforementioned definitions, can also be written in the following form:

$$\Delta H_f(STO) = \Delta\mu_{Sr} + \Delta\mu_{Ti} + 3\Delta\mu_{O} \tag{3.8}$$

In fact, this equation must be satisfied to guarantee the stability of STO. Similar equations can be developed for LAO, which are relevant when considering substitutional doping within the LAO portion of the interface.

Returning to the interfacial energy difference (Equation 2), it is important to note that, experimentally, μ_X and μ_{Nb} strongly depend on the material growth conditions. Therefore, we considered a series of thermodynamic conditions and determined the relevant chemical potential ranges within those conditions. The specific conditions considered are: SrO-rich, TiO_2-rich, Al_2O_3-rich, and La_2O_3-rich. The former two conditions are relevant when considering doping on the STO side, while the latter two are used for doping at the LAO side. By using the definitions (4)-(6), the Equation 2 can be further rewritten as below:

$$\Delta\gamma = [E_{HS}^{Nb@X} - E_{HS}^{undoped} + 2(\Delta\mu_X - \Delta\mu_{Nb}) + 2(E_X - E_{Nb})]/2A \tag{3.9}$$

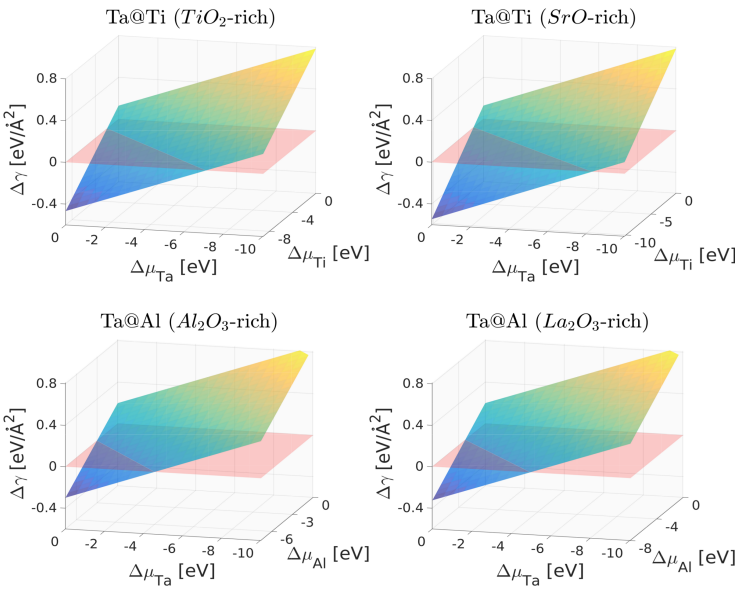

Figure 3.2: Calculated change of the interfacial energy between Ta@X (X=Ti and Al) doped and undoped LAO/STO HS systems.

As an example let us consider Nb@Ti doping in the SrO-rich case. Under SrO-rich conditions, the following equation is always satisfied:

$$\Delta H_f(SrO) = \Delta\mu_{Sr} + \Delta\mu_O \tag{3.10}$$

By splitting the SrO-rich condition into sub-conditions (O-rich, *i.e.,* $\Delta\mu_O$=0 and Sr-rich, *i.e.*, $\Delta\mu_{Sr}$=0) using thermodynamic laws, we were able to determine that the theoretical value of $\Delta\mu_{Ti}$ in the range of -10.3 eV $\leq \Delta\mu_{Ti} \leq 0$ eV. The range for $\Delta\mu_{Nb}$ can be determined more simply. To avoid the competitive formation of secondary dopant oxide Nb_2O_5, $\Delta\mu_{Nb}$ and $\Delta\mu_O$ must satisfy the following condition: $2\Delta\mu_{Nb} + 5\Delta\mu_O < \Delta H_f(Nb_2O_5)$, from which a useful $\Delta\mu_{Nb}$ range can be derived. Together, the ranges for $\Delta\mu_{Ti}$ and $\Delta\mu_{Nb}$ can be used to determine boundary values of $\Delta\gamma$(Nb@Ti) under SrO-rich conditions. We used a similar procedure to calculate $\Delta\gamma$ for substitutional doping of Nb/Ta at interfacial Ti, Al, Sr, or La atoms under two thermodynamic conditions each. Our results for Nb and Ta doping at Sr/La sites are shown in Fig. 1S and 2S of the Supporting Information, respectively, indicate that these substitutions are extremely unfavorable,

hence they are not considered further in our work. The results for Nb@Ti and Nb@Al doping are plotted in Fig. 1, while the results for Ta@Ti and Ta@Al doping are plotted in Fig. 2. Several important conclusions can be drawn:

(i) There is very little difference in the energetic favorability of Nb- and Ta-doped interfaces, and either dopant can be stably doped at the LAO/STO interface.

(ii) Of the two viable interfacial doping sites considered, substitutional doping by Nb/Ta is more favorable at the Ti site than that at Al site. In other words, substitution at Ti yields a more stable interface under a wider range of chemical potentials than substitution at Al. However, doping at either site under appropriate thermodynamic conditions can create a more stable interface than in the undoped system.

(iii) Doping at Ti is more favorable under SrO-rich than that under TiO_2-rich conditions, while doping at Al is (slightly) more favorable under La_2O_3-rich than Al_2O_3-rich conditions.

In addition, we also carried out a group of test calculations to evaluate the relative stability of the dopant at a layer different to the interface. Our results show that the Nb@Al and Ta@Al doping at the interface is energetically more favorable than the layer doping far away from the interface, while for the Nb@Ti and Ta@Ti doping, the two layer doping models, *i.e.*, one at the interfacial layer and the other one at the layer far away from the interface have comparable stability. This indicates the interfacial Nb and Ta layer doping is experimentally feasible.

3.3.2 Electronic Structure

Here, we investigated the effects of Nb and Ta-doping on the electronic properties of *n*-type LAO/STO HS systems. First, we will provide some insight on the electronic properties of undoped LAO/STO system for comparison, then study the doped systems. It is well-established that 2DEG is primarily derived from the Ti 3*d* orbitals of the first (IF-I) TiO_2 layer of the STO substrate for undoped LAO/STO HS system, along with a small contribution from the third (IF-III) layer near the Fermi level. [152, 161, 163] The fifth (IF-V) layer has almost no contribution and

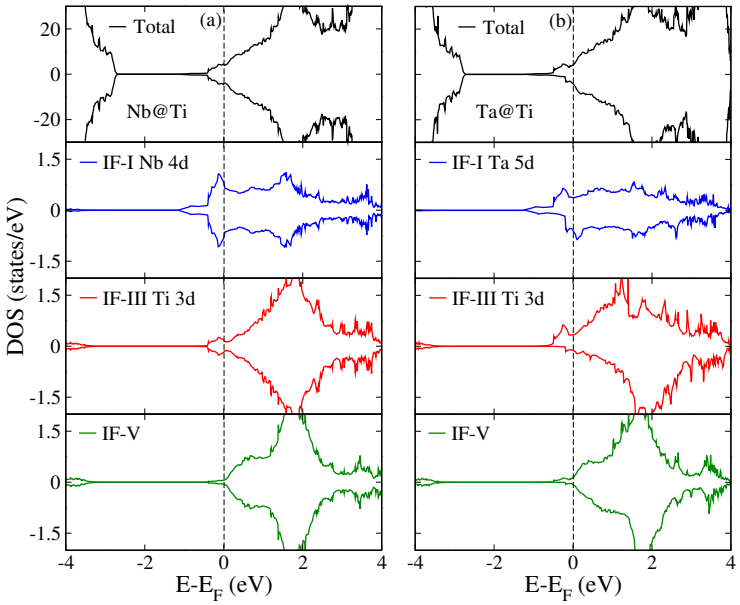

Figure 3.3: Calculated spin-polarized total and partial DOS projected on Ti 3*d*, Nb 4*d*, and Ta 5*d* orbitals near the interfacial region of the STO substrate for (a) Nb@Ti and (b) Ta@Ti doped LAO/STO HS systems. The IF-I, IF-III, and IF-V represent the first, third and fifth layers in the STO substrate, respectively. The Fermi level is indicated by the vertical dashed line at 0 eV.

the other layers away from the interface show an insulating behavior, which shows the typical two-dimensional character of the 2DEG. The width of the metallic region in this abrupt LAO/STO HS system is around 10 Å along the *c*-axis (about 3 unit cells of the STO). The interfacial (IF-I) TiO_2 layer exhibits a nearly half-metallic nature with a magnetic moment of 0.38 μ_B on the Ti atom. The calculated magnetic moment of the Ti atom in the IF-III TiO_2 layer is 0.08 μ_B and all other layers further away from the interface exhibit no spin-polarization. [152, 161, 163] For reference, the DOS and layer-resolved DOS of the undoped LAO/STO superlattice system are provided in Fig. 3S the Supporting Information.

To illustrate the effects of Nb and Ta-doping on the electronic properties of the 2DEG in LAO/STO HS, we calculated total and partial DOS projected on Ti 3*d*, Nb 4*d*, and Ta 5*d* orbitals near the interfacial region for Nb@Ti and Ta@Ti doped LAO/STO HS systems in Fig. 3. Total DOS for Nb@Ta (Fig. 3a) and Ta@Ti (Fig. 3b) doped HS systems exhibit typical *n*-type conductivity as found in the case of the abrupt interface and more occupied states near the Fermi

energy are found compared to that of the undoped system. [152, 161, 163] This phenomena can be understood by analyzing the valence states of the dopant. The Nb and Ta atoms typically adopt a +5 valence state, which can be inferred from their respective electron configurations of $4d^4 5s^1$ and $5d^3 6s^2$ fillings. When these atoms replace an interfacial Ti^{4+} atom ($3d^2 4s^2$) in the STO substrate, one free electron will be injected into the system. Our results, however, indicate that Nb and Ta atoms are not in perfect +5 states after doping since some Nb 4*d* and Ta 5*d* orbitals are occupied, and therefore only a small fraction of free electrons are actually added to the system. Nevertheless, these free electrons still increase the orbital occupation number near Fermi energy, and lead to higher charge carrier density in the doped HS systems compared to the undoped LAO/STO system, as shown below. Moreover, it is found that when Ta is doped at the Ti site (Fig. 3b), the orbital occupation of the total DOS is higher than that of the Nb@Ti (Fig. 3a) doped system, because 5*d* orbital is more de-localized than 4*d* orbital. Therefore, the Ta atom releases more free electrons to the system than the Nb atom. From the partial DOS, one can also see that Nb 4*d* and Ta 5*d* orbitals are also crossing the Fermi level and significantly contributing to the interfacial conductivity. The 2DEG spans only 2 unit cells of the STO substrate, while Ti atoms from the third (IF-III) TiO_2 layers showing a very small orbital occupation. Surprisingly, our results further indicate that when Nb is doped at the Ti site (Fig. 3a), the system shows no spin-polarization, as spin-up and spin-down channels have the identical DOS compared to Ta@Ti (Fig. 3b) doped and undoped LAO/STO HS systems. [152, 161, 163]

Fig. 4a and 4b represent the total and partial Ti 3*d*, Nb 4*d*, and Ta 5*d* DOS for Nb@Al and Ta@Al doped LAO/STO HS systems, respectively. Our results exhibit that when Nb and Ta atoms substitute for Al, more electrons are added to the system than in the case of Nb@Ti (Fig. 3a) or Ta@Ti (Fig. 3b) doping. This is due to the different valence states of the substituted atoms: Al^{3+} versus Ti^{4+}. That is to say, the Nb@Al (Ta@Al) doping can release one more electron into the LAO/STO HS system than the Nb@Ti (Ta@Ti) doping. Thus substitution at Al substantially enhances the 2DEG orbital occupation near the Fermi energy, charge carrier density,

and magnetism of the system. The extra free electrons provided by the Nb and Ta atoms reside almost entirely at the interfacial Ti atoms, see Fig. 4a and 4b. Fig. 4b (Ta@Al) shows that partial occupation of the total and interfacial Ti atoms (IF-I) is higher than that of the Nb@Al doped system (Fig. 4a). This means that the Ta atoms release more free electrons to the system than the Nb dopant, as found in the previous doped systems (discussed in Fig. 3). The Nb 4*d* and Ta 5*d* states cross the Fermi level and contribute to the interfacial conductivity, similar to Nb@Ti and Ta@Ti LAO/STO doped systems. In both doped systems, the partial DOS also indicates that electrons are confined almost within 1.5 unit cells of the STO substrate along the *c*-direction, which is almost half the width of metallic region in the undoped LAO/STO system. [152,161,163] This means that electron transfer from the polar $(LaO)^{+1}$ layer and the Nb/Ta atoms extends only as deep as the nonpolar $(TiO_2)^0$ IF-III layer of the substrate, with transfer to all deeper layers strongly restricted. Therefore, in the doped systems, mobile electrons reside in the first two unit cells of the STO substrate. Finally, one can notice that the shapes of the DOS in these doped system is very different from that of the undoped LAO/STO HS system. [152, 160, 161, 163] This is because, besides the d_{xy} orbital, d_{yz} orbital of Ti ions also contribute to the formation of the 2DEG, which lead to the different shape of the DOS. More detail behind this phenomenon will be discussed later.

Fig. 5 shows the band structure along the Brillouin Zone path M-Γ-X for all the doped and undoped HS systems. It clearly shows that Nb(Ta)@Ti doping leads to additional occupied bands relative to the undoped system, while Nb(Ta)@Al doping causes more occupied bands. As discussed above, this can be easily understood when considering the valence states of the dopant and host atoms: $Nb(Ta)^{+5}@Ti^{+4}$ doping leads to approximately one free electron per dopant atom, whereas $Nb(Ta)^{+5}@Al^{+3}$ leads to roughly two free electrons per dopant atom. To partially evaluate the Nb(Ta) doping influence on the charge carrier mobility, we then calculated the relative electron effective masses (m_e^*/m_0) using parabolic effective-mass approximation for the minimum conduction bands from M to Γ, i.e, the highlighted bands in the Fig. 5. m_0 refers to

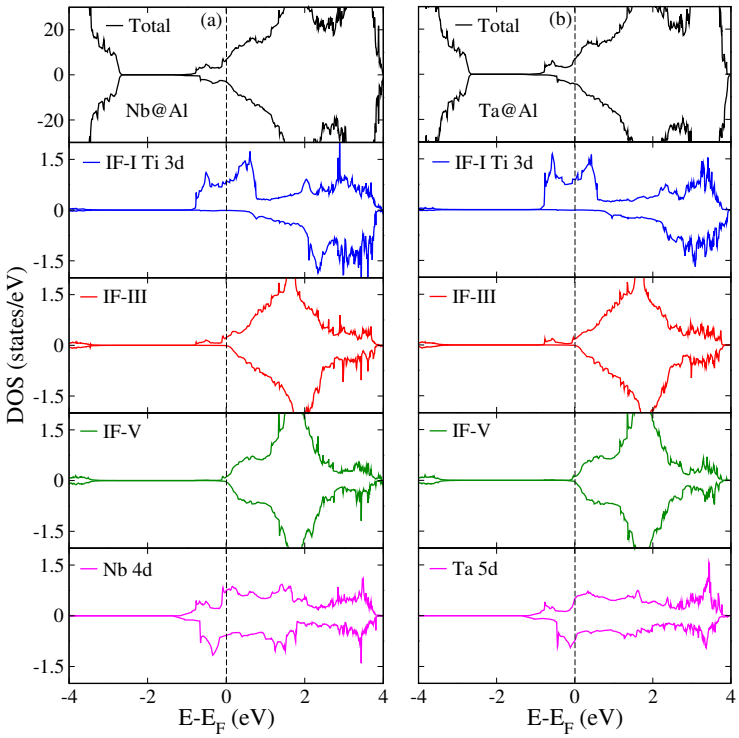

Figure 3.4: Calculated spin-polarized total and partial DOS projected on Ti 3*d*, Nb 4*d*, and Ta 5*d* orbitals near the interfacial region of the STO substrate for (a) Nb@Al and (b) Ta@Al doped LAO/STO HS systems.

the free electron rest mass. For comparison, we also calculated the relative effective mass for the undoped LAO/STO system. The calculated value for the undoped system is 0.59, which is in a good agreement with the previous reported value. [183–185] Note that the calculated effective mass value cannot be directed related to the the absolute electron mobility in the experiment. Rather, it is included as a baseline to which the doped results may be compared, which can provide us a qualitative evaluation whether the Nb and Ta doping can change the electron effective mass and the resulting electron mobility. The calculated relative effective masses for Nb@Ti, Ta@Ti, Nb@Al, and Ta@Al doped systems are 0.36, 0.41, 0.56, and 0.58, respectively. These results indicate that Nb@Ti and Ta@Ti doping can reduce the electron effective mass with respect to that of the undoped system and thus potentially improve the electron mobility, while Nb@Al and Ta@Al doping yield comparable effective mass with that of the undoped system and thus is not beneficial for improving the electron mobility.

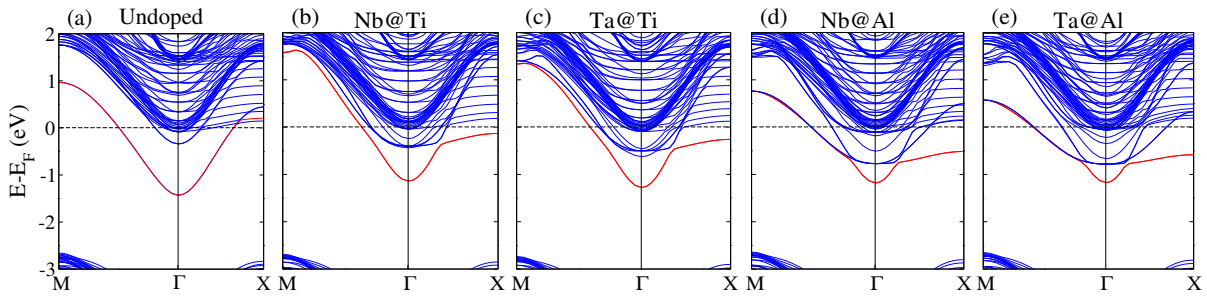

Figure 3.5: Calculated band structure for undoped and Nb(Ta)-doped LAO/STO HS systems. The red highlighted lines indicate the specific band used for each of our effective mass calculations.

3.3.3 Electron Carrier Density and Interfacial Magnetic Moment

For a qualitative comparison of the various Nb and Ta-doped systems, we determined their total charge carrier density (a) and magnetic moments on Ti atoms near the interfacial region (b) in Fig. 6. To do this, we computed the partial occupation by integrating the conducting states of the total DOS below the Fermi level and then continued to calculate the charge carrier density in each case. The estimated values of occupation numbers and their corresponding charge carrier densities are plotted in Fig. 6a for undoped and Nb(Ta)-doped LAO/STO HS systems. Our calculations show that the highest orbital occupation numbers and charge carrier densities are achieved in Ta@Al doped LAO/STO HS system. As we mentioned above, this happens because when Ta replaces Al, it donates more extra electrons to the system compared to Nb@Al doping, which extensively increases the orbital occupation number of DOS near the Fermi energy (Figure 4b) and hence, raises the charge carrier density. Similarly, the estimated occupation number of Ti atom from interfacial TiO_2 layers in the STO substrate for Nb@Al and Ta@Al doped LAO/STO HS systems are 0.57 and 0.74, respectively, and the corresponding electron carrier densities are 3.7×10^{14} cm^{-2} and 4.9×10^{14} cm^{-2}, larger than that in the undoped superlattice model of about 1.9×10^{14} cm^{-2}. [152] These results also confirm that Ta atoms release more electrons into the system compared to Nb and that these electrons primarily reside at the interfacial Ti atoms, as shown in Fig. 4.

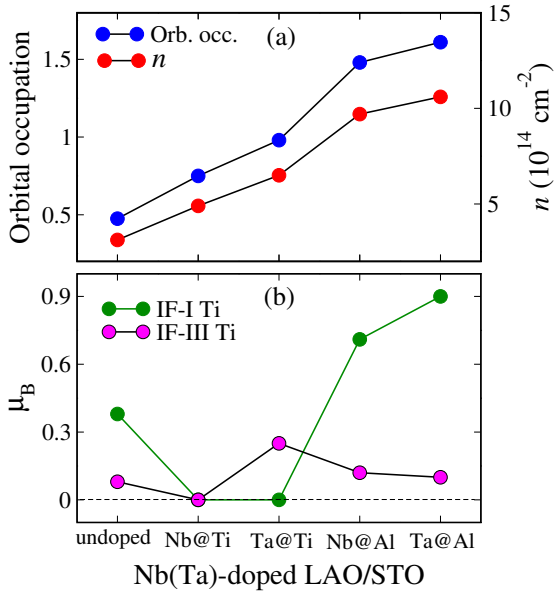

Figure 3.6: Calculated (a) total orbital occupation (Orb. occ.) numbers (blue) and corresponding charge carrier densities n (red) and (b) total magnetic moments in undoped and Nb(Ta)-doped LAO/STO HS systems.

Next, we study the effects of Nb and Ta-doping on the magnetic moments of interfacial Ti atoms in the above mentioned doped HS systems. It is very well known that magnetic moments on interfacial Ti atoms are caused by the partially occupied Ti 3*d* orbitals. [152,161,163,186,187] Therefore, we plotted local magnetic moments on Ti atoms from the IF-I and IF-III TiO_2 layers for undoped and Nb(Ta)-doped LAO/STO HS systems in Fig. 6b. The system with Ta-doping at the Al site (Ta@Al) has the largest interfacial (IF-I) Ti magnetic moments compared to undoped and other doped LAO/ST HS systems. For the Nb@Al and Ta@Al doped LAO/STO HS systems, the Ti atoms in IF-III TiO_2 layers show very small spin-polarization with magnetic moments of 0.12 μ_B and 0.10 μ_B, respectively. This is because less electrons transfer to the IF-III layers than that to the IF-I from the LaO layer and also from Nb/Ta doped atoms. The TiO_2 layers further away from the interface in the STO substrate show no spin-polarization. For the Ta@Ti doped system, a significant magnetic moment of 0.25 μ_B is also found in the third (IF-III) layer, while Nb@Ti doped system exhibits no spin-polarization as reflected in the DOS of Fig. 3a.

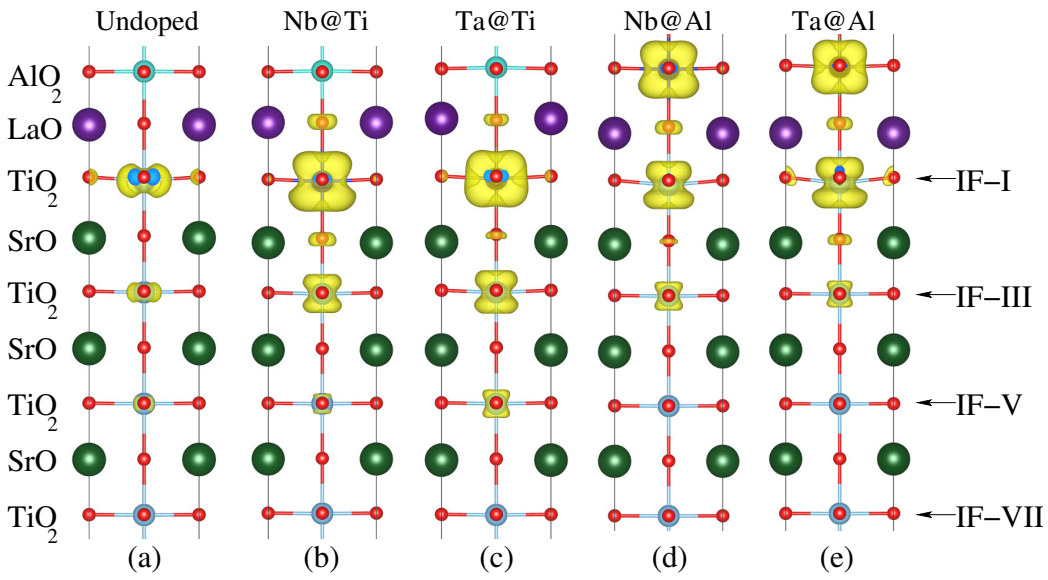

Figure 3.7: Charge density projected on the bands forming the metallic states near the interfacial region for undoped (a), Nb@Ti (b), Ta@Ti (c), Nb@Al (d), and Ta@Al (e) doped LAO/STO HS systems.

3.3.4 Three-Dimensional Charge Density

To gain deep insight into the interfacial metallic states and to visualize the charge transfer effects in the Nb (Ta)-doped LAO/STO systems, we plotted the three-dimensional charge density projected on the bands forming the 2DEG for undoped (a), Nb@Ti (b), Ta@Ti (c), Nb@Al (d), and Ta@Al (e) doped LAO/STO HS systems in Fig. 7. Our results clearly demonstrate that in the undoped LAO/STO HS system, electrons from the polar $(LaO)^{+1}$ layer are mainly transferred to IF-I and IF-III $(TiO_2)^0$ layers of the STO substrate, along with a minor distribution on the IF-V layer (see Fig. 7a), which means that the 2DEG extends within 3 unit cells of the STO substrate along the *c*-axis, indicating a typical two-dimensional character of conducting states.

In the case of Nb@Ti (Fig. 7b) and Ta@Ti (Fig. 7c) doped systems, 2DEG primarily comes from interfacial Nb and Ta atoms, along with a substantial contribution from the IF-III TiO_2 layers. Interestingly, it is noted that the density of Ti atoms in the second TiO_2 layer (IF-III) is higher in Ta@Ti doped system than in the Nb@Ti system. The third TiO_2 layer (IF-V) in the Nb@Ti doped system has almost no contribution to the interface conductivity, yet in the Ta@Ti

doped system it contributes significantly. This difference implies that a few electrons transfer to the deeper STO substrate, consistent with the calculated partial DOS in Fig. 3. One reason is probably because that Ta 5*d* orbitals are less localized than Nb 4*d* and thus the Ta 5*d* orbitals hold less electrons, and the remaining electrons are further transferred to deep TiO_2 layers. As discussed below, another reason is because the structural distortion of the TiO_6 octahedra near the interface in the Ta@Ti system is stronger than that in the Nb@Ti system. For the Nb@Al (Fig. 7d) and Ta@Al (Fig. 7e) doped LAO/STO, the conducting metallic states are mainly contributed by the Nb and Ta atoms, and the interfacial TiO_2 layer (IF-I) in each system.

Table 3.2: Calculated O-Ti-O bond angles in the *ab*-plane at IF-III and IF-V TiO_2 layers for undoped, Nb@Ti, Ta@Ti, Nb@Al, and Ta@Al doped LAO/STO HS systems.

	Undoped	Nb@Ti	Ta@Ti	Nb@Al	Ta@Al
IF-III	177.6^o	177.5^o	175.5^o	178.8^o	179.3^o
IF-V	178.7^o	178.8^o	177.9^o	179.3^o	179.5^o

The spatial extension of the 2DEG along the *c*-direction strongly depends on TiO_6 octahedral distortion in the STO substrate. To elucidate this distortion in our systems, we calculated the O−Ti−O bond angles in the *ab*-plane at the IF-III and IF-V TiO_2 layers for undoped, Nb@Ti, Ta@Ti, Nb@Al, and Ta@Ti doped LAO/STO HS systems in Table 2. One can clearly see that the TiO_6 octahedra are distorted up to the 3rd TiO_2 layer (IF-V) in the case of the undoped and Nb@Ti doped LAO/STO HS systems. Therefore, charge transfer from the polar $(LaO)^+$ layer to nonpolar $(TiO_2)^0$ layers extends to 3 unit cells of the STO substrate as shown in our charge density plot (Fig. 7a). Similarly, TiO_6 octahedra are distorted up to 3 unit cells of the STO substrate in the Ta@Ti doped system (Fig. 6c), but in the fifth (IF-V) layer the degree of distortion is higher than in the undoped and Nb@Ti doped systems (Fig. 7a and 7b). Therefore, more charge is transferred to the IF-V TiO_2 layer in this case, consistent with the DOS in Fig. 3. On the other hand, for the Nb@Al and Ta@Al doped HS systems, very small TiO_6 octahedral distortions are found at the IF-III TiO_2 layer, with almost negligible distortions at the

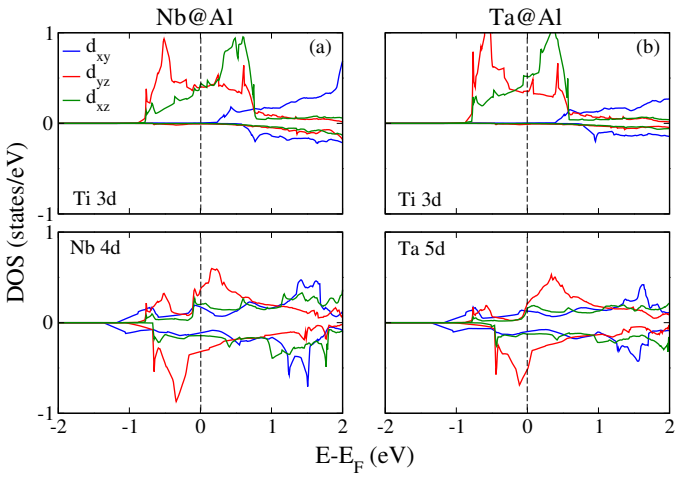

Figure 3.8: Orbital-resolved interfacial (IF-I) Ti 3d, Nb 4d, and Ta 5d DOS in Nb@Al (a) and Ta@Al (b) doped LAO/STO HS systems.

IF-V TiO_2 layers. Hence, less charge migrates to deeper TiO_2 layers and a highly confined 2DEG is obtained. Moreover, the density on the Ti atoms in the interfacial TiO_2 layer (IF-I) is larger in the Ta@Al doped system than in the Nb@Al system, which means higher orbital occupation and higher charge carrier density. This is because TiO_6 octahedra is more distorted at the interfacial (IF-I) TiO_2 layer for the Ta@Al doped system than in the undoped and Nb@Al doped LAO/STO HS systems. In short, the Nb and Ta doping at Al sites can significantly modify the electron transport properties of the LAO/STO HS system.

In addition, from the Fig. 6 (charge density), one can see that the occupied Ti 3*d* orbitals in the STO substrate differ in shape compared to the undoped HS system. [152, 161, 163] This means that the 3*d* bands, which form the 2DEG in doped LAO/STO HS systems, have different orbital occupations. To verify this difference, we plotted the orbital-resolved DOS of Ti 3*d*, Nb 4*d*, and Ta 5*d* states for the Nb@Al (a) and Ta@Al (b) doped LAO/STO HS systems in Fig. 8. As previous results [152, 161, 163, 188, 189] indicate, 2DEG resides in the *ab*-plane in the undoped LAO(LTO)/STO HS systems and only the d_{xy} orbitals of interfacial Ti atoms cross the Fermi level, while the d_{yz}/d_{xz} orbitals remain unoccupied. This can be explained in the context of crystal field theory. It is well known that in a regular octahedral crystal field, Ti 3*d* states are split into

triply t_{2g} (d_{xy}, d_{xz}, and d_{yz}) and doubly e_g ($d_{3z^2-r^2}$ and $d_{x^2-y^2}$) degenerate states. After structural relaxation, the TiO_6 octahedral distortion results in a degraded symmetry. Therefore, the triply degenerate t_{2g} states are split into non-degenerate d_{xy}, d_{yz}, and d_{xz} orbitals, and the transferred electron eventually occupies the low-energy d_{xy} orbitals. For comparison, the orbital-resolved DOS of interfacial (IF-I) Ti atoms for Nb@Al (a) and Ta@Al (b) doped LAO/STO HS systems is shown in Fig. 7. For Nb@Al (Fig. 7a) and Ta@Al (Fig. 7b), one can clearly see that the metallicity results from the admixture of d_{yz} and d_{xz} instead of d_{xy} orbitals, while d_{xy} orbitals remain unoccupied and stay at higher energies in the conduction band (far away from the Fermi level). Therefore, the 2DEG resides in the yz and zx, rather than xy, plane, the reverse of what is usually observed in undoped STO-based HS systems. [152, 161, 163, 188, 189] In contrast, both the d_{xy}, d_{xz}, and d_{yz} orbitals of Nb 4d and Ta 5d contribute to the interfacial conductivity.

3.4 Conclusions

In summary, first-principles density functional theory calculations were performed to investigate the Nb (Ta) doping effects on the interface energetics and electronic properties of 2DEG in LAO/STO HS system. Our calculations reveal that LAO/STO HS systems with Nb@Ti and Ta@Ti doping are energetically more favorable than the undoped and other doped ones. We found that Nb(Ta)@Ti and Nb(Ta)@Al doping significantly improve the orbital occupation near the Fermi level, and produce a high interfacial charge carrier density. This is mostly attributed to the additional free electrons provided by Nb(Ta) dopant, and these free electrons reside mainly at the Nb(Ta) dopant and the Ti atoms in the interfacial TiO_2 layer of the STO substrate. Our results indicate that the Nb(Ta)@Al doped HS systems exhibit higher interfacial charge carrier density and magnetic moments than the undoped and other doped ones, while the Nb(Ta)@Ti doped HS systems may show higher charge carrier mobility because of the lower electron effective mass. Our theoretical calculations invite a thorough experimental characterization of Nb and

Ta-doped LAO/STO systems to fully understand their thermodynamic stability and electron transport property.

3.5 Acknowledgements

Chapter 3, in full, is a reprint of the material "Nb and Ta Layer Doping Effects on the Interfacial Energetics and Electronic Properties of $LaAlO_3/SrTiO_3$ Heterostructure: First-Principles Analysis" as it appears in Physical Chemistry Chemical Physics. Safdar Nazir, Maziar Behtash, Jianli Cheng, Jian Luo, Kesong Yang, 18, 2379, (2016). The dissertation author was a contributing author for this paper.

Chapter 4

Polarization Effects on the Interfacial Conductivity in the $LaAlO_3/SrTiO_3$ Heterostructure: First-Principles Study

In Chapter 3 we have discussed transition metal layer doping in the $LaAlO_3/SrTiO_3$ (LAO/STO) heterostructure (HS), which can enhance the charge carrier density, magnetism, and spacial confinement of the interfacial two-dimensional electron gas (2DEG). In fact, 2DEG properties can also be enhanced by the application of strain on the STO substrate. For example, Eom *et al*. grew LAO films on strained STO substrates, and found that the sheet carrier density can be increased by the application of biaxial tensile strain. [190] Experiments have also shown that 2DEG does not form in unstrained LAO/STO systems until at least four LAO unit cells have been deposited, which is known as the critical thickness. [143] Interestingly, Eom *et al*. found that biaxial compressive strain increases the critical film thickness to more than four LAO unit cells. Several years earlier Pentcheva *et al*. had proposed that polarization in the LAO overlayers could neutralize the polar catastrophe in LAO/STO, yielding insulating behavior. [191] Subsequently, Moler *et al*. found that uniaxial tensile strain increases the conductivity of LAO/STO HS, and

suggested that strain-induced changes in LAO film polarization perpendicular to the interface could be responsible for this increase. [192] Motivated by these studies, in this Chapter we present a first-principles study of uniaxial strain and polarization in the LAO/STO slab system. We systematically revealed the correlation between LAO film thickness, polarization, and interfacial charge carrier density. In particular, we found that the polarization in the LAO film is strongly dependent on film thickness, and identified a critical polarization value above which the polar catastrophe is neutralized and insulating behavior is observed. In addition, we found that the application of [100] uniaxial tensile strain on the STO substrate can reduce the polarization in the LAO film, and thereby enhance the conductivity of the interfacial 2DEG in LAO/STO. Finally, we discovered that uniaxial strain can change the distribution of charge among the three TiO_2 layers nearest to the interface, with tensile strains increasing the relative concentration of free carriers at the interfacial TiO_2 layer. This work resolves the long-standing discrepancy between the theoretical and experimental charge carrier densities in the LAO/STO 2DEG, and provides fundamental insights into the role of polarization in 2DEG formation.

4.1 Introduction

In the past decade, the two-dimensional electron gas (2DEG) at the *n*-type $(LaO)^{+1}/(TiO_2)^0$ interface in $LaAlO_3/SrTiO_3$ (LAO/STO) heterostructures (HS) has attracted considerable attention for its unique electronic properties and potential applications in nanoelectronic devices. [138, 193–195] When an LAO film is deposited on an STO substrate, the polar discontinuity at the $(LaO)^{+1}/(TiO_2)^0$ interface leads to divergence of the electrostatic potential. To compensate this divergence, according to the polar catastrophe mechanism, [138, 150] $0.5e^-$ is transferred from the polar $(LaO)^{+1}$ layer of LAO to the nonpolar $(TiO_2)^0$ layer of the STO substrate. These electrons partially occupy Ti 3*d* orbitals near the interfacial region, producing a 2DEG with a theoretical charge carrier density of 3.3×10^{14} cm^{-2}. However, systematic

experiments of the oxygen-annealed samples show a sheet carrier density of about $1-2\times10^{13}$ cm^{-2}, [54, 143, 149, 196–198] one order of magnitude smaller than the theoretical value. Some research efforts are still being made to explore a comprehensive model that can account for all the experimental phenomena in the LAO/STO HS. [199, 200] Several possible explanations for this discrepancy have been proposed from various viewpoints. [191, 199–203] For example, from density functional theory (DFT) calculations, Popović *et al.* suggested that the transferred electrons are not only confined at the interfacial TiO_2 layer but also extend over several deeper TiO_2 layers, which dilutes the sheet carrier density. [201] By first-principles electronic structure calculations, Krishnaswamy *et al.* proposed that the sheet carrier density of 3.3×10^{14} cm^{-2} is intrinsic to the LaO/TiO_2 interface in the LAO/STO system, while the AlO_2 terminated surface may transfer electrons from the 2DEG to the surface states, leading to a smaller sheet carrier density at the interface. [200] Pentcheva *et al.*, for the first time, has proposed that the polar distortion in the LAO overlayers on the STO substrate can neutralize the polar catastrophe, leading to the insulating behavior up to five monolayers of LAO. [191] As a results, one may speculate that the polarization, *i.e.*, the polar distortion, in the LAO film may be weak enough when the LAO film is more than five monolayers so that the polar distortion is not capable of fully neutralizing the polar catastrophe. Consequently, a charge transfer less than $0.5e^-$ may occur from the LAO to the STO, which leads to the 2DEG at the interface but with smaller sheet carrier density. This hypothesis may reconcile the discrepancy between the experimental and theoretical sheet charge carrier density in the LAO/STO system if it is true, and thus a systematic computational study on the correlation among the LAO film thickness, LAO film polarization, and the sheet carrier density in the LAO/STO HS system is essential. This partially motivates the work presented in this paper.

Despite the discrepancy between experimental and theoretical sheet charge carrier density, substantial efforts continue to be expended for optimizing the interfacial electron transport properties in the LAO/STO system, in order to realize its potential applications in high-

performance nanoelectronics. For example, it has been shown that transition metal and rare earth metal layer doping can significantly enhance the 2DEG charge carrier density in the LAO/STO HS. [43–45, 135–137, 154, 204] Another potential method to tailor 2DEG properties in LAO/STO HS systems is to apply a strain on the STO substrate. Experimentally, various degrees of strain in the LAO/STO HS can be achieved by growing STO on single-crystal substrates with a lattice mismatch; an LAO film can then be deposited on the strained STO to form the HS. For example, Eom *et al.* grew STO on a variety of substrates before depositing LAO films, demonstrating substantial differences in 2DEG properties with respect to strain. [190] They found that the sheet charge carrier density increases as the STO substrate undergoes a strain from -1.5% to 0.5%, which is consistent with recent first-principles electronic structure calculations. [205] Eom's team also found that the required critical thickness of LAO film to produce 2DEG changes with biaxial compressive strain; specifically, compressive strain requires more than the 4 unit cells of LAO which are normally sufficient in the unstrained case.

Recently Moler *et al.* [192] found that uniaxial tensile strains in either $[100]_p$ or $[010]_p$ directions substantially enhance the local conductivity in LAO/STO HS-based slab systems, but that a simultaneous elongation in both directions (*i.e.* biaxial tensile strain) yields no such increase. The higher conduction is attributed to an increase in either mobility or charge carrier density in the tetragonal domain structure in the STO substrate. The authors speculated that strain-induced changes in the polarization perpendicular to the interface could lead to changes in interfacial conductivity, but more details are necessary to clarify the origin of this behavior. A subsequent first-principles study revealed the role of uniaxial strain in tailoring the interfacial electronic properties using an LAO/STO superlattice model (without vacuum). It was found that uniaxial tensile strain can considerably increase the interfacial charge carrier density, which can partially explain the enhanced conductivity observed in the tetragonal domain structure of the LAO/STO system. [206] Although the periodic superlattice model can well reproduce the polar catastrophe effects, [201, 202, 205] it might not be able to exactly model the LAO/STO interface in

reality. [207] This is mainly because, experimentally, the LAO film is grown on the STO substrate and has a surface polar discontinuity that significantly influences the materials properties. [191] Thus periodic LAO/STO superlattice models cannot accurately model the polarization effects induced by the surface polar discontinuity, *i.e.*, the relative displacement between the cations and anions in the LAO film. In fact, the interfacial conductivity is strongly linked to the polarization in both the film and substrate, [208, 209] and particularly, recent first-principles calculations suggest that strain-induced polarization is responsible for the interfacial conductivity in the $CaZrO_3/SrTiO_3$ HS system. [210] Despite widespread agreement regarding the potential of strain as an optimization tool for 2DEG in HS systems, fundamental and predictive knowledge of its effects, particularly the strain-induced polarization effects, remains elusive. A more systematic study of the influence of strain on the polarization of LAO/STO HS, and the consequent changes of the interfacial conductivity, is therefore essential.

In this work, we employed first-principles electronic structure calculations to investigate the effects of uniaxial [100] strain on the electron transport properties of 2DEG at the *n*-type $(LaO)^{+1}/(TiO_2)^0$ interface in LAO/STO HS slab systems from the perspective of the polarization effects. Here, our main motivation is to examine the effects of uniaxial [100] compressive and tensile strains on the charge carrier density, electron mobility, and conductivity of the 2DEG in the LAO/STO system. We suspect that these effects are mediated in large part by strain-induced changes in the LAO film polarization. Therefore, first we study the unstrained LAO/STO system to establish a clear point of reference, then explore the influence of uniaxial [100] strain on the electronic properties of 2DEG in the LAO/STO HS slab system. To the best of our knowledge, this is the first theoretical work which clearly explains the polarization mechanisms influencing the enhanced charge carrier density, mobility, and conductivity of 2DEG in the uniaxially tensile strained LAO/STO system. This conclusion is in excellent agreement with recent experimental finding, where higher local conductivity is observed in the uniaxial tensile strained system. In contrast, the compressively strained systems show less favorable electron transport properties

than the unstrained LAO/STO HS system.

4.2 Calculation Methods and Structural Details

Spin-polarized DFT calculations were carried out using the Vienna *ab initio* Simulation Package (VASP). [103, 104] The projector augmented wave (PAW) [97] pseudopotentials were employed for electron-ion interactions. The generalized gradient approximation (GGA) parametrized by Perdew-Burke-Ernzerhof (PBE) [98] was used in combination with appropriate on-site Coulomb interactions (GGA+U) to describe the electron exchange and correlation potentials. Respective U values for Ti 3d and La 4f orbitals were set to 5.8 eV and 7.5 eV, as it is well established that such values are appropriate to describe these strongly-correlated states. [84, 169, 205, 211, 212] A 450 eV cut-off energy for the plane wave basis set was used, and a $10 \times 10 \times 1$ Γ-centered k-point mesh was found to be well-converged for self-consistent calculations. The convergence threshold for self-consistent-field iteration was set to 10^{-5} eV. The density of states (DOS) were calculated using the tetrahedron method with Blöchl corrections. [99] Atomic positions were relaxed along the c-direction until all components of the residual forces were smaller than 0.02 eV/Å. In the calculations of Born effective charges for bulk LAO and STO, identical parameters were used, with the exception of a $8 \times 8 \times 8$ Γ-centered k-point mesh instead of the $10 \times 10 \times 1$ Γ-centered k-point mesh used in HS calculations.

A supercell approach was used to model the LAO/STO HS slab system by depositing an LAO film on an STO substrate of eight unit cell thickness. A vacuum layer of approximately 14 Å along the [001] direction was added to resemble the actual epitaxial growth process of the HS system. Hence, one n-type interface and two distinct polar discontinuities are present in this study. The first polar discontinuity occurs at the LAO/STO interface, the other at the LAO surface/vacuum interface, see Figure 1S in the Supporting Information. The experimental lattice constant of STO, 3.905 Å, was fixed in the ab-plane to construct the unstrained HS system. The

lattice parameter along the [100] axis was adjusted to simulate various applied uniaxial strains from -1% to 1%. Interfacial charge carrier densities were calculated by integrating the occupation number of the interfacial Ti 3*d* orbitals from the conduction band minimum to the Fermi level, and then dividing by the interfacial area. This is because the interfacial conducting states are mainly contributed by the Ti 3*d* orbital at the interfacial TiO_2 layer. [160]

4.3 Results and Discussion

4.3.1 Unstrained Systems

Polarization Strength and Critical Thickness

We first explored the origin of the required critical thickness to form 2DEG in the unstrained LAO/STO HS system from the viewpoint of the polarization in the LAO film; specifically, the polarization strength versus the LAO film thickness. To do this, we modeled LAO/STO HS slab systems by depositing LAO films of various thickness on the TiO_2-terminated STO substrate along the [001] direction. Hereafter, these interface systems are referred to as $(LAO)_n$/STO, in which n (n = 1-6) denotes the number of LAO unit cells. The analysis of these relaxed HS indicates that the La/Al cations in the LAO film move towards the vacuum [207], producing relative displacements between the cations and anions (oxygen atoms) and a resulting polarization towards the vacuum. This polarization produces an internal electric field in the LAO film, which inhibits the polar-discontinuity-driven charge transfer from LAO to STO. As a result, one may speculate that the interfacial polar discontinuity in the LAO/STO system can be partially or entirely counteracted by the polarization in the LAO film, and the degree of the counteraction depends on the polarization strength.

To quantify the relationship between the polarization strength and the LAO film thickness, we calculated the average polarization P of the LAO unit cells in LAO/STO HS slab systems

using the following formula: [213, 214]

$$P = \frac{e}{\Omega} \sum_{i=1}^{N} Z_i^* \delta z_i \tag{4.1}$$

where Ω is the total volume of the LAO film, N is the number of atoms in the unit cell, Z_i^* is the Born effective charge for each atom, and δz_i is the relative displacement of the ith atom in the HS. The relative displacement (δz) of La(Al) cations with respect to the oxygen ions within the same LaO and AlO_2 planes is calculated as $\delta z_{La/Al} = z_{La/Al} - z_O$. Our calculated Born effective charges Z_i^* are 4.45, 2.92, -2.48, and -2.44 for La, Al, O in the LaO, and O in the AlO_2 layers for the tetragonal bulk LAO, respectively.

The estimated average polarization P_{LAO} of the LAO layers in the LAO/STO HS systems is plotted with respect to the number of LAO unit cells in Figure 4.1a. As an additional comparison, the band gap with respect to LAO film thickness is shown in Figure 4.1b, in which the band gap is defined as the energy gap between the O 2p states in the valence band and the Ti 3d states near the conduction band bottom and calculated from the DOS. The DOS of the $(LAO)_n$/STO (n = 1-6) HS slab systems are provided in Figure 2S of the Supporting Information. One can clearly see from Figures 4.1a and 4.1b that that as the LAO film thickness is increased from 1 to 6 unit cells, the polarization strength in the LAO film decreases, and the band gap also decreases. This implies that the barrier to charge transfer from the LAO film to the STO substrate weakens as the LAO film thickness increases. In other words, as the LAO film thickness increases, the tendency for electron transfer from the LAO film to the STO substrate increases, which leads to the insulator-to-metal transition in the LAO/STO HS system.

At the critical thickness (*i.e.*, 5 unit cells) the polarization in the LAO film becomes sufficiently diminished to permit charge transfer from the interfacial $(LaO)^{+1}$ to $(TiO_2)^0$ layer, leading to a zero band gap and the formation of the 2DEG. The determination of the critical thickness, 5 unit cells of LAO, is consistent with prior theoretical studies. [191, 207, 215] Con-

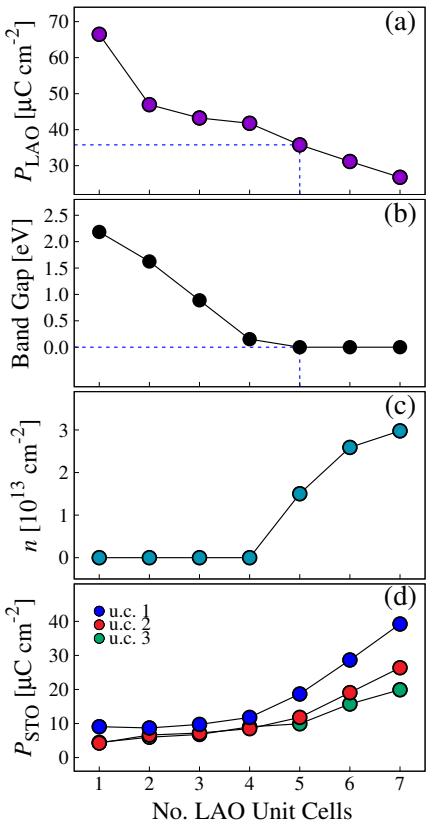

Figure 4.1: Calculated (a) average polarization (P) in LAO film, (b) band gap values, (c) interfacial charge carrier density (n), and (d) polarization in the first (blue), second (red), and third (green) STO unit cells (u.c.) with respect to the LAO film thickness in unstrained $(LAO)_n$/STO (n = 1-6) HS slab systems. The dashed blue lines indicate the polarization strength in the LAO film and band gap value at the critical thickness of LAO unit cell.

sequently, we can infer that the critical LAO polarization, above which 2DEG formation is strongly hindered, is $\approx$ 38-40 μC cm^{-2}. This value is quite consistent with that in prior theoretical work. [203] Below 5 unit cells, the polarization of the LAO film is strong enough to counteract the polar-discontinuity-induced charge transfer from the LAO film to STO substrate, and thus the LAO/STO HS system exhibits insulating behavior. At and above 5 unit cells, the polarization is weakened such that it can only partially counteract the polar-catastrophe-induced charge transfer, and the remaining electrons (much less than 0.5e) are transferred to the STO substrate, forming the 2DEG at the interface.

It is noted that, unlike in experimental studies, the DFT-calculated interfacial charge

carrier density tends to increase with the number of LAO unit cells after the LAO critical thickness has been reached. [216] Our present calculations show the same trend, as do those in our prior work. [205, 207] As demonstrated in Figure 4.1c, below 5 unit cells the strong LAO film polarization prevents any polar-discontinuity-driven charge transfer, leading to zero interfacial charge carrier density. Above 5 unit cells, interfacial charge carrier density increases as the LAO film thickness increases. It is interesting to note, however, that the calculated interfacial charge carrier density for the unstrained $(LAO)_5$/STO system is about 1.6×10^{13} cm^{-2}, which is in excellent agreement with the experimental value in the range of $1-2 \times 10^{13}$ cm^{-2}. [54, 143, 149, 196–198] In contrast, the superlattice model produces an interfacial charge carrier density about five to ten times greater than this value, [201, 205] indicating that the slab model is more appropriate in describing the interfacial electronic states than the superlattice model. This is mainly attributed to the fact that the slab model can appropriately reproduce the polarization behavior in the LAO film while the superlattice model cannot.

We also examined the polarization strength in the first three STO unit cells near the interface as a comparison with the LAO film, in which the vast majority of transferred charge is confined. After structural relaxation, the STO substrate exhibits polarization in the opposite direction from that in the LAO film, though its magnitude is much smaller. The calculated Born effective charges using the bulk cubic STO, Z_i^*, are 2.56, 7.42, -5.89, and -2.03 for Sr, Ti, O in the SrO, and O in the TiO_2 layers, respectively, which were used in the polarization calculation. Figure 4.1c shows the polarization in the first three STO unit cells nearest the interface with respect to LAO film thickness, demonstrating several facts. First, the polarization in all three STO cells tends to increase with the LAO film thickness. At the critical thickness of 5 LAO unit cells, there is a significant degree of polarization in the first STO unit cell (≈ 20 [μC cm^{-2}]). It is worth mentioning that the great majority of this polarization is contributed by the relative displacement between Sr and O ions in the SrO layers of the STO substrate, while that between the Ti and O ions in the TiO_2 layers have negligible contributions. This is consistent with prior work in which

Ti and O ions were found to have only slight polar distortion. [191]

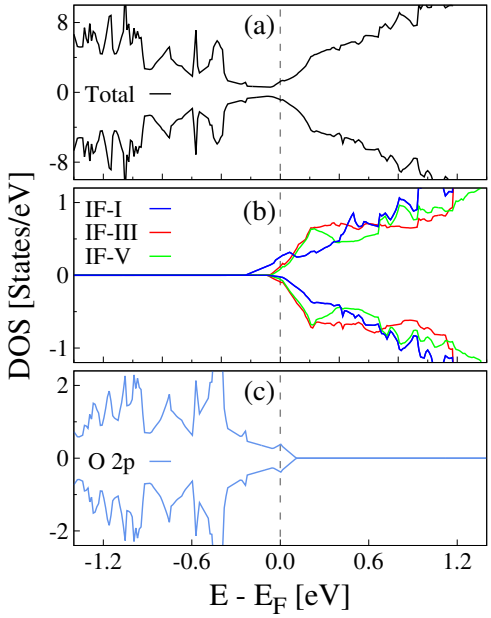

Figure 4.2: Calculated spin-polarized total (a), partial DOS projected on the Ti 3*d* orbitals from first three successive TiO_2 layers near interfacial region (b), and partial DOS projected on the O 2*p* orbitals from the surface $(AlO_2)^{-1}$ layer (c) in the unstrained $(LAO)_5$/STO HS slab system. IF-I, IF-III, and IF-V represent the first, third, and fifth TiO_2 layers of the STO substrate, respectively. The vertical dashed line indicates the Fermi level at 0 eV.

Electronic Properties

Next we considered the unstrained $(LAO)_5$/STO HS slab system to provide a frame of reference for the strained systems. The calculated spin-polarized total DOS, projected DOS for Ti 3*d* orbitals from the first three (*i.e.,* IF-I/III/V) interfacial TiO_2 layers in the STO substrate (b), and projected DOS for O 2*p* orbitals from the surface $(AlO_2)^{-1}$ layer is depicted in Figure 4.2. The total DOS (Figure 4.2a) clearly shows that the system exhibits conductivity, indicating that 5 unit cells of LAO film is sufficient to produce a 2DEG in the STO substrate. This result is consistent with previous GGA+*U* and hybrid functional calculations. [191, 207, 215]. Three consecutive $(TiO_2)^0$ layers, extending from the interface into the STO substrate, were defined as IF-I, IF-III, and IF-V. Figure 4.2b demonstrates that the Ti 3*d* orbitals at the IF-I $(TiO_2)^0$ layer

have the majority contribution to the interfacial conductivity, while the contribution from IF-III and IF-V layers is substantially less. Nevertheless, this small contribution from the IF-III and IF-V $(TiO_2)^0$ layers indicates that the 2DEG in the unstrained LAO/STO HS slab system extends three unit cells into the STO substrate, having a *c*-direction width of approximately 10 Å. All deeper $(TiO_2)^0$ layers show an insulating character, which confirms the formation of a 2DEG.

Moreover, O 2*p* surface states (Figure 4.2c) from the $(AlO_2)^{-1}$ surface layer also have a significant contribution to the conductivity and the hole states occur at the surface $(AlO_2)^{-1}$ layer, which can be compensated by oxygen vacancies [193] or passivated with H atoms [217]. In this case, the only metallic states would be present at the *n*-type interface. Finally, the calculated orbital-resolved DOS (Figure 3S – Supporting Information) of the unstrained system shows that Ti $3d_{xy}$ and O $2p_x/p_y$ orbitals from interfacial $(TiO_2)^0$ and surface $(AlO_2)^{-1}$ layers are mainly responsible for the interfacial and surface conductivity, respectively. These results are also consistent with prior theoretical and experimental work. [189, 207, 218]

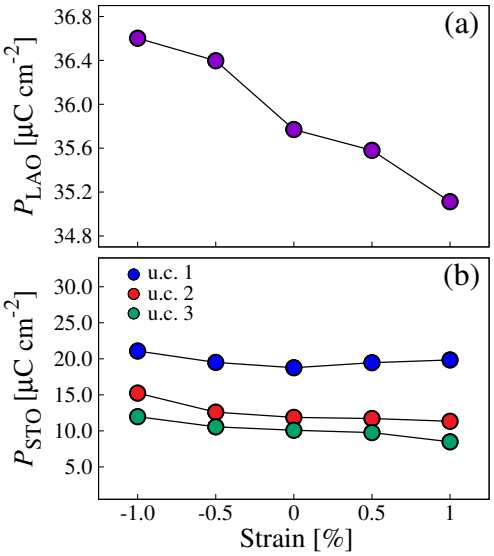

Figure 4.3: Calculated average polarization (P_{LAO}) in the LAO film (a), and in the first (blue), second (red), and third (green) STO unit cells (b) with respect to [100] uniaxial strain from -1% to $+1\%$ on the STO substrate in $(LAO)_5$/STO HS slab systems.

4.3.2 [100] Uniaxially Strained Systems

Polarization Strength and Critical Thickness

Herein, we examined the effect of uniaxial strain on the polarization strength in the LAO film and the STO substrate. To do this, the experimental lattice parameter a of the STO substrate, 3.905 Å, was used as reference point and then varied in a range from -1% to $+1\%$ to simulate applied uniaxial [100] strain. Negative values indicate compressive strain, while positive values signal tensile strain. The average polarization in the LAO film (P_{LAO}) is depicted in Figure 4.3a with respect to uniaxial [100] strain. It can be clearly seen that P_{LAO} decreases under tensile strain and increases under compressive strain. Thus, the interfacial polarization discontinuity is weakened by uniaxial tensile strain, weakening the driving force opposing charge transfer from LAO to STO. Uniaxial compressive strain, by contrast, strengthens P_{LAO} and discourages charge transfer from LAO to STO relative to the unstrained system. We also plotted the polarization in the first (blue), second (red), and third (green) unit cells of STO substrate with respect to uniaxial strain in Figure 4.3b. While no clear trend can be established for the polarization in the first STO unit cell, the polarization in the second and third cells appears to decrease with tensile strain and increase with compressive strain. However, overall polarization in the STO substrate is minor compared to the LAO film. Even in the STO unit cell nearest the interface, the polarization value is far less than P_{LAO}.

Given that [100] uniaxial strain affects P_{LAO}, one may consider whether the critical LAO film thickness (d_{crit}) to form 2DEG is affected as well. In fact, biaxial strains have been shown to significantly affect d_{crit} in experimental [190] and theoretical [207] studies. To investigate the situation in the uniaxial strain case, we calculated the total DOS for each of our strained systems (-1%, -0.5%, $+0.5\%$, and $+1\%$). The total DOS for -1% and $+1\%$ [100] uniaxially strained LAO/STO HS slab systems is shown in Figures 4.4a and 4.4b, clearly demonstrating that uniaxial strain in this range has no effect on d_{crit}. This result can be easily understood in the

context of the earlier polarization discussion: none of the applied strains increase P_{LAO} beyond the critical threshold ($\approx$40 [μC cm^{-2}], and thus 5 unit cells are sufficient to achieve n-type interfacial conductivity in each system.

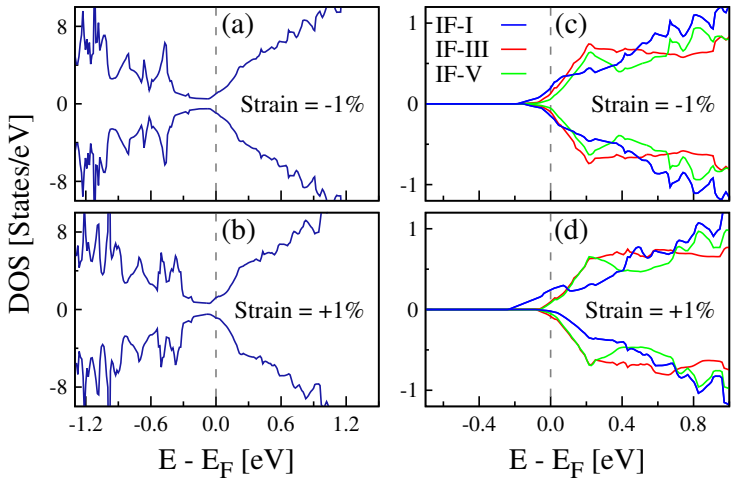

Figure 4.4: Calculated spin-polarized total DOS for n-type $(LAO)_5$/STO HS slab systems under -1% (a) and +1% (b) [100] uniaxial strain. Calculated partial DOS of Ti 3d orbitals from IF-I, IF-III, and IF-V TiO_2 layers in the STO substrate of the same systems under -1% (c) and +1% (d) [100] uniaxial strain.

Electronic Properties

Here we studied the effects of uniaxial strain on the 2DEG electron transport properties of the LAO/STO HS slab system. As mentioned previously, the free electrons transferred from LAO—which comprise the interfacial 2DEG—reside primarily in Ti 3d orbitals of the first (IF-I), third (IF-III), and fifth (IF-V) TiO_2 layers of the STO substrate. Thus, Figures 4.4c and 4.4d depict the calculated PDOS of Ti 3d orbitals at IF-I, IF-III, and IF-V TiO_2 layers for -1% and $+1\%$ uniaxially strained systems. Our results indicate that in the compressively strained system (Figure 4.4c), the contribution to the 2DEG from all the three TiO_2 layers is comparable. In other word, the 2DEG in the compressively strained system is almost equally dispersed between IF-I/III/V TiO_2 layers. In the tensile strained system (Figure 4.4d), by contrast, IF-I Ti 3d orbitals have a dominant contribution to the 2DEG. This indicates a 2DEG with a greater interfacial charge

carrier density, and a greater degree of concentration at IF-I, relative to that in the compressively strained system.

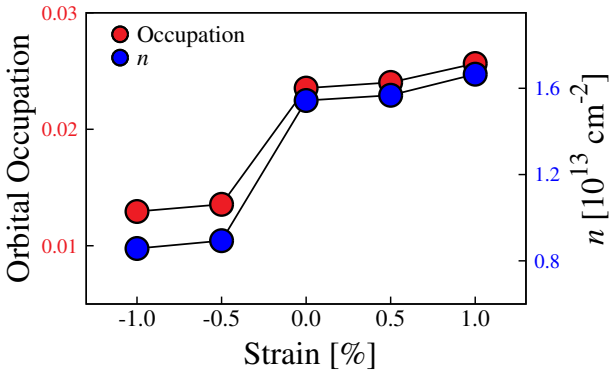

Figure 4.5: Calculated orbital occupation numbers and respective charge carrier densities (n) of Ti 3d orbitals at the interfacial TiO_2 layer in the STO substrate with respect to [100] uniaxial strain in the $(LAO)_5$/STO HS slab systems.

To provide a quantitative comparison between the unstrained and strained systems, we calculated the partial occupation number and charge carrier density of the interfacial (IF-I) Ti 3d orbitals in each case by integrating the partial DOS near the Fermi level. The calculated IF-I Ti 3d partial occupation numbers and respective charge carrier densities n for the unstrained and [100] uniaxially strained systems are shown in Figure 4.5. Our results indicate that the charge carrier density increases as strain is adjusted from -1% to $+1\%$. This increase is due to two factors. First, the LAO film polarization is consistently reduced by increasing tensile strain (see Figure 4.3a), weakening the driving force opposing charge transfer from LAO to STO, and ultimately promoting more charge transfer to STO. Second, strain changes the distribution of charge among the first three TiO_2 layers near the interface, resulting in a superior concentration of charge at the IF-I TiO_2 layer in the tensile strained system relative to that in the compressively strained system (see Figure 4.4c, 4.4d, and Figure 4S). It is particularly worth mentioning that the calculated interfacial charge carrier density for the unstrained $(LAO)_5$/STO system is about 1.6×10^{13} cm^{-2}, which is in excellent agreement with the experimental value in the range of $1-2 \times 10^{13}$ cm^{-2}. [54, 143, 149, 196–198] In contrast, the superlattice model produces an interfacial charge

carrier density about five to ten times greater than this value, [201, 205] indicating that the slab model is more appropriate in describing the interfacial electronic states than the superlattice model. This is mainly attributed to the fact that the slab model can appropriately reproduce the polarization behavior in the LAO film while the superlattice model cannot.

Here, we would like to mention that our earlier work on the [100] uniaxially strained periodic (*i.e.* without vacuum) LAO/STO superlattice system showed that compressive strains substantially increased the interfacial electron carrier density relative to the unstrained and tensile strained systems. [206]. The enhanced charge carrier density in the compressive strained systems was attributed to interfacial Ti $3d_{yz}$ orbitals instead of d_{xy}. In LAO/STO HS-based vacuum slab models, however, 2DEG originates only from Ti $3d_{xy}$ orbitals for all the strained systems and charge carrier density decreases for compressively strained systems, which is in excellent agreement with experiment. [192] The orbital-resolved Ti $3d$ DOS from the IF-I TiO_2 layers for -1% (a), 0% (b), and $+1\%$ (c) uniaxially strained LAO/STO HS slab systems are plotted in Figure 3S of the Supporting Information. One can clearly see that in each case, only d_{xy} orbitals cross the Fermi level, and are thus singularly responsible for the formation of 2DEG. The d_{yz} and d_{xz} orbitals remain unoccupied and stay at higher energies in the conduction band. Figure 3S also indicates that the partial occupation number of IF-I Ti $3d_{xy}$ orbitals increases when strain is applied on the STO substrate from -1% to $+1\%$, resulting in enhanced carrier density. In each case, O $2p_x/p_y$ states give rise to the surface conductivity. We also plotted the charge density projected on the bands forming the metallic states in -1%, 0%, and $+1\%$ uniaxially strained systems (see Figure 4S – Supporting Information), which supports the conclusion that IF-I charge carrier density is enhanced by tensile strain and diminished by compressive strain.

The effect of strain on orbital occupation number can also be analysed from the band structure. Figure 4.6 shows the band structure near the Γ point for -1%, 0%, and +1% strained systems, with the red band indicating the IF-I Ti 3d band. It can be clearly seen that compressive strain reduces the partial occupation of Ti $3d$ orbitals, while tensile strain increases it. The

band structure of these strained systems thus corroborates our DOS analysis of Figures 4.4c and 4.4d. Some hole states can also be easily discerned at the M point. These hole states are due to the dangling bonds at the surface layers, which can be typically compensated by oxygen vacancies [193] or passivated with H atoms. [217]

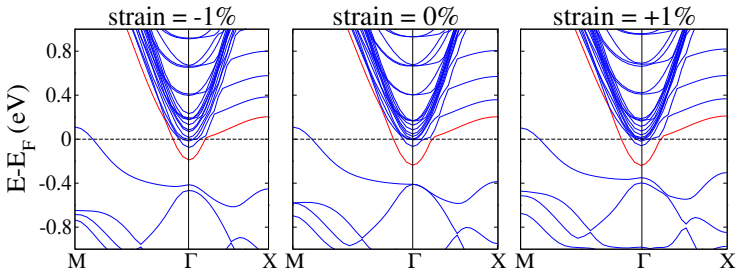

Figure 4.6: Calculated band structure for -1%, 0%, and $+1\%$ uniaxially strained $(LAO)_5$/STO HS slab systems. The red lines indicate the Ti $3d$ bands in the interfacial layer.

The conductivity of the LAO/STO HS system is not only determined by the interfacial charge carrier density but also by the electron mobility, a quantity closely related to the electron effective mass. Hence, to evaluate the influence of the uniaxial strain on the mobility, we calculated the effective mass (m^*/m_e) of free electrons at IF-I Ti $3d$ bands (colored red in Figure 4.6), which are mainly responsible for 2DEG in the strained and unstrained LAO/STO HS slab systems. We then normalized these effective masses to that of the unstrained system (m_o/m_e), yielding a series of normalized values m^*/m_o. Electron mobility can be related to m^* using the following equation: $\mu = \frac{e<\tau>}{m^*}$, [219] where e is the fundamental charge, $<\tau>$ is the average scattering time. Using the fact that electron mobility (μ) is inversely proportional to electron effective mass, along with the assumption that $<\tau>$ is a constant in these systems, we also generated a series of normalized mobility values μ/μ_o for the strained systems. The normalized electron effective masses and corresponding electron mobilities of all the systems are plotted in Figure 4.7a. It can be clearly seen that tensile strains reduce the electron effective mass and increase electron mobility. This comes in addition to the improvement in charge carrier density discussed earlier. Compressive strains, by contrast, raise effective mass and suppress electron

mobility, in addition to its negative effect on charge carrier density. However, it is noted that the effect of strain on charge carrier density is more pronounced than on electron mobility.

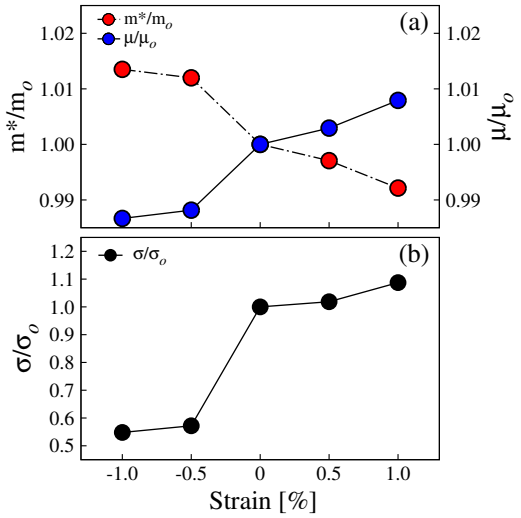

Figure 4.7: (a) Calculated normalized electron effective masses (m^*/m_o) and corresponding mobilities (μ/μ_o), and (b) normalized electrical conductivities (σ/σ_o) for Ti 3*d* electrons in the interfacial TiO_2 layer with respect to [100] uniaxial strain in $(LAO)_5$/STO HS slab systems.

It can thus be concluded that tensile strains increase the interfacial charge carrier density (see Figure 4.5) and electron mobility (see Figure 4.7), while compressive strains have the opposite effect on both of these quantities. This trend is mostly attributed to the induced ferroelectric polarization in the LAO film with respect to applied uniaxial [100] strain. Given these facts, an examination of interfacial conductivity itself is also appropriate. Electron conductivity can be calculated as $\sigma = ne\mu$, where n is the charge carrier density, and μ the electron mobility. The calculated conductivity (σ), normalized by the conductivity of the unstrained system (σ_o), is plotted with respect to strain in Figure 4.7b. As demonstrated in Figure 4.7b, there is an $\approx 9\%$ increase in interfacial conductivity under $+1\%$ tensile strain. Compressive (-1%) strain causes a large drop in the interfacial conductivity, mostly due to the sharp reduction in interfacial charge carrier density (Figure 4.5). In short, our calculations show that when uniaxial [100] strain on the STO substrate is adjusted from -1% to $+1\%$, the interfacial electron carrier density and mobility are both increased, resulting in enhanced interfacial conductivity. These results are in excellent

agreement with Moler *et al*.'s experimental findings, [192] in which the local conductivity is significantly enhanced under uniaxial tensile strain. Our results provide a convincing explanation for such a phenomenon.

4.4 Conclusions

The polarization characters and electronic properties of unstrained and uniaxially [100] strained LAO/STO HS slab systems were examined using first-principles density functional theory calculations. We first systematically revealed the correlation among the LAO film thickness and polarization, and the interfacial sheet carrier density, which can well explain the discrepancy between experimental and theoretical values of the 2DEG carrier density. When the HS system undergoes a compressive uniaxial strain, we found that the polarization magnitude in the LAO film increases with respect to that of the unstrained system, which has a negative impact on the electron transport properties of the LAO/STO HS system. Tensile strain, however, was found to reduce the polarization strength in the LAO film, which weakens the driving force against the charge transfer from the LAO to the STO substrate, thus improving the interfacial 2DEG charge carrier density and mobility. This improvement results in an enhanced interfacial conductivity, which is in an excellent agreement with experimental findings. Hence, we propose that uniaxial tensile strain could be an effective route to improve the interfacial conductivity in the LAO/STO system.

4.5 Acknowledgements

Chapter 3, in full, is a reprint of the material "Polarization Effects on the Interfacial Conductivity in the $LaAlO_3/SrTiO_3$ Heterostructure: First-Principles Study" as it appears in Physical Chemistry Chemical Physics. Maziar Behtash, Safdar Nazir, Kesong Yang, 18, 6831,

(2016). The dissertation author was the primary investigator and author of this paper.

Chapter 5

Oxygen Vacancy Formation in the $SrTiO_3$ Σ5 [001] Twist Grain Boundary from First-Principles

In Chapters 3 and 4, we have discussed methods of enhancing the electronic properties of two-dimensional electron gas at the $LaAlO_3/SrTiO_3$ (LAO/STO) heterointerface. We now turn our attention to the substrate of this system, $SrTiO_3$ (STO), which is widely used as a varistor, thermistor, and dielectric, among many other applications. [220–222] Oxygen vacancies have been shown to have significant effects on the bulk properties of STO, [54, 223, 224] and their segregation to tilt grain boundaries (GB) of STO has been closely studied. [225, 226] However, the segregation tendency of oxygen vacancies to the STO twist GB is completely unknown. In this Chapter, we present a comprehensive study of interface termination and oxygen vacancy formation in a low-energy Σ5 [001] STO twist GB via first-principles calculations. We identified three possible GB terminations, assessed their relative favorability in the chemical potential range necessary to maintain bulk STO stability, and found that only the SrO/SrO (S/S) and SrO/TiO_2 (S/T) terminations can form in STO. In addition, we found that oxygen vacancies tend to segregate

adjacent to the GB layer in the S/S GB system, but precisely at the GB layer in the S/T GB system. We generated temperature- and pressure-dependent GB phase diagrams for oxygen vacancy formation in STO, indicating that oxygen vacancies can form in a wider range of temperatures and pressures in the S/T system than in the S/S system. This work opens up a new avenue in STO GB engineering, namely that the position of oxygen vacancies with respect to STO twist GBs can be controlled by the ratio of S/S to S/T GB terminations, and is expected to stimulate experimental study of the STO twist GB system.

5.1 Introduction

Strontium titanate ($SrTiO_3$) is a versatile, low-cost material whose favorable bulk properties enable wide usage as a varistor, [220] thermistor, [221] and dielectric. [222] $SrTiO_3$ also finds diverse applications as a substrate in perovskite heterostructures for forming two-dimensional-electron-gas, [138, 227–230] and as a photocatalyst. [231] While the properties of bulk $SrTiO_3$ are quite well understood, many grain boundary (GB) properties are less clear. For example, since the seminal paper by Chiang and Takagi in 1990, [232] space-charge theory in the $SrTiO_3$ tilt GB has been explored from many perspectives. [225, 233–235] Chiang *et al*. proposed that the observed positive GB core charge in $SrTiO_3$ tilt boundaries is due to the segregation of intrinsic donor defects (O vacancies and Ti interstitials) and holes to the GB core, with oxygen vacancies providing the dominant contribution. This theory is based on the assumption that oxygen vacancies in $SrTiO_3$ do not permanently trap free electrons, and thus carry a positive relative charge. It is worth noting that oxygen vacancies in some other materials such as $BaZrO_3$ can trap free electrons and achieve neutrality relative to the anion sublattice site ($V_O^{\times}$). [55] In $SrTiO_3$, later theoretical work confirmed that the lowest energy charge state for oxygen vacancies is indeed +2 under most conditions ($V_O^{\bullet\bullet}$). [236–238] Chiang *et al*. found that, unlike the GB core, the area surrounding the GB core was enriched with free electrons and intrinsic acceptor

defects (chiefly Sr vacancies), and depleted of intrinsic donor defects (chiefly O vacancies). The net effect is to create a negatively charged area, beginning roughly 0.5 nm from the GB plane, which is called the space charge region. They also found that, quite unlike intrinsic acceptor defects, some extrinsic acceptor defects such as Al'_{Ti} segregate to the GB core. Chiang *et al*.'s findings can be summarized as follows: (1) intrinsic donors and holes segregate to the GB core and are depleted in the space charge region; (2) intrinsic acceptors and free electrons are depleted in the GB core and enriched in the space charge region; and (3) some extrinsic acceptors with concentrations well below the dilute limit (*i.e*. trace impurities) segregate to the GB core and are depleted in the space charge region.

The work of Chiang *et al*. stimulated a great deal of experimental studies, with additional controversies arising. Klie *et al*. determined that oxygen vacancies segregate to the GB core of a nominally-undoped $SrTiO_3$ 58° [001] tilt grain boundary using scanning transmission electron microscopy and electron energy loss spectroscopy. [225] They also observed an *n*-type conducting layer along the GB core, indicating the presence of free electrons therein. Klie *et al*.'s results are difficult to reconcile with space charge theory. This is because, according to space charge theory, the free electrons donated by oxygen vacancies migrate away from the GB core and become concentrated in the space charge region. In contrast, a later study of Fe-doped $SrTiO_3$ low-angle [001] tilt GB by De Souza *et al*. revealed a positive GB core charge contributed by oxygen vacancy segregation, and a negative flanking space charge region, in agreement with Chiang *et al*. [235] De Souza *et al*. also found that Fe'_{Ti} was enriched in the space charge region and primarily responsible for the negative charge there. This conclusion, however, is not consistent with Chiang *et al*.'s finding that extrinsic acceptors including Fe'_{Ti} tended to segregate to the GB core. [232]

Acceptor-doped $SrTiO_3$ tilt grain boundaries have also been closely examined using numerical simulation. McIntyre calculated equilibrium grain boundary depletion layer widths and found that oxygen vacancies were likely to be trapped in the GB core and unable to diffuse into

the space charge region or the grain interior beyond. [239] McIntyre also determined that defect concentrations do not approach bulk levels until 12-16 nm from the GB plane. This considerable width prevents direct investigation of the $SrTiO_3$ space charge region via density functional theory (DFT) calculations. DeSouza proposed four possible models which describe mobile/immobile acceptor dopants and oxygen vacancies, and calculated defect distributions and space charge potentials for each case. [240] Using a combined experimental and numerical analysis, Klie *et al*. found that oxygen vacancies accumulate in both the GB core and space charge region of acceptor-doped $SrTiO_3$. [241] Surprisingly, Klie *et al*. also reported a negative GB core charge and metallic conductivity along grain boundaries. In a subsequent comment, Meyer & DeSouza argued that a double Schottky barrier model is more appropriate than the Thomas-Fermi screening model used by Klie *et al*., because a positive GB core charge and depletion of oxygen vacancies in the space charge yields greater agreement with experimental work. [242] Meyer & DeSouza also noted that a negative GB core charge cannot be reconciled with the fact that tilt GBs act as barriers for oxygen diffusion. [243, 244]

Indeed, while $SrTiO_3$ tilt GBs have been extensively studied from both the theoretical [245–249] and experimental realms, [250–254] key controversies regarding the segregation of defects and the implications for space charge remain. [225, 233–235, 255–257] The properties of twist grain boundaries are even less understood. Nomura *et al*. carried out only one published experimental study of the $SrTiO_3$ $\Sigma 5$ [001] twist boundary, employing both transmission electron microscopy and molecular dynamics modelling. [258] While this study focused on GB properties with respect to temperature, the authors did conclude that the boundary was atomically sharp with a coincident site lattice (CSL) structure. This is quite unlike the picture typically found in many tilt grain boundaries, where secondary or even amorphous phases may be present in the GB core. [259, 260]

The segregation of substitutional defects or ionic vacancies to GBs can have vast effects on the bulk physical and electronic properties of many materials, leading to embrittlement, [63–65]

strengthening, [66, 67] or differential inter- and intra-grain conductivity. [68, 69] Although the segregation tendencies of such defects have been intensively studied in the $SrTiO_3$ tilt GB, [70–73] very little is known about their likely concentrations and locations in the $SrTiO_3$ twist GB. Astala *et al*. investigated the segregation tendencies of Na substitution at Sr sites in the $SrTiO_3$ $\Sigma 5$ [001] twist boundary, and found a strong tendency for the acceptor defect to segregate to the boundary. [261] An earlier study by the same group found that Sr-O divacancy in the GB core caused a decrease in GB energy, due to a reduction in like-ion repulsion across the GB plane. [262] However, due to computational limitations, each grain in their model contained only three SrO layers, two of which are boundary layers and equivalent by mirror symmetry. Beyond these two studies, the literature is largely barren regarding the $SrTiO_3$ twist GB. In particular, the segregation tendency of oxygen vacancies to the $SrTiO_3$ [001] twist GB is completely unknown. Oxygen vacancies have been shown to have major effects on the properties of $SrTiO_3$, [54, 223, 224] and their segregation in the $SrTiO_3$ tilt GB are responsible for key GB properties. [225, 226] Therefore a comprehensive study of oxygen vacancies in the $SrTiO_3$ twist GB is essential.

In this work, by using first-principles DFT calculations, we studied the $SrTiO_3$ $\Sigma 5$ [001] twist GB and carried out a comprehensive analysis of oxygen vacancy formation in this system. This article is organized into three sections. First, we discuss the relative energetic stability of three types of GB structures within the thermodynamic constraints to maintain bulk $SrTiO_3$ stability. Second, we examine the segregation behavior of oxygen vacancies in the twist GB structure. Finally, we generate GB phase diagrams of oxygen vacancies with respect to the synthesis temperature and oxygen partial pressure.

5.2 Computational Details and Structural Models

DFT calculations were carried out using the Vienna *ab initio* Simulation Package (VASP). [104] The projector augmented wave (PAW) [97] pseudopotentials were employed for electron-ion

interactions. The generalized gradient approximation (GGA) parametrized by Perdew-Burke-Ernzerhof (PBE) [98] was used to describe the electron exchange-correlation potentials. A 400 eV cut-off energy for the plane wave basis set was used during structural relaxation, and a $2 \times 2 \times 1$ Γ-centered *k*-point mesh is well-converged for self-consistent calculations. Subsequent single-point total energy calculations were carried out using Gaussian method with a $4 \times 4 \times 1$ Γ-centered *k*-point mesh, with a 480 eV cut-off energy for the plane wave basis set. All the atomic positions were relaxed until all components of the residual forces were smaller than 0.02 eV/Å, and the convergence threshold for self-consistent-field iteration was set to 10^{-5} eV. It is noted that DFT studies of transition metal oxides often require U corrections to properly describe the strongly-correlated d-orbitals. [263–265] We have carried out a series of test calculations to determine whether including a U correction of 5.8 eV on Ti $3d$ orbitals [152] would impact our conclusions. We found that the trend of formation energy values is completely unchanged, in spite of slight changes in the absolute values, indicating that U corrections have little effect on studying the formation energy trend of oxygen vacancies in the $SrTiO_3$ twist grain boundary.

$SrTiO_3$ is a layered structure along the [001] direction composed of alternating SrO and TiO_2 layers. As such, the [001] GB plane of a twist GB structure may be terminated by either SrO or TiO_2 layers. In principle, there are three possible GB terminations in the $SrTiO_3$ Σ5 [001] twist GB: SrO/SrO (S/S), TiO_2/TiO_2 (T/T), and SrO/TiO_2 (S/T) (see Fig. 6.1). Each GB structure is composed of two grains, with one grain rotated with respect to the other along the [001] direction. In the case of the S/S and T/T models, the two grains in each of them are equivalent. For example, in the S/S model, each grain is symmetric and terminated by SrO layers, while in the T/T model each grain is symmetric and terminated by TiO_2 layers. In contrast, in the S/T model the two grains are not equivalent because one grain is terminated by SrO layer (named as α-grain) and the other is terminated by TiO_2 layer (named as β-grain). In this work, the S/S GB was modeled using a 320-atom supercell composed of 14 SrO layers and 12 TiO_2 layers (see Fig. 6.1a); the S/T GB was modeled using a 325-atom supercell composed of 13 SrO layers and 13

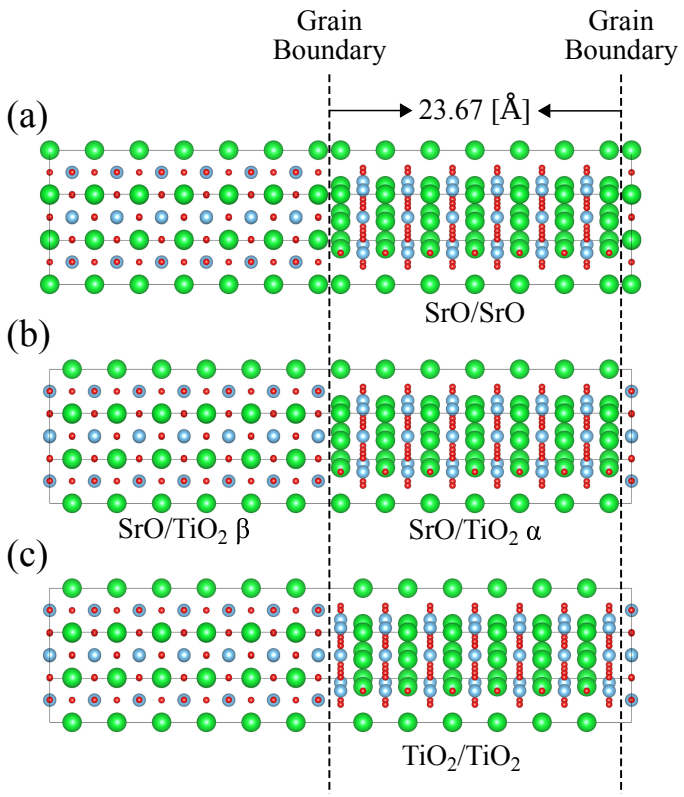

Figure 5.1: Structural depictions of three types of $SrTiO_3$ Σ5 [001] twist GBs: (a) SrO/SrO (S/S), (b) SrO/TiO_2 (S/T), and (c) TiO_2/TiO_2 (T/T). Vertical dashed lines indicate grain boundary positions. Two non-equivalent grains, labeled α and β, comprise the SrO/TiO_2 grain boundary system.

TiO_2 layers, achieving bulk $SrTiO_3$ stoichiometry (see Fig. 6.1b); and the T/T GB was modeled using a 330-atom supercell composed of 12 SrO layers and 14 TiO_2 layers (see see Fig. 6.1c).

5.3 Results and Discussion

5.3.1 Grain Boundary Energy and Relative Stability

Let us first study the relative stability of the S/S, S/T, and T/T GB structures, in particular which one is more likely to form within the chemical potential range necessary to guarantee bulk

$SrTiO_3$ stability. To do so, we calculated their GB energies (σ) using the following equation:

$$\sigma = (E_{GB} - nE_{STO} - m\mu_{Sr} - l\mu_O)/2A \tag{5.1}$$

in which E_{GB} and E_{STO} denote the total energy of the GB structure and the total energy of a single unit cell of $SrTiO_3$, respectively, and n represents the number of TiO_2 units in the structure. μ_{Sr} and μ_O are the chemical potentials of Ti and O, and m and l denote the number of stoichiometrically excessive Sr and O ions, respectively.

As shown from equation (1), σ is not fixed but depends on two variable chemical potentials, μ_{Sr} and μ_O. In fact, the favorability of many experimental syntheses can be controlled by tuning the chemical potentials of the relevant elements. In this case, the chemical potentials are linked by the stability of $SrTiO_3$:

$$\mu_{Sr} + \mu_{Ti} + 3\mu_O = E_{STO} \tag{5.2}$$

in which μ_{Sr}, μ_{Ti}, and μ_O represent the chemical potentials of Sr, Ti, and O, and E_{STO} refers to the total energy of an $SrTiO_3$ formula unit. Determining this chemical potential at specific thermodynamic conditions, however, often requires consideration of the other linked chemical potentials as well. For convenience, we define chemical potential references using following equations:

$$\Delta\mu_{Sr} = \mu_{Sr} - E_{Sr} \tag{5.3}$$

$$\Delta\mu_{Ti} = \mu_{Ti} - E_{Ti} \tag{5.4}$$

$$\Delta\mu_O = \mu_O - \frac{1}{2}E_{O_2} \tag{5.5}$$

in which E_{Sr} and E_{Ti} are the per-atom energy of the ground-state phases of elemental Sr and Ti, and E_{O_2} is the total energy of the ground state O_2 molecule. The formation enthalpy of $SrTiO_3$ is

defined as:

$$\Delta H_f(STO) = E_{STO} - E_{Sr} - E_{Ti} - \frac{3}{2}E_{O_2} \tag{5.6}$$

By using these definitions, equation (2) becomes:

$$\Delta H_f(STO) = \Delta\mu_{Sr} + \Delta\mu_{Ti} + 3\Delta\mu_O \tag{5.7}$$

Additionally the chemical potentials must be bounded to prevent the formation of competing phases. In the case of $SrTiO_3$ the most common competing phases are SrO and TiO_2, thus the following boundary conditions must also be satisfied:

$$\Delta\mu_{Sr} + \Delta\mu_O < \Delta H_f(SrO) \tag{5.8}$$

$$\Delta\mu_{Ti} + 2\Delta\mu_O < \Delta H_f(TiO_2) \tag{5.9}$$

in which $\Delta H_f(SrO)$ and $\Delta H_f(TiO_2)$ represent the respective formation enthalpies of bulk SrO and TiO_2. By using these boundary conditions, the stability phase diagram of $SrTiO_3$ with respect to $\Delta\mu_{Ti}$ and $\Delta\mu_O$ can be constructed (see Fig. 5.2). To determine stability regions for the three types of GB models, we employ several additional boundary conditions. By setting the GB energies of the S/S (σ_{GB}^{SS}) and S/T (σ_{GB}^{ST}) models equal, we are able to obtain the following equation:

$$E_{GB}^{SS} - E_{GB}^{ST} - 5E_{STO} + 10\mu_O + 20\mu_{Ti} = 0 \tag{5.10}$$

where E_{GB}^{SS} and E_{GB}^{ST} are the respective total energies of the S/S- and S/T-terminated GB structures. This boundary condition yields the boundary line between the S/S and S/T stability regions in the phase diagram. Moreover, the GB energy of both systems must also be greater than zero: [266]

$$\sigma_{GB}^{SS} = E_{GB}^{SS} - 60E_{STO} + 10\mu_O + 20\mu_{Ti} > 0 \tag{5.11}$$

$$\sigma_{GB}^{ST} = E_{GB}^{ST} - 65E_{STO} > 0 \tag{5.12}$$

Note that σ_{GB}^{ST} is independent of the Ti and O chemical potentials because the S/T system achieves bulk STO stoichiometry. Finally the boundary between the S/T and T/T stability regions can be determined by setting the GB energies of the S/T (σ_{GB}^{ST}) and T/T (σ_{GB}^{TT}) models equal, with the following equation:

$$E_{GB}^{TT} - E_{GB}^{ST} + 5E_{STO} - 10\mu_O - 20\mu_{Ti} = 0 \tag{5.13}$$

where E_{GB}^{TT} is the total energy of the T/T GB model. The boundary lines generated by equations (10, 11, and 13) are all parallel to those forming the bulk STO stability region. However, the boundary line described by equation (13) lies outside the bulk $SrTiO_3$ stability region, and within the TiO_2 precipitation region.

The relative stability of each GB termination is depicted in Fig. 5.2 overlaid on the bulk $SrTiO_3$ stability phase diagram. As shown in Fig. 5.2, the S/S boundary phase stability zone (turquoise) occupies most of the $SrTiO_3$ bulk stability region (black striped), and is favored in relatively Ti-poor and O-poor conditions. The S/T boundary phase stability zone (red) occupies a much smaller portion of the $SrTiO_3$ bulk stability region. This suggests that the S/S boundary model is thermodynamically favored over the S/T boundary model over a wider range of $\Delta\mu_O$ and $\Delta\mu_{Ti}$. Relative to the S/S GB, the S/T GB is favored in slightly more Ti-rich and O-rich conditions. Finally, the T/T boundary phase stability zone is not shown because it lies entirely outside the bulk $SrTiO_3$ stability region, indicating that the twist T/T GB model cannot be formed, as the required Ti-rich and O-rich conditions would cause precipitation of competing oxide TiO_2.

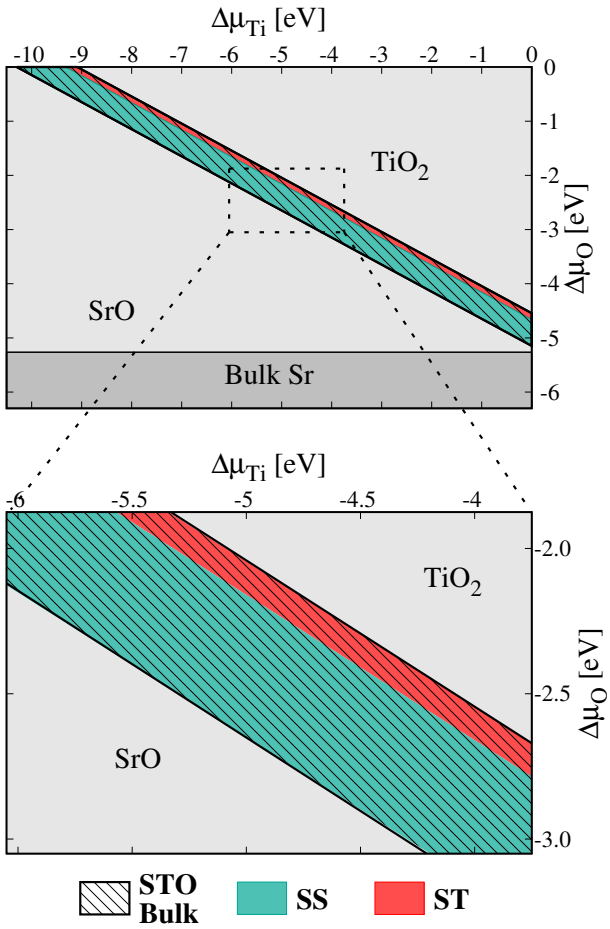

Figure 5.2: Grain boundary (GB) energy phase diagram with respect to $\Delta\mu_{Ti}$ and $\Delta\mu_O$ for the possible $SrTiO_3$ $\Sigma5$ [001] twist GB structures. The striped area indicates the region of bulk $SrTiO_3$ stability. The turquoise and red areas indicate the energetically favored regions for the S/S and S/T GB models, respectively.

5.3.2 Oxygen Vacancy Segregation

SrO/SrO Grain Boundary

To determine the preferred positions of oxygen vacancies in the $SrTiO_3$ $\Sigma5$ [001] twist GB, we produced a series of oxygen-deficient GB structures by systematically creating oxygen vacancies at each non-equivalent oxygen site. Each structure bears only a single oxygen vacancy, yielding a vacancy concentration of approximately 0.5 mol%. It is worth mentioning that in CSL twist grain boundaries some ions lie in coincidence across the GB plane, along lines normal to the

GB plane, and some do not. For example, in the case of the $SrTiO_3$ $\Sigma 5$ [001] twist GB, there are two to three non-equivalent oxygen sites in each layer: one coincidence site and either one or two non-coincidence sites, depending on layer type (SrO or TiO_2). In this work, all non-equivalent oxygen vacancy positions are considered. We begin by examining the S/S GB model that is composed of two equivalent grains.

To analyze the segregation of oxygen vacancies in the S/S GB, we calculated oxygen vacancy formation energies at all the non-equivalent oxygen sites in the S/S GB model, with and without structural relaxation. The purpose of these calculations is to determine the effects of structural relaxation on the formation of oxygen vacancies. Oxygen vacancy formation energies were calculated using the following equation:

$$E_f(V_O) = E_{vac} - E_{pris} + \mu_O \tag{5.14}$$

where E_{vac} and E_{pris} denote the total energy of the GB structures with and without oxygen vacancies, respectively. By using the typical experimental growth condition of $SrTiO_3$, *i.e.*, temperature of 750 °C and an oxygen partial pressure of 10^{-9} atm, [267–274] we obtained the $\Delta\mu_O = -2.04$ eV. The calculated formation energies of oxygen vacancy without and with structural relaxations are plotted in Fig. 5.3a and Fig. 5.3b, respectively, with respect to the vacancy positions. As a comparison, $E_f(V_O)$ in bulk $SrTiO_3$ is also shown in the plots. A comprehensive analysis leads to following conclusions:

(i) In the unrelaxed GB structure (Fig. 5.3a), the calculated $E_f(V_O)$ for all layers except the GB SrO layer is slightly larger than that in bulk $SrTiO_3$. This is because the intra-grain crystal structure of the unrelaxed GB model is mostly identical to that of bulk $SrTiO_3$. As for the GB SrO layer, $E_f(V_O)$ is lower than that in the grain interior by nearly 2 eV. The lower $E_f(V_O)$ is because the oxygen atom in the GB SrO layer is bound to only one Ti ion rather than two, unlike all other vacancy positions considered in the S/S GB system.

(ii) In the relaxed GB structure (Fig. 5.3b), the calculated $E_f(V_O)$ in grain interior layers is about 1.4 - 1.5 eV, which is lower than that in bulk $SrTiO_3$ by around 0.5 - 0.6 eV. This is different from the case in the unrelaxed GB structure, in which the $E_f(V_O)$ in the grain interior layers is slightly larger than that in the bulk. Additionally, $E_f(V_O)$ in the GB SrO layer is roughly 0.3 eV lower than in the grain interior, which is a much smaller difference than that in the unrelaxed case (0.3 versus 2.0 eV). This indicates that structural relaxation plays a significant role in determining $E_f(V_O)$. Moreover, the lowest $E_f(V_O)$ value is found in the GB TiO_2 layer rather than the GB SrO layer, unlike in the unrelaxed GB structure.

(iii) In both the unrelaxed and relaxed cases, the formation energy of oxygen vacancies in GB layers is lower than that in the grain interior layers. This indicates that oxygen vacancies tend to segregate to the GB. In particular, oxygen vacancies in the TiO_2 layer nearest to the GB have the lowest formation energy, and those in grain interior SrO and TiO_2 layers have the highest formation energy. Our calculations suggest an enrichment of oxygen vacancies directly adjacent to the GB core, and a depletion of oxygen vacancies in the grain interior.

SrO/TiO_2 Grain Boundary

Next we consider the oxygen vacancy formation energy in the S/T GB structure. Unlike the S/S GB structure, the two grains which comprise the S/T GB structure are not equivalent. One grain is terminated by SrO layers (defined as grain 'α'), while the other is terminated by TiO_2 layers (defined as grain 'β'). The twist GB plane is situated at the interface between the α and β grains. Therefore, $E_f(V_O)$ should be different in each of the two grains, and thus we investigate $E_f(V_O)$ separately for each grain.

First, we examine the effect of structural relaxation on $E_f(V_O)$. The calculated $E_f(V_O)$ in the unrelaxed α and β grains of the S/T-terminated GB system is shown in Fig. 5.4a and 5.4b, respectively. Strikingly, overall $E_f(V_O)$ in the α grain is notably lower than that in the β grain (3.3 versus 3.8 eV). Moreover, average $E_f(V_O)$ in the α grain is lower than that in bulk STO by

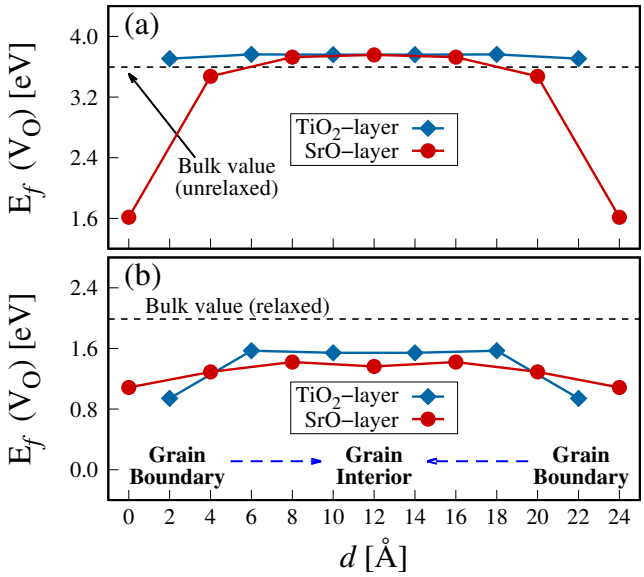

Figure 5.3: Calculated (a) unrelaxed and (b) relaxed oxygen vacancy defect formation energies in the S/S GB model with respect to distance from the left GB. All non-equivalent oxygen sublattice sites are considered, and the lowest formation energy within a given layer is plotted. The dashed black lines indicate the formation energy of an oxygen vacancy in bulk, cubic $SrTiO_3$ in (a) unrelaxed and (b) relaxed cases.

≈0.3 eV, while $E_f(V_O)$ in the β grain is higher than that in bulk STO by ≈0.2 eV. In both grains, $E_f(V_O)$ is lower at the GB than in the grain interior. However, in the α grain $E_f(V_O)$ shows a pronounced drop at the GB SrO layer (1.2 eV vs 3.3 eV in the grain interior), while there is no such sharp drop in the β grain. This finding is due to the same mechanism observed earlier in the unrelaxed S/S-terminated GB system (Fig. 5.3a): the GB SrO oxygen site in the α grain is bound to only one Ti ion rather than two.

In the relaxed α and β grains, $E_f(V_O)$ remains lowest at the GB and highest in the grain interior (see Fig. 5.4c,d). However, the magnitude of change in $E_f(V_O)$ is significantly different from that in the unrelaxed case. For example, $E_f(V_O)$ in the unrelaxed α grain is 2.1 eV lower at the GB than in the grain interior, yet this difference shrinks to 0.9 eV in the relaxed case. In the β grain, by contrast, $E_f(V_O)$ in the unrelaxed case is 0.4 eV lower at the GB than in the grain interior, yet this difference grows to 1.1 eV in the relaxed case. In other words, structural relaxation weakens the oxygen vacancy segregation tendency in the α grain yet strengthens it in

the β grain. However, average $E_f(V_O)$ in the relaxed α grain remains lower than that in the relaxed β grain, but not to the extent seen in the unrelaxed case. We note that in the relaxed α and β grains, $E_f(V_O)$ in the grain interior is lower than that in the bulk. This indicates that bulk-like properties are not fully reproduced in the grain interior. According to our test calculation, expanding the cell by ≈16 Å along [001] yields an $E_f(V_O)$ value in the grain interior which is ≈0.2 eV closer to the bulk value. We therefore expect that $E_f(V_O)$ in the grain interior will become closer to the bulk $E_f(V_O)$ value as the system is further expanded.

We now compare the oxygen vacancy segregation behavior in the S/S and S/T GB systems. For the S/T GB system, $E_f(V_O)$ is lowest at the interfacial GB layer and highest in the grain interior (see Fig. 5.4c and 5.4d). This finding is slightly different from that in the S/S GB system, where oxygen vacancies have the lowest formation energy in the TiO_2 layer adjacent to the interfacial GB layer (see Fig. 5.3b). In fact, this slight difference in $E_f(V_O)$ leads to a large difference in the oxygen vacancy formation probability profile between the S/S and S/T systems. In the S/T system, relative oxygen vacancy formation probability is by far the greatest at the interfacial GB layer in both the α and β grains, that is, respective SrO and TiO_2 layers (see Fig. S2 of the supporting information). In contrast, in the S/S system oxygen vacancies show the highest relative probability in the TiO_2 layer adjacent to the interfacial GB layer (see Fig. S1 of the supporting information). Therefore oxygen vacancies tend to segregate precisely to the GB in the S/T system, but adjacent to the GB in the S/S system. This opens up an interesting avenue in GB engineering: if the ratio of S/S to S/T GB can be controlled, the relative positions of oxygen vacancies in the material (and hence key properties including oxygen mobility and electronic conductivity across GBs) can be tuned.

As mentioned above, the formation energy of oxygen vacancies in the α grain of the S/T GB is lower than that in the β grain, particularly in the unrelaxed case. To investigate this discrepancy, we calculated the electrostatic potential energy along the *c*-direction for the entire pristine S/T GB structure, in both unrelaxed and relaxed cases (see Fig. 5.5). In the unrelaxed case

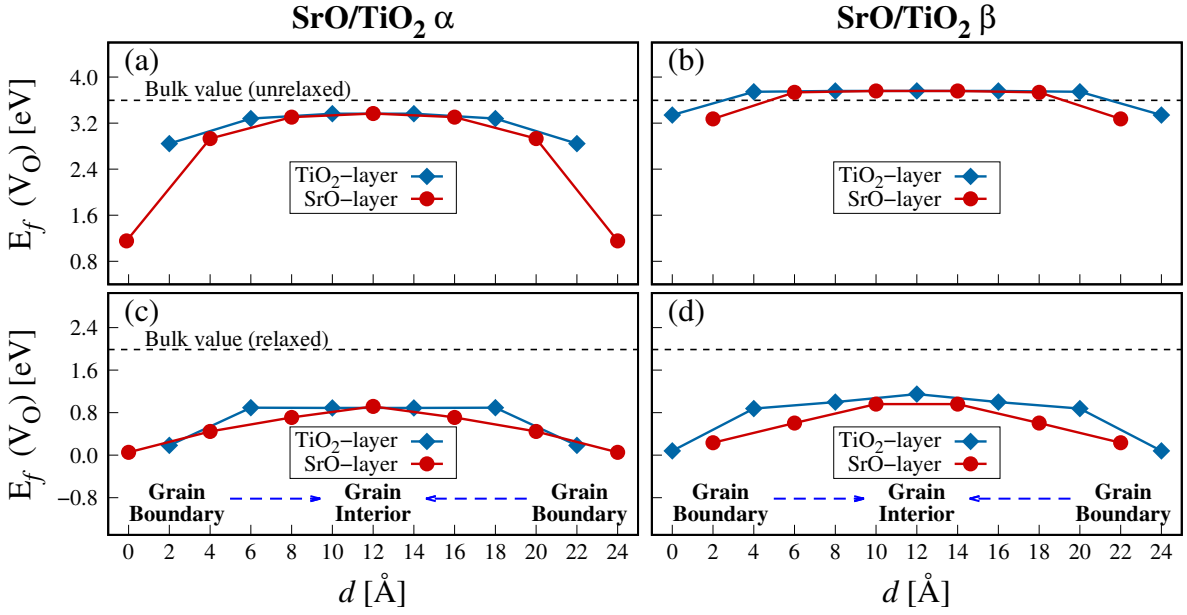

Figure 5.4: Calculated (a, b) unrelaxed and (c, d) relaxed oxygen vacancy defect formation energies in the S/T GB model with respect to distance from the left GB, in both the α and β grains. The dashed black lines indicate the formation energy of an oxygen vacancy in bulk, cubic $SrTiO_3$ in (a, b) unrelaxed and (c, d) relaxed cases.

(Fig. 5.5a), the macroscopic averaged electrostatic potential energy within the β grain is more negative than that in the α grain by approximately 1.3 eV (labeled as ΔE_u). This implies that the average ionic bond strength is higher in the β grain than in the α grain. [275, 276] In the relaxed case (Fig. 5.5b), the difference in electrostatic potential energy between α and β grains shrinks slightly to 1.1 eV (labeled as ΔE_r). Additionally there is a spike in the electrostatic potential energy at the GB in the relaxed case which is not present in the unrelaxed case. This spike is a consequence of structural changes near the GB plane after relaxation. In both unrelaxed and relaxed cases, however, the more negative electrostatic potential in the β grain signifies a greater ionic bond strength and thus leads to the higher $E_f(V_O)$.

Grain Boundary Phase Diagram

Finally, we generate GB phase diagrams for oxygen vacancy with respect to synthesis temperature (T) and oxygen partial pressure (p_{O_2}). $SrTiO_3$ can be synthesized under a wide

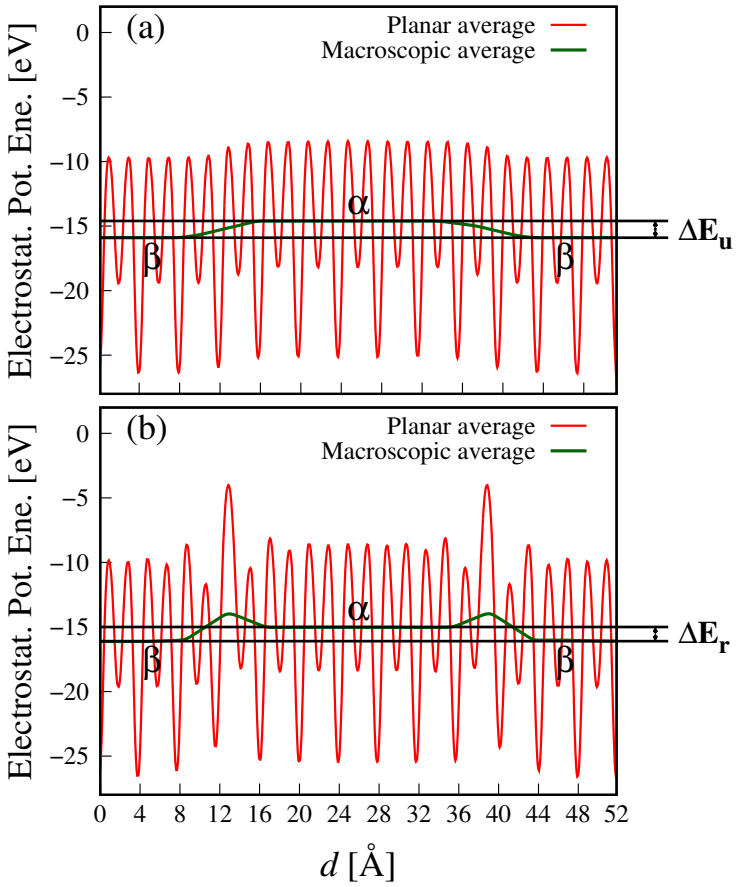

Figure 5.5: Calculated (a) unrelaxed and (b) relaxed electrostatic potential energy with respect to distance along the *c*-axis for the pristine S/T GB model. The α grain is in the center of the depiction, flanked by the two halves of the β grain. The black horizontal lines emphasize the difference ΔE between the macroscopically-averaged electrostatic potential energy in the α and β grains.

variety of experimental conditions, with most syntheses at temperatures between 600 and 1400 °C, and oxygen partial pressures between 10^{-12} atm and $10^{-0.7}$ atm. [267–274, 277] Therefore the GB phase diagrams are made to correspond to these T and p_{O_2} ranges. To do so, we included both the enthalpic and entropic contributions to the oxygen chemical potential. $\Delta\mu_O$ can thus be expressed with respect to T and p_{O_2} as follows:

$$\Delta\mu_O(T,P_0) = ([H_0 + \Delta H(T)] - T[S_0 + \Delta S(T)]) \tag{5.15}$$

$$\Delta\mu_O(T,P) = \Delta\mu_O(T,P_0) + \frac{1}{2}k_B T ln(\frac{P}{P_0}) \tag{5.16}$$

where the O_2 enthalpy $H_0 = 8.7$ kJ mol^{-1} and entropy $S_0 = 205$ J mol^{-1}K^{-1} at ambient conditions ($T_0 = 298$ K, $P_0 = 1$ atm), [278] $\Delta H(T) = C_P(T - T_0)$, and $\Delta S(T) = C_P \ln(T/T_0)$. Since all $SrTiO_3$ synthesis conditions considered are well within ranges where the ideal gas law can be justifiably applied ($T \geq 298$ K & $p_{O_2} \leq 1$ atm), the surrounding O_2 gas can be treated as an ideal reservoir. [279] Thus, we can approximate the isobaric heat capacity per diatomic molecule $C_P = 3.5k_B$. [280] Therefore for any given pressure P_0 we may determine a series of $\Delta\mu_O(P = P_0)$ values with respect to T, and vice-versa. Using this approach we generate oxygen vacancy phase diagrams with respect to T and p_{O_2} for the S/S and S/T GB systems (see Fig. 5.6). An $E_f(V_O)$ of zero is emphasized with a black line, while increasingly positive (red) and negative (blue) $E_f(V_O)$ are depicted with increasingly saturated coloring. For each GB phase diagram, we consider only oxygen vacancies with the lowest $E_f(V_O)$: adjacent to the interfacial GB layer for S/S (defined as the 'penultimate' layer), and at the interfacial GB layer for S/T. It is noted that the line indicating $E_f(V_O) = 0$ is nonlinear; this is due to variations in the temperature dependence of $E_f(V_O)$ with respect to pressure. In particular, a given change in T has a substantially greater effect on $E_f(V_O)$ at low p_{O_2} than at high p_{O_2}.

We now compare the oxygen vacancy phase diagrams for the S/S and S/T GB systems. In the S/S system, oxygen vacancy formation requires a minimum synthesis temperature of roughly 1000 °C in the penultimate layer (see the blue region of Fig. 5.6a). In the S/T system, by contrast, oxygen vacancies can form at roughly 660 °C in the interfacial GB layer, differing slightly depending on whether the α grain or β grain is considered (Fig. 5.6b/c). Similarly, at temperatures greater than 1000 °C, oxygen vacancies can form at higher p_{O_2} in the S/T GB (α or β) than in the S/S GB. In other words, oxygen vacancies are relatively easy to form at the S/T-terminated GB, but depend on high synthesis T and low p_{O_2} to form in the S/S-terminated GB. The reader may note that $E_f(V_O)$ is negative in the blue regions of the phase diagram; this does not imply phase

decomposition and significant O_2 release. This is because each phase diagram is generated for the lowest energy oxygen vacancy position: at the penultimate and interfacial layers for the S/S and S/T GB systems, respectively. In either case, oxygen vacancies would not form elsewhere in the lattice until more extreme experimental conditions were imposed. We note that the energy to form a second oxygen vacancy would not be the same as the $E_f(V_O)$ values calculated here (*i.e.* not additive). Next, we compare the phase diagrams for oxygen vacancy formation in the α and β grains of the S/T GB system (see Fig. 5.6b,c). We find that oxygen vacancies can form as low as 650 °C in the α grain (Fig. 5.6b), and 670 °C in the β grain (Fig. 5.6c). This finding is consistent with our earlier conclusion that oxygen vacancies form more easily in the α grain than the β grain, though this difference is much smaller than that between the S/S and S/T systems as a whole.

Finally, we compare our results with experimental work on the $SrTiO_3$ tilt grain boundary. By studying the formation energy of oxygen vacancies at different sites in the $SrTiO_3$ grain boundary, we find that oxygen vacancies tend to segregate to the GB core in the twist system. In fact, experimental studies have indicated that oxygen vacancies also segregate to the GB core in tilt boundaries of $SrTiO_3$. [225, 232] Many related studies confirm that these segregated oxygen vacancies are responsible for the observed positive GB core charge in $SrTiO_3$ tilt boundaries. [235, 281] Zhang *et al*. suggested that oxygen deficiency in the $SrTiO_3$ tilt GB core may also be responsible for repulsion of Ti cations, causing the observed shift of ions away from the GB plane. [282] However, we can now identify two key differences in oxygen vacancy formation between $SrTiO_3$ tilt and twist GBs. First, the lowest-energy position of oxygen vacancies in the twist GB is dependent upon the GB termination, because of its layered structural features. In the S/S system, oxygen vacancies have the lowest formation energy in the penultimate layer, while in the S/T system they have the lowest formation energy in the interfacial layer itself. No such mechanism has been observed in the tilt boundary. Second, prior experimental work on the $SrTiO_3$ tilt GB has indicated that, although the enthalpic term is dominant, [239, 240] oxygen vacancy segregation is entropically favorable and thus increases with temperature. [225, 283] Our

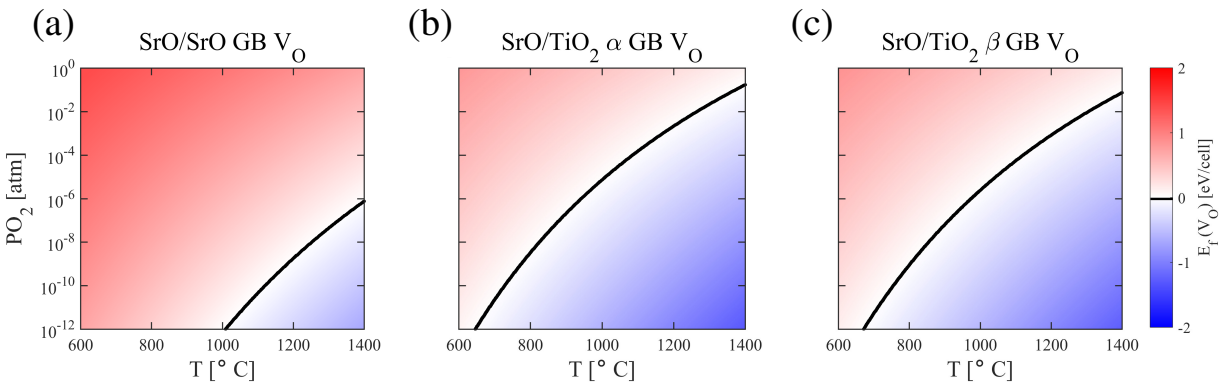

Figure 5.6: Oxygen vacancy formation energy in the (a) S/S, (b) S/T α, and (c) S/T β twist GBs with respect to synthesis temperature and oxygen partial pressure. A formation energy of zero is emphasized with a solid black line. Increasingly positive (red) or negative (blue) formation energies are depicted with increasingly saturated coloring. The formation energies calculated are for a single oxygen vacancy and are not additive.

calculations indicate an opposite tendency in the $SrTiO_3$ twist GB system. Although the energetic favorability of oxygen vacancy formation throughout the system increases with temperature, the oyxgen vacancy segregation tendency decreases with temperature (see supporting information). In other words, increasing temperature can reduce oxygen vacancy formation energy in both the GB core and grain interior, but it also weakens the energetic advantage of oxygen vacancy formation in the GB core relative to that in the grain interior.

5.4 Conclusions

In summary, we have studied relative termination stability and oxygen vacancy segregation behavior in the $SrTiO_3$ Σ5 [001] twist GB using first-principles calculations. Our results show that the S/S and S/T GB structures can form within the chemical potential range necessary to maintain $SrTiO_3$ stability, while the T/T GB structure cannot. The S/S GB structure is energetically favored over the S/T GB structure in the majority of the $SrTiO_3$ phase stability zone. Oxygen vacancy formation energies were also calculated for the S/S and S/T systems, to determine segregation behavior in each case. We found that oxygen vacancies in the S/S system segregate to the TiO_2

layer adjacent to the interfacial GB layer, while those in the S/T system tend to segregate to the interfacial GB layer (SrO for α and TiO_2 for β). This implies that the relative positions of oxygen vacancies in the material may be tuned via control of the S/S to S/T termination ratio, providing more opportunities for GB engineering. Moreover, oxygen vacancy formation energies were found to be higher in the β grain than in the α grain, which can be explained by a more negative average electrostatic potential energy in the β grain. Finally, grain boundary phase diagrams for oxygen vacancy with respect to synthesis temperature and oxygen partial pressure were generated. The phase diagrams show that oxygen vacancies can form in a wider range of temperatures and pressures in the S/T system than in the S/S system, indicating that the concentration of oxygen vacancies in each system is different even at the same experimental condition. These findings provide useful guidance regarding the experimental conditions necessary to promote oxygen vacancy formation in the $SrTiO_3$ twist GB system.

5.5 Acknowledgements

Chapter 5, in full, is a reprint of the material "Oxygen Vacancy Formation in the $SrTiO_3$ Σ5 [001] Twist Grain Boundary from First-Principles" as it appears in Journal of the American Ceramic Society. Maziar Behtash, Yaqin Wang, Jian Luo, Kesong Yang, 101, 3118, (2018). The dissertation author was the primary investigator and author of this paper.

Chapter 6

First-Principles Study of Impurity Segregation in Zirconia, Hafnia, and Yttria-Stabilized-Zirconia Grain Boundaries

In Chapter 5 we explored oxygen vacancy segregation in twist grain boundaries of $SrTiO_3$. We now turn our attention to grain boundaries in yttria-stabilized zirconia (YSZ), a refractory oxide with excellent chemical inertness and high-temperature stability. [284–286] Among the most important applications of YSZ is its use as a thermal barrier coating (TBC), which has enabled substantial increases in the operating temperature of gas turbine engines used in powered flight. However, YSZ-based TBCs are vulnerable to hot-corrosion by ingested impurities, resulting in TBC degradation and the exposure of the turbine blades, which in turn leads to premature failure of the engine. [287–289] Sand ingestion is particularly damaging, leading to the formation of calcium-magnesium-alumino silicate (CMAS) which easily infiltrates the TBC and begins attacking it. This attack occurs preferentially at grain boundaries (GB), and involves a process by

which certain impurities become segregated at GBs with primarily deleterious results. [290–292] In this Chapter we present a detailed theoretical study of impurity segregation in ZrO_2, HfO_2, and YSZ grain boundaries via first-principles calculations. We found that there is a fundamental difference in the segregation profiles of charged and uncharged impurities. In addition, we found that Si and Ca are strong segregants in YSZ while Al, Ti, and Y are not. This work is the first DFT study to successfully generate and structurally-optimize a YSZ grain boundary model containing appropriate concentrations of yttrium dopants and oxygen vacancies, and provides new insights regarding the impurities most involved in CMAS-attack of YSZ.

6.1 Introduction

Yttria-stabilized zirconia (YSZ) is widely used as a thermal barrier coating (TBC) in gas turbine engines because of its exceptional material properties such as low thermal conductivity, [293,294] chemical inertness, [284] phase stability at room and operational temperature, [285,286] and a close thermal expansion match with the typical nickel-base superalloy substrate. [295] In recent years, however, the YSZ-based TBC in gas turbine engines has been exposed to a new challenge in the form of dust and sand ingestion. It is believed that the sand enters the combustion chamber and attacks the integrity of the TBC through a combination of physical and chemical effects. [287] The mechanisms behind the chemical infiltration may involve impurity segregation to grain boundaries (GB) and the formation of siliceous phases, [296] impurity-silicates, [287] and oxide-silicon interfaces. [297] These combined effects degrade and ultimately destroy the capacity of the TBC to protect the turbine blades from the heat of the combustion chamber. [288] Closely involved in this process is the formation of Calcium–Magnesium–Alumino Silicate (CMAS), which rapidly infiltrates the TBC and attacks the platinum-modified nickel aluminide bond coat. [288, 298, 299] In addition, CMAS has also been found to partially dissolve YSZ upon contact, which is then reprecipitated in a yttria-depleted monoclinic phase. [289, 300]

The tetragonal to monoclinic phase transition is accompanied by a destructive 3-9% volume expansion which promotes spallation of the TBC. [301, 302] CMAS attack has been shown to occur preferentially at grain boundaries, [290–292] and is closely tied with impurity segregation, whereby impurities become concentrated at grain boundaries. [63–65]

Significant efforts have been made to study impurity segregation in zirconia grain boundaries. Matsuda *et al*. used secondary ion mass spectrometry (SIMS) to study Ca diffusion in polycrystalline 10 mol% cubic YSZ (*c*–10YSZ), and observed no segregation of Ca to GBs. [303] However, a subsequent SIMS analysis by Kowalski *et al*. in *c*–8YSZ found a strong segregation tendency, in which Ca was almost exclusively observed at GBs. [304] Guo *et al*. studied the segregation behavior of trace SiO_2 in Al_2O_3-doped *c*–9YSZ samples containing both amorphous and crystalline GBs using electron probe microanalysis (EPMA) and energy-dispersive X-ray spectroscopy (EDS). [305] Interestingly, despite the presence of trace SiO_2 in their reaction powders, the authors could detect Si only within amorphous GBs rather than crystalline GBs. In 15 mol% CaO-stabilized cubic zirconia, Aoki *et al*. found that the segregation behavior of Si impurities depends on the grain size, with nearly zero segregation in the samples with the smallest grain sizes of 0.14 μm. [306] These results are surprising in light of the fact that the bulk solubility of SiO_2 in stabilized zirconia, roughly 0.0025 mol%, [306] is exceedingly low compared to that of CaO ($\approx$19 mol%). [307] This is because, in principle, the segregation tendency is greater for the impurity with lower bulk solubility. [308–310] In short, these experimental results suggest that grain size and GB crystallinity have significant effects on the segregation tendencies of impurities, even those with low bulk solubility.

Despite substantial experimental study, a complete understanding of impurity segregation in YSZ remains elusive. This is primarily due to a lot of variations in experimental setup such as grain size, impurity concentration, and stabilizing oxides, which adds a certain level of complexity to the computational and theoretical studies. In fact, prior theoretical studies have generally been limited to studying the distribution of intrinsic defects in YSZ, such as yttrium

substitutions (Y_{Zr}) or oxygen vacancies (V_O). For example, Lee *et al*. reported that both Y_{Zr} and V_O show a modest segregation tendency to the Σ5 (310)/[001] GB of *c*–10YSZ using a hybrid Monte Carlo–Molecular Dynamics simulation. [311] A later experimental and theoretical work found that both Y_{Zr} and V_O segregate to the Σ13 (510)/[001] GB, but that V_O segregates more strongly. [312] Nevertheless, few theoretical studies particularly at the quantum mechanics level have examined the distribution of extrinsic substitutional impurities in zirconia or YSZ systems. Therefore, a comprehensive theoretical study of impurity segregation is essential to fundamental understanding of impurity segregation in YSZ and to the further development of hot-corrosion-resistant YSZ-based TBCs.

While density functional theory (DFT) is currently the most successful approach to compute the total energy and electronic structure of matter, no DFT study of the YSZ GB yet exists. This is because YSZ is a chemically-disordered material with respect to the distribution of oxygen vacancies (V_O) and yttrium dopants (Y_{Zr}). [47] This disorder, combined with high doping concentrations of about 6-10 mol%, complicates first-principles calculations via DFT, and thus prior DFT calculations of YSZ have generally been limited to relatively simple bulk structures. For example, thanks to the use of a 96-atom bulk supercell model of YSZ, it was possible to evaluate the stability of 453 unique structures from first-principles DFT calculations. [313]

In this work, we used first-principles DFT calculations to examine Σ5 (310)/[001] symmetric tilt YSZ GBs, as well as two closely related GBs of pristine zirconia and hafnia, and carried out a comprehensive analysis of impurity segregation in these systems. In fact, hafnia and zirconia share many similarities. Zr and Hf display nearly identical chemistry, [314] Zr^{4+} and Hf^{4+} have similar ionic radii of 0.86 and 0.85 Å, [315, 316] and both zirconia and hafnia crystallize in the same monoclinic, tetragonal, and cubic phases with comparable lattice parameters. [317] Hafnia may therefore serve as a valuable point of comparison with zirconia and YSZ in our study of substitutional impurity segregation to GBs. This article is divided into three sections. First, we compare the structural and energetic properties of the pristine zirconia and hafnia GB

models. Second, we examine the segregation tendencies of experimentally-relevant impurities in the zirconia and hafnia GB structures. Finally, we generate a series of candidate YSZ GB models, assess their relative stability, and study impurity segregation in the lowest-energy model.

6.2 Computational Details and Structural Models

DFT calculations were carried out using the Vienna *ab initio* Simulation Package (VASP). [104] The projector augmented wave (PAW) [97] pseudopotentials were employed for electron-ion interactions. The generalized gradient approximation (GGA) parametrized by Perdew-Burke-Ernzerhof (PBE) [98] was used to describe the electron exchange-correlation potentials. A 400 eV cut-off energy for the plane wave basis set was used during structural relaxation, and a $2 \times 2 \times 1$ Γ-centered *k*-point mesh is well-converged for self-consistent calculations. Subsequent single-point total energy calculations were carried out using the Gaussian method with a $4 \times 4 \times 1$ Γ-centered *k*-point mesh, with a 480 eV cut-off energy for the plane wave basis set. All the atomic positions were relaxed until all components of the residual forces were smaller than 0.03 eV/Å, and the convergence threshold for self-consistent-field iteration was set to 10^{-5} eV.

6.3 Results and Discussion

6.3.1 Grain Boundary Structures

We begin by comparing the structural properties of pristine grain boundaries in cubic ZrO_2 and HfO_2. To do so, we generated Σ5 (310)/[001] symmetric tilt GBs of cubic ZrO_2 and cubic HfO_2 from optimized unit cells of each material. Unless otherwise specified, henceforth ZrO_2 and HfO_2 refer to each respective material in its cubic phase. The optimized lattice parameters of the ZrO_2 and HfO_2 unit cells are 5.14 Å and 5.08 Å, respectively, which are consistent with the respective bulk experimental values of 5.10 Å and 5.08 Å. [317] Our calculated lattice parameters

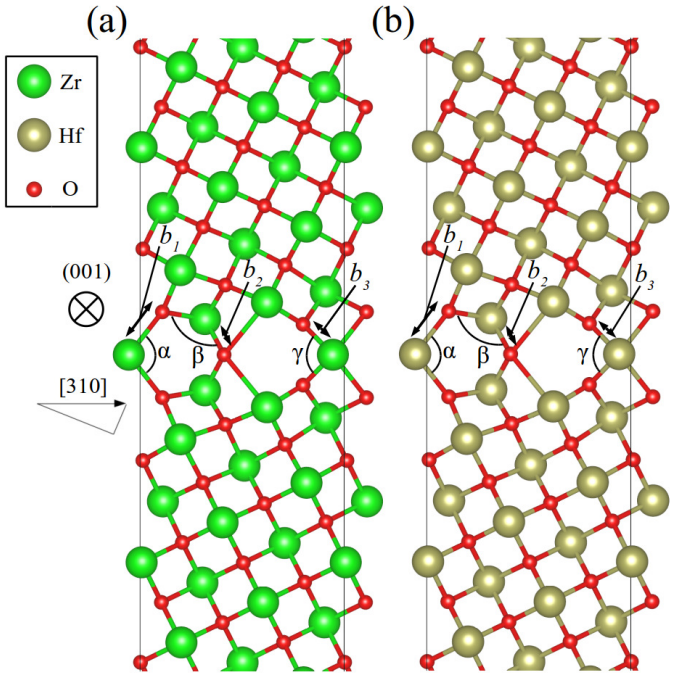

Figure 6.1: Structural depiction of the relaxed Σ5 (310)/[001] symmetric tilt GB structures of cubic (a) ZrO_2 and (b) HfO_2. For clarity, only the area near the GB core is shown.

for ZrO_2 and HfO_2 also agree closely with those reported in prior theoretical work. [318, 319] We note that the cubic phases of bulk ZrO_2 and HfO_2 are typically high-temperature phases. [315,320] However, thin films of both ZrO_2 and HfO_2 up to 1000 Å have been observed in their cubic phase at room temperature, with respective lattice parameters of 5.0±0.5 Å and 5.1±0.5 Å. [317] Our GB structures are less than 100 Å in length, which is well within the thickness regime where the cubic phase can form. Therefore, we expect that our findings will remain sufficiently general to be relevant to experimental study.

The relaxed ZrO_2 and HfO_2 GB structures are depicted in Fig. 6.1a and 6.1b, respectively, showing that both structures are exceedingly similar. In both ZrO_2 and HfO_2 GB structures, the GB core region shows a high degree of lattice distortion while the grain interior region keeps a bulk-like symmetry. The evident qualitative similarity between the ZrO_2 and HfO_2 GB structures can be also verified by their local structural parameters. Calculated M–O bond lengths (labeled b_1, b_2, b_3) and O–M–O bond angles (labeled α, β, γ) within the GB cores of each system are

depicted in Table 6.1 (also see Fig. 6.1). These calculated values confirm that the ZrO_2 and HfO_2 GBs are nearly structurally identical. It is noted that the bond lengths within the HfO_2 GB core are slightly smaller than those within the ZrO_2 GB core. This is also consistent with prior experimental findings in which the Hf-O bond in monoclinic HfO_2 is roughly 1% shorter than the Zr-O bond in monoclinic ZrO_2. [315]

Table 6.1: Calculated bond angles (α, β, and γ) and bond lengths (b_1, b_2, and b_3) with the ZrO_2 and HfO_2 grain boundary core.

	ZrO_2	HfO_2
α	85.508	85.184
β	90.749	90.884
γ	70.598	70.957
b_1	2.526	2.489
b_2	2.155	2.116
b_3	2.101	2.072

We next studied the relative stability of ZrO_2 and HfO_2 GB structures by calculating their GB energy (σ) using the following formula:

$$\sigma = (E_{GB} - E_{Bulk} - p\mu_M - q\mu_O)/A \tag{6.1}$$

, in which E_{GB} and E_{Bulk} denote the total energy of the GB structure and the total energy of a bulk MO_2 (M=Zr and Hf) supercell having the same number of formula units, respectively. μ_M and μ_O are the chemical potentials of M and O, and p and q denote the number of stoichiometrically excessive M and O ions, respectively. Since the modeled Σ5 (310)/[001] ZrO_2 and HfO_2 GB systems retain bulk stoichiometry, the above formula can be further reduced to:

$$\sigma = (E_{GB} - E_{Bulk})/A \tag{6.2}$$

The calculated respective σ values for the ZrO_2 and HfO_2 GB systems are 2.35 J/m^2 and 2.72 J/m^2. Our calculated σ value for ZrO_2 is consistent with the molecular dynamics (MD) calculated

value of 2.8 J/m^2 previously reported by Fisher *et al*. [321] For HfO_2, our calculated σ value is also consistent with the 2.92 J/m^2 reported in a prior DFT work. [319] In short, all these results show that our pristine ZrO_2 and HfO_2 GB models are suitable for impurity segregation analysis.

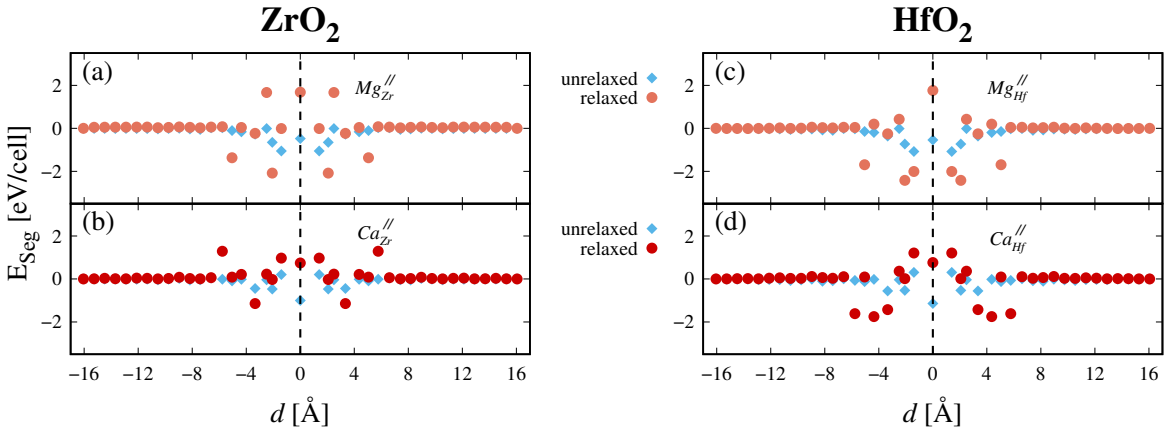

Figure 6.2: Calculated segregation energies (E_{seg}) of divalent impurities with respect to distance d from the central GB plane in the Σ5 (310)/[001] ZrO_2 and HfO_2 GBs. (a) Mg and (b) Ca in the ZrO_2 GB, and (c) Mg and (d) Ca in the HfO_2 GB. In this and subsequent segregation energy figures, the vertical dashed black lines indicate the central GB plane.

6.3.2 Impurity Segregation in ZrO_2 and HfO_2 GBs

Divalent Impurities

To determine the preferred positions of relevant substitutional impurities in the ZrO_2 and HfO_2 GBs, we built a series of structures by creating substitutional defects at each non-equivalent Zr (Hf) site. Each structure bears only one substitutional dopant, yielding an impurity concentration of 1.25%. On the basis of the composition analysis of sand-induced engine deposits by Smialek in 1991, [287] herein we modeled six possible dopants. They can be divided into three groups based on their typical oxidation states: divalent cations (Mg, Ca), trivalent cations (Al, Y), and tetravalent cations (Si, Ti). A table of these dopants, and their typical oxidation states and ionic radii, is shown below for convenience.

We first investigated the segregation tendency of divalent impurities Mg and Ca in ZrO_2

Table 6.2: List of oxidation states and ionic radii of the host ions (Zr and Hf) and relevant divalent, trivalent, and tetravalent impurities in the ZrO_2 and HfO_2 grain boundary.

Element	Oxidation State	Ionic Radius [322] [Å]
Zr	+4	0.86
Hf	+4	0.85
Mg	+2	0.86
Ca	+2	1.14
Al	+3	0.68
Y	+3	1.04
Si	+4	0.54
Ti	+4	0.74

and HfO_2 by calculating their segregation energies. The segregation energy of a defect can be written:

$$E_{seg,d} = E_{GB,d} - E_{GB,ref} \tag{6.3}$$

, where $E_{GB,d}$ is the total energy of the GB system with a defect at position d, and $E_{GB,ref}$ is the total energy of the system containing a defect in the reference state. Note that in this convention, negative segregation energies imply energetic favorability. In systems bearing a charged extrinsic acceptor, a suitable number of electrons were added to the overall supercell through charge compensation by a homogeneous background charge in our calculations. To clearly understand the influence of structural relaxation on the impurity segregation behavior, we also calculated the segregation energy for the unrelaxed ZrO_2 and HfO_2 GB models.

The segregation energies of divalent impurities Mg and Ca in ZrO_2 and HfO_2 are plotted in Fig. 6.2 with respect to distance d from the central GB plane. In the unrelaxed GB structures of both ZrO_2 and HfO_2, the calculated E_{seg} of Mg and Ca is ≈ 0 when the defect is located more than 4 Å from the GB plane. E_{seg} of Mg (Fig. 6.2a, c) is slightly below zero at the GB plane, and reaches a global minimum adjacent to the GB plane (d = 1.4 Å). E_{seg} of Ca (Fig. 6.2b, d), by contrast, reaches a global minimum at the GB plane (d = 0 Å), and is positive adjacent to the GB plane. The calculated segregation profiles also show that, for the unrelaxed GB models, E_{seg}

for Mg_{Zr} and Mg_{Hf} are nearly identical and the same is true for Ca_{Zr} and Ca_{Hf}. For example, minimum unrelaxed E_{seg} for Mg_{Zr} and Mg_{Hf} are both -1.1 eV, while those for Ca_{Zr} and Ca_{Hf} are -1.0 eV and -1.1 eV, respectively. These results indicate that E_{seg} in the unrelaxed GB models is nearly independent of host material.

In the relaxed ZrO_2 and HfO_2 GB systems, E_{seg} of both Mg and Ca is ≈ 0 in the grain interior when the defect is located more than about 6 Å from the GB plane, which indicates that the width of the GB core is roughly 12 Å. This width is in excellent agreement with experimental measurements of the GB core width in pristine YSZ of about 10 - 12 Å. [312, 323] Also the minimum E_{seg} of Mg impurity is found at 2 Å from the GB plane while that of Ca impurity is around 4 Å from the GB plane in both ZrO_2 and HfO_2 GBs. This indicates that Mg tends to be nearer to the GB plane than Ca. As shown in Fig. 6.2a and c, the lowest E_{seg} of Mg impurity is about -2.1 eV in the ZrO_2 GB and -2.4 eV in the HfO_2 GB, and that of Ca impurity is about -1.1 and -1.7 eV, respectively. In addition, it is noted that E_{seg} of Mg in the relaxed case is about 1 eV lower than that in the unrelaxed case, indicating that structural relaxation significantly influences E_{seg}. Therefore, the unrelaxed segregation energies will not be discussed from this point forward, and they are included in the subsequent figures for completeness and comparison only. Several major conclusions can be drawn by analyzing our results:

(i) E_{seg} values for both Mg and Ca in the HfO_2 GB are more negative than those in the ZrO_2 GB. In other words, GB segregation for these impurities is more pronounced in HfO_2 than in ZrO_2, suggesting that HfO_2 may be more susceptible to GB attack by divalent impurities.

(ii) In both ZrO_2 and HfO_2, Mg has more negative E_{seg} than Ca, indicating that Mg has a greater tendency to segregate to the GB core. To the best of our knowledge, no experimental GB segregation data for Mg exists in YSZ. However, in ceria-stabilized t–ZrO_2, Hwang *et al*. did find that Mg segregates more strongly than does Ca using Auger electron spectroscopy (AES) and X-ray photoelectron spectroscopy (XPS). [12] In particular, they reported an enrichment factor of 6.5 for Mg, and 5.0 for Ca, where the enrichment factor is defined as C_{gb}/C_{bulk}. In fact,

a later work by Kowalski *et al*. found that Ca could also segregate to the GB in *c*–8YSZ using secondary-ion mass spectrometry. [304]

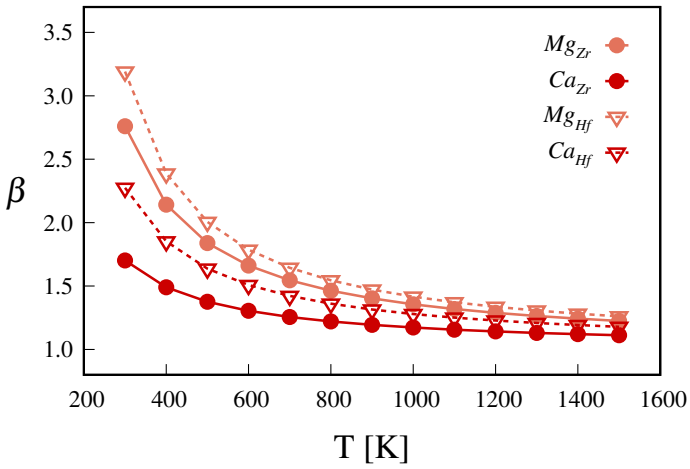

Figure 6.3: Calculated GB enrichment factors (β) for Mg and Ca as a function of temperature (K) in the Σ5 (310)/[001] ZrO_2 and HfO_2 GB models.

Next to have a comparison with these experimental studies, we calculated quantitative GB enrichment factors at the lowest-energy defect positions in both ZrO_2 and HfO_2 using Langmuir-McLean adsorption isotherm equations as below: [324, 325]

$$\frac{X_{GB}}{X^o_{GB} - X_{GB}} = \frac{X_b}{1 - X_b} \exp(-\Delta G / k_B T) \tag{6.4}$$

where X_{GB} is the concentration of a given impurity at the GB, X^o_{GB} is the GB fraction available at saturation, and X_b is the concentration in the bulk. In the dilute limit, Eq. 4 can be reduced to:

$$\beta = \frac{X_{GB}}{X_b} = \exp(-\Delta G / k_B T) \tag{6.5}$$

where β is the GB enrichment factor and ΔG is the free energy of segregation. The calculated GB enrichment factors (β) for Mg and Ca in ZrO_2 and HfO_2 are presented in Fig. 6.3 with respect to temperature. At 300 K, our calculated β values for Mg_{Zr} and Ca_{Zr} are 2.7 and 1.7, respectively. These values are both somewhat smaller than the respective experimental β values

of 6.5 and 5.0 for Mg and Ca in ceria-stabilized t–ZrO_2 reported by Hwang *et al*. [12] However, the trend is the same for our theoretical calculations and the experimental values, namely that Mg segregates more strongly than Ca in ZrO_2. This trend is also reproduced in our calculations for HfO_2. However, β values for Mg_{Hf} and Ca_{Hf} at 300 K are 3.2 and 2.3, indicating that the segregation tendency for both impurities is more pronounced in HfO_2 than in ZrO_2. Fig. 6.3 also shows that β decreases with temperature, saturating at roughly 1400 K with respective β values for Mg_{Zr} and Ca_{Zr} of 1.2 and 1.1, which indicates that the difference in β for Mg and Ca is diminished at high temperatures. Our calculations for both ZrO_2 and HfO_2 indicate that Mg is a stronger segregant than Ca, which agrees with the experimental results of Hwang *et al*. [12]

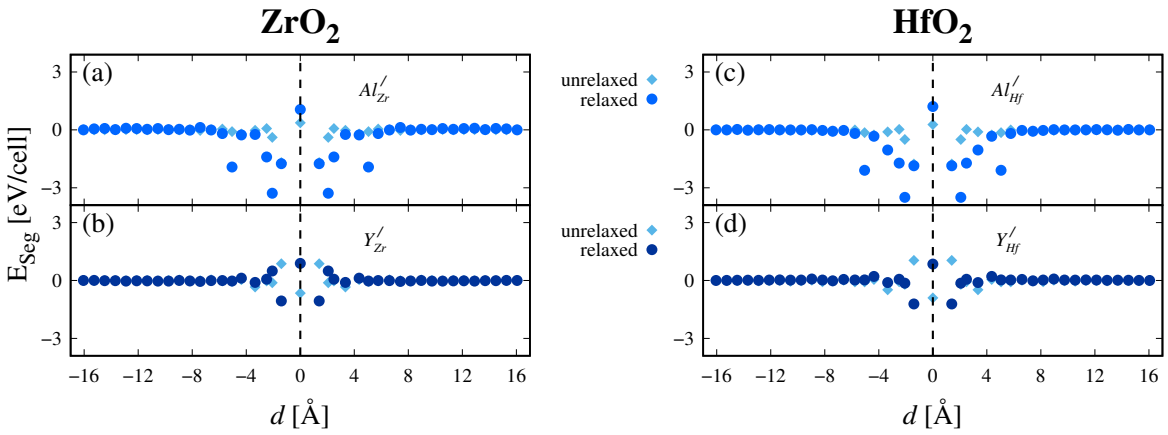

Figure 6.4: Calculated segregation energies (E_{seg}) of trivalent impurities with respect to distance d from the central GB plane in the Σ5 (310)/[001] ZrO_2 and HfO_2 GBs. (a) Al and (b) Y in the ZrO_2 GB, and (c) Al and (d) Y in the HfO_2 GB.

Trivalent Impurities

The segregation energies of trivalent impurities Al and Y in ZrO_2 and HfO_2 are plotted in Fig. 6.4 with respect to distance d from the central GB plane. As in the case of the divalent impurities, E_{seg} for Al and Y is ≈ 0 in the grain interior, and most negative near the GB plane, suggesting a general segregation to the GB core. For Al impurity, as shown in Fig. 6.4a and c, the lowest E_{seg} is about -3.3 eV in the ZrO_2 GB and -3.4 eV in the HfO_2 GB, both around 2.1 Å

from the GB plane. For Y impurity, the lowest E_{seg} is about -1.1 eV in the ZrO_2 GB and -1.2 eV in the HfO_2 GB at d = 1.4 Å, see Fig. 6.4b and d, which are significantly smaller than those of Al impurity. These results indicate that while Al and Y both tend to segregate to the GB core, Al has a much greater segregation tendency than Y. To have a quantitative analysis of the Al (Y) segregation behavior, we also calculated their GB enrichment factors β in the ZrO_2 and HfO_2 GBs using the Langmuir-McLean adsorption isotherm (see Fig. 6.5). Our calculated β values at 300 K are 4.9 for Al and 1.7 for Y in the ZrO_2 GB, indicating that Al has a much stronger segregation than Y in the ZrO_2 GB.

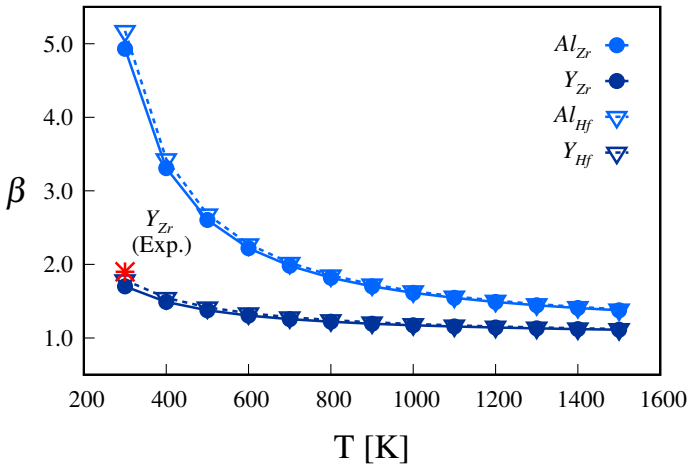

Figure 6.5: Calculated enrichment factors (β) for Al and Y as a function of temperature (K) in the Σ5 (310)/[001] ZrO_2 and HfO_2 GB models. The red star indicates the experimental GB enrichment factor for Y in YSZ. [12, 13]

In fact, a prior experimental study has indicated that Al segregates strongly to ZrO_2 grain boundaries. [305] By using electron probe microanalysis (EPMA), Guo *et al*. studied 1-5 mol% Al_2O_3 doped *c*–9YSZ and found that Al was mainly concentrated at grain boundaries, and that the extent of Al segregation was proportionate to the Al_2O_3 doping concentration. [305] At high doping concentrations, they found the formation of distinct Al-rich crystalline and amorphous GB phases, which further confirms the Al segregation behavior. For Y impurity, Dickey *et al*. studied Σ5 (310)/[001] and near-Σ13 (310)/[001] grain boundaries of *c*–10YSZ, and by contrast

found a modest segregation tendency in YSZ, and an absence of Y-rich GB phases even at high doping concentrations. [13] The authors also found an ≈ 9 mol% enrichment of Y at the GBs relative to the grain interior, yielding an enrichment factor of 1.9. [13] Interestingly, the same Y enrichment factor of 1.9 was also reported in the *t*–4YSZ system from XPS. [12] These results are well consistent with our calculated value of 1.7 for Y. [12, 13]

In addition, it is noted that for the divalent impurities, the calculated β values in the HfO_2 GB are much higher than that in the ZrO_2 GBs, while for the trivalent impurities, the β values are very similar in the ZrO_2 and HfO_2 GBs. This indicates that the segregation tendency of trivalent impurities Al and Ca is nearly independent of host material.

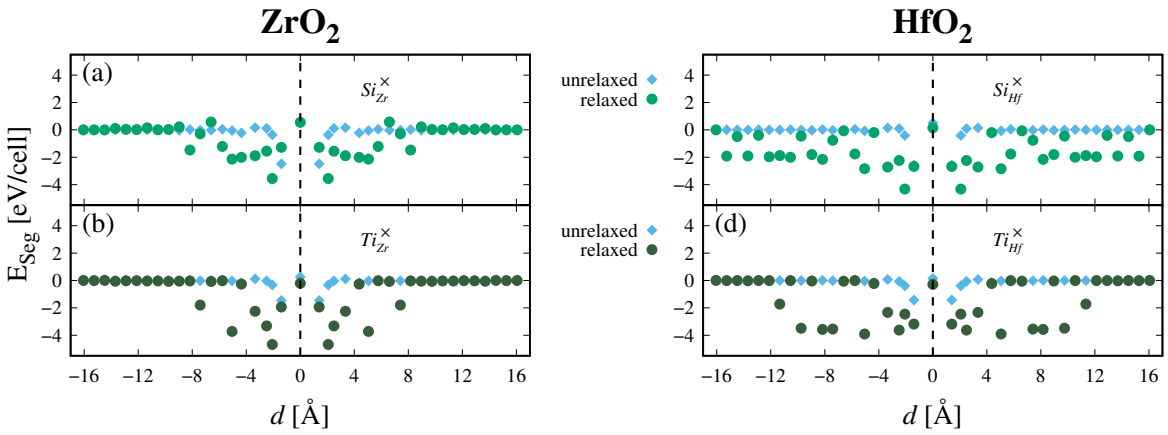

Figure 6.6: Calculated segregation energies (E_{seg}) of tetravalent impurities with respect to distance *d* from the central GB plane in the Σ5 (310)/[001] ZrO_2 and HfO_2 GBs. (a) Si and (b) Ti in the ZrO_2 GB, and (c) Si and (d) Ti in the HfO_2 GB.

Tetravalent Impurities

The calculated segregation energies for tetravalent impurities Si and Ti in the ZrO_2 and HfO_2 GBs are plotted in Fig. 6.6 with respect to distance *d* from the GB plane. In the ZrO_2 GB (Fig. 6.6a, b), E_{seg} for Si and Ti is ≈ 0 in the grain interior, and most negative near the GB plane, suggestive of a general segregation to the GB core. In the HfO_2 GB, similarly, E_{seg} for Si and Ti is most negative near the GB plane (see Fig. 6.6c, d). However, unlike in the ZrO_2 GB, significantly

negative E_{seg} values for Si and Ti are also found far from the GB plane. For example, E_{seg} for Ti_{Hf} is -3.5 eV at d = 9.8 Å, as compared to -3.6 eV in the GB core (d = 2.5 Å). Our calculations indicate that tetravalent impurities Si and Ti have a much smaller segregation tendency in HfO_2 than in ZrO_2. This result is very different from the case of trivalent and divalent impurities. The trivalent impurities Al and Y exhibit a very similar segregation tendency in HfO_2 and ZrO_2 (Fig. 6.4), while the divalent impurities Mg and Ca have a greater segregation tendency in HfO_2 than in ZrO_2 (Fig. 6.2).

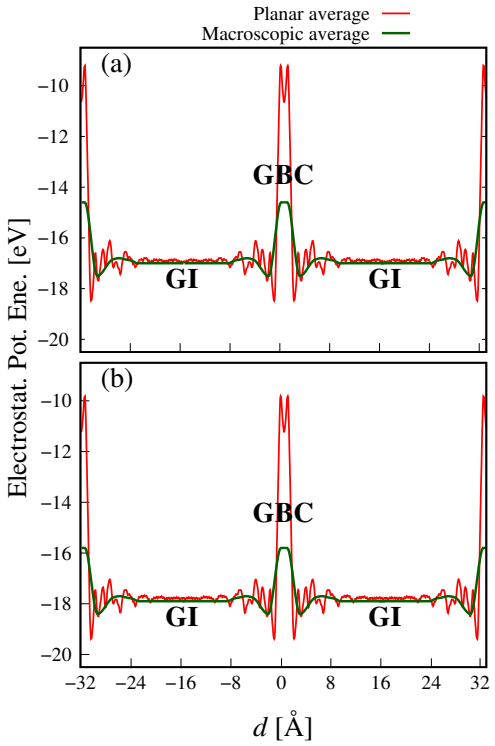

Figure 6.7: Calculated electrostatic potential energy (eV) in the ZrO_2 (a) and HfO_2 (b) GBs with respect to distance (d) along the c-axis (that is normal to the GB plane).

In the ZrO_2 GB, Ti has a stronger segregation tendency than Si, and the minimum E_{seg} is -4.7 for Ti and -3.6 eV for Si, as shown in Fig. 6.6a and b. Several prior experimental studies have indicated a segregation of Si to GBs of stabilized ZrO_2. For example, using scanning-transmission electron microscopy, Aoki *et al*. examined 15 mol%-CaO-stabilized t–ZrO_2 GBs, and found that trace Si impurities indeed segregated to the GB core. [306] Interestingly, Guo *et al*.'s EPMA study

of 1-5 mol% Al_2O_3-doped-*c*–9YSZ indicated that trace Si impurities were present only within amorphous GB phases rather than crystalline GBs. [305] The different segregation behavior of Si impurity in the amorphous and crystalline GBs is beyond the scope of the present study, and further experimental studies might be useful to expose the underlying mechanism.

In addition, it is noted that the tetravalent cations show a very different segregation profile from the divalent and trivalent cations. For instance, Si and Ti tend to segregate to a wide area up to 15 Å from the GB plane, while the divalent and trivalent impurities tend to segregate to a narrow area within roughly 4 Å of the GB plane, see Fig. 6.2 and 6.4. To explore the origin of this difference, we calculated electrostatic potential energies (EPE) normal to the GB plane for the relaxed pristine ZrO_2 and HfO_2 GB structures, see Fig. 6.7. The EPE is dependent on the interaction between electrons and ions in the crystal, and thus is related to the number of ions per unit volume. Accordingly, a region with low volumetric ionic density is expected to have less negative EPE. In both ZrO_2 and HfO_2 GBs, the EPE is significantly less negative at the GB plane and more negative in the grain interior (GI). Moreover, there is a low EPE region about 4 Å wide just beyond the GB plane, which is similar to the width of the segregation region we have calculated for the divalent and trivalent impurities, see Fig. 6.2 & Fig. 6.4. Our prior theoretical work has shown that positively-charged oxygen vacancies in $SrTiO_3$ form preferentially in regions with less negative electrostatic potential energy. [326] Therefore, the impurities with negative relative charge are expected to be driven to regions with more negative EPE. In the ZrO_2 and HfO_2 GBs, these low EPE regions are near the GB plane. This can explain why the divalent and trivalent impurities with negative relative charge tend to segregate near the GB plane. In contrast, the tetravalent impurities with neutral relative charge, Si and Ti, show a much wider segregation segregation profile than the divalent and trivalent impurities, see Fig. 6.6.

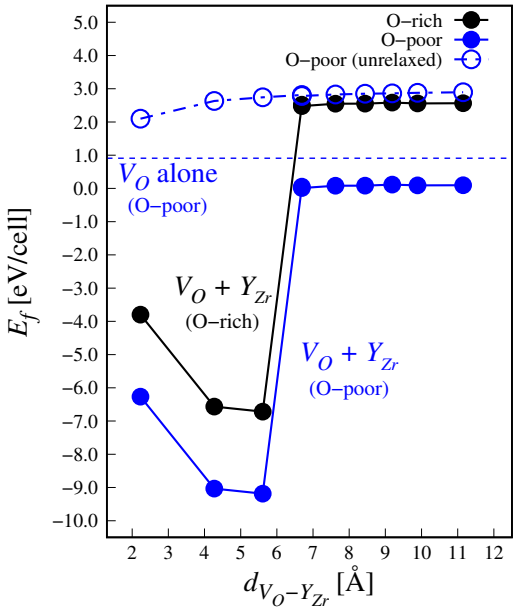

Figure 6.8: System formation energy in bulk Y-doped cubic ZrO_2 with respect to the distance between oxygen vacancy and substitutional Y ($d_{V_O - Y_{Zr}}$) under oxygen-rich (black) and oxygen-poor (blue) conditions. The blue horizontal dashed line indicates the oxygen vacancy formation energy in a pristine 324-atom supercell of cubic ZrO_2.

6.3.3 Yttria-Stabilized Zirconia

Distribution of Intrinsic Defects in Bulk YSZ

From a practical viewpoint, exploring impurity segregation behavior in cubic yttria-stabilized zirconia (c–YSZ) GBs can provide more relevant information about CMAS attack in YSZ-based thermal coatings. To model c–YSZ GBs, there are two possible approaches. The first approach is to generate a bulk structure of c–YSZ that contains both oxygen vacancies (V_O) and Y substitutions at Zr sites (Y_{Zr}), and then build the GB model from this bulk structure. However, this approach is not practical for DFT calculations because the generated GB models from the bulk c–YSZ unit cell would be prohibitively large. For example, by starting from a 96-atom unit cell of bulk YSZ with yttria concentration of 6.25%, we were able to generate a symmetric tilt $\Sigma 5$ (310)/[001] GB model that consists of 1900 atoms. [327] The other approach is to build c–YSZ GBs from a pristine ZrO_2 unit cell and then introduce a suitable number of V_O and Y_{Zr},

making the composition comparable with the experimental case. First, one needs to determine the optimal distance between oxygen vacancies and yttrium dopants in the c–YSZ GB model ($d_{V_O-Y_{Zr}}$), which can be approximated from a bulk YSZ model. To do this, we built a 324-atom $3\times3\times3$ supercell of bulk cubic ZrO_2 in which the central Zr atom was doped with Y, and nine non-equivalent oxygen sites were identified. Next we relaxed each of these nine structures, and calculated the formation energy as a function of the V_O–Y_{Zr} distance using the following equation:

$$E_f = E_{YSZ} - E_{pris} + \mu_O + \mu_{Zr} - \mu_Y \tag{6.6}$$

, where E_f is the formation energy of the YSZ model, E_{YSZ} is the total energy of the YSZ, E_{pris} is the total energy of the pristine ZrO_2 supercell, and μ_X represents the chemical potential of element X (X = O, Zr, and Y). To determine the influence of local structural relaxation on the formation energy, we also calculated E_f for the unrelaxed structures. The calculated E_f for both relaxed and unrelaxed structures with respect to $d_{V_O-Y_{Zr}}$ are plotted in Fig. 6.8. To have a clear comparison, we also calculated the formation energy of one oxygen vacancy ($E_f(V_O)$) in the pristine ZrO_2 model. Two major conclusions can be drawn:

i) E_f in YSZ is significantly lower than the $E_f(V_O)$ in pristine ZrO_2, regardless of $d_{V_O-Y_{Zr}}$, which suggests that Y strongly promotes V_O formation.

ii) Structural relaxation plays a significant role in the E_f. For the unrelaxed YSZ models, the lowest E_f is found when the V_O is at the nearest neighbor position to the Y atom, and E_f increases with $d_{V_O-Y_{Zr}}$. For the relaxed YSZ models, the lowest E_f is found when the V_O is at the next-nearest-neighbor positions relative to Y (d = 4.3, 5.6 Å). This means that the optimal $d_{V_O-Y_{Zr}}$ is approximately 4-5 Å. This result is also consistent with prior experimental work in which oxygen vacancies typically occupy the next-nearest-neighbor position with respect to Y. [328, 329]

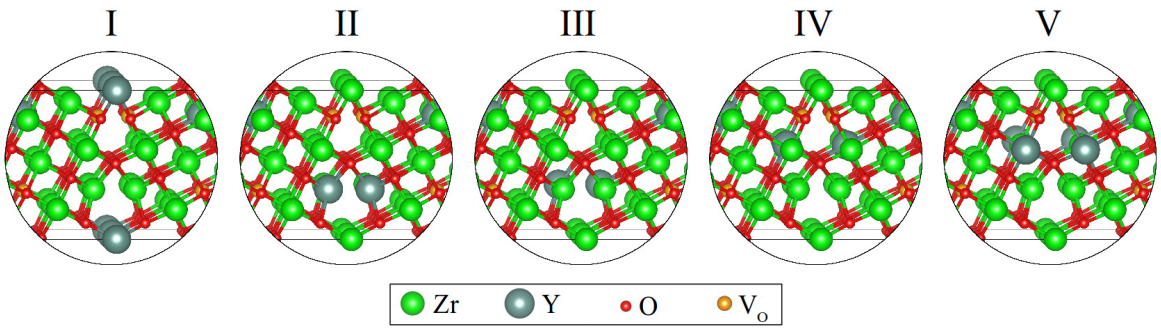

Figure 6.9: Structural depictions of the GB core in each YSZ model. Yttrium ions are identified as dark grey, while oxygen vacancy sites are depicted in orange.

Grain Boundary Structures

On the basis of experimental [13, 302] and our computational findings, an ideal c–YSZ GB structure should satisfy the following conditions: (1) 8-10 mol% yttria doping concentration, (2) yttria enrichment in the GB core, (3) overall charge neutrality, (4) relatively uniform yttria distribution in the GB interior, and (5) relatively consistent $d_{V_O - Y_{Zr}}$. Note that although overall charge neutrality should be maintained, oxide GB cores are often charged because of the segregation of oxygen vacancies. [330] Indeed, a prior experimental study has shown that YSZ GBs tend to be positively charged due to V_O segregation which is more pronounced than that of Y_{Zr}. [312] In light of these considerations, we first generated a symmetric tilt GB model that consists of 240 atoms based on pristine ZrO_2, and then introduced some yttrium atoms and oxygen vacancies. To have a charge neutral YSZ GB model with 10 mol% yttria concentration, we could introduce eight Y_{Zr} dopants and four V_O. In addition, to account for the experimental V_O excess at YSZ GBs, we included another four V_O near the GB cores and built five distinct GB models whose local structures are shown in Fig. 6.9. The introduction of V_O also provides a charge compensation mechanism for our impurity segregation calculations. We list the relative energies of these five GB models in Table 6.3. It shows that model IV has the lowest energy, and therefore this model was selected for further study of impurity segregation.

Table 6.3: Calculated relative energy (ΔE) with respect to that of model IV for the five YSZ grain boundary models.

Model	ΔE (eV)
I	0.57
II	2.93
III	3.86
IV	0
V	2.21

Impurity Segregation in the YSZ GB

We calculated segregation energies for the relevant impurities in the YSZ GB model by systematically creating substitutional extrinsic defects at each non-equivalent Zr site. As in the case of the ZrO_2 and HfO_2 calculations, we studied six key elements which are relevant to the sand-induced TBC damage: Mg, Ca, Al, Y, Si, and Ti. We particularly focus on the differences between the impurity segregation profiles in ZrO_2 and YSZ. The calculated segregation energies for each impurity in the YSZ GB model are presented in Fig. 6.10. For the divalent impurities, Ca shows a greater segregation tendency than Mg in the YSZ model, see Fig. 6.10a and b. This is unlike the case in ZrO_2, where our calculated E_{seg} for Mg tended to be more negative than that of Ca. This could be due to the oxygen vacancy excess at the YSZ GB that enables the lattice to favorably accommodate the large Ca^{2+} cation.

For the trivalent impurities, Al shows a greater segregation tendency than Y in the YSZ model, see Fig. 6.10c and d. This is similar to the case in ZrO_2, where Al showed a strong segregation tendency and Y showed a modest one. However, Y shows an even weaker segregation tendency in the YSZ model than in ZrO_2. This is because our IV YSZ model already has a ≈10 mol% enrichment of yttrium in the GB core relative to the grain interior, which is close to the optimal enrichment factor of 9 mol% experimentally reported. [13] Therefore, additional yttrium near the GB plane would be expected to be energetically unfavorable.

For the tetravalent impurities, Ti shows a remarkably weaker segregation tendency than Si

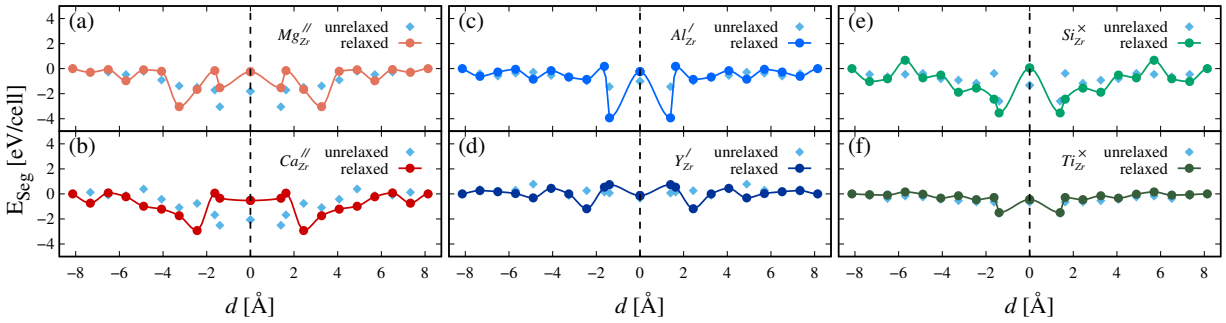

Figure 6.10: Calculated segregation energies (E_{seg}) [eV] of divalent (a, b), trivalent (c, d), and tetravalent (e, f) impurities with respect to the distance d [Å] from the central GB plane in the Σ5 (310)/[001] YSZ GB.

in the YSZ model, see Fig. 6.10e and f. This is quite unlike the case of ZrO_2, where Ti shows a stronger segregation tendency than Si. In fact, a prior experimental study of a *c*–YSZ GB found a very weak GB segregation tendency for Ti using SIMS, [331] which is in good agreement with our calculations. This is correlated with the high solubility of TiO_2 in *c*–YSZ of at least 30 mol% observed in experiment. [332] In contrast, the solubility of Si in CaO-stabilized-ZrO_2 is exceedingly low, on the order of 25 ppm. [306] This may explain why Si has a much stronger segregation tendency in YSZ, which is also consistent with our calculations.

6.4 Conclusions

In summary, we have studied the structural and energetic properties of pristine and doped Σ5 (310)/[001] GB structures of cubic ZrO_2, HfO_2, and yttria-stabilized ZrO_2 (YSZ) using first-principles density functional theory calculations. Our results can be summarized as follows:

(1) The pristine ZrO_2 and HfO_2 GBs share similar structural characteristics, and have respective GB energies of 2.35 J/m^2 and 2.72 J/m^2.

(2) Substitutional impurities with different valence states show different segregation behavior in the ZrO_2 and HfO_2 GBs. The divalent (Mg, Ca) and trivalent (Al, Y) impurities tend to segregate to a narrow region within about 4 Å of the GB plane, while the tetravalent (Si, Ti)

impurities have a much more scattered segregation profile which extends up to 15 Å from the GB plane.

(3) The GB enrichment factor (β) of Mg is greater than that of Ca, while for the trivalent impurities β of Al is significantly higher than that of Y. In particular, our calculated β value for Y in ZrO_2 is 1.7 at 300 K, which agrees with the experimental value of 1.9.

(4) In the YSZ GB model, Mg, Ca, and Si show a strong segregation tendency, while Ti shows a very weak segregation tendency.

This work has, for the first time, demonstrated first-principles density functional theory calculations of impurity segregation in a YSZ GB system containing both oxygen vacancies and yttrium dopants. Our study reveals some fundamental understanding of the substitutional impurity segregation behavior in ZrO_2, HfO_2, and YSZ GBs, which may be useful in the development of next-generation YSZ-based thermal barrier coatings.

6.5 Acknowledgements

Chapter 6, in full, is currently being submitted for publication of the material "First-Principles Study of Impurity Segregation in Zirconia, Hafnia, and Yttria-Stabilized-Zirconia Grain Boundaries". Maziar Behtash, Jian Luo, Kesong Yang. The dissertation author was the primary investigator and author of this paper.

Chapter 7

Summary and Future Directions

Defects such as grain boundaries, oxygen vacancies, and substitutional impurities are often present in polycrystalline materials, and their presence has significant effects on overall material properties. To engineer next-generation materials with novel functionality, or to improve the performance of present-day materials, we must therefore understand the ways in which material properties are influenced by defects. In this thesis we have focused on substitutional impurities, heterointerfaces, oxygen vacancies, and grain boundaries in metal oxide materials, specifically SnO_2, $LaAlO_3$, $SrTiO_3$, ZrO_2, HfO_2, and yttria-stabilized ZrO_2. Our goal has been to deepen the understanding of defects in these systems, by elucidating the energetic and/or electronic properties of defect-bearing systems.

We first considered a rare class of materials known as transparent conducting oxides (TCO). TCOs display both optical transparency and electronic conductivity, the coexistence of which is exceedingly rare in nature, enabling the functionality of important devices such as photovoltaic cells, cell phone digitizers, and light-emitting diodes. The typical TCO material, tin-doped indium oxide (ITO), suffers from substantial free-carrier absorption in the infrared and near-infrared range due to its very high charge carrier density ($\approx 10^{21}$ [cm^{-2}]) and relatively low free electron mobility ($\approx$40 [$cm^2V^{-1}s^{-1}$]). The cost of ITO continues to grow, as indium demand

outpaces production. These issues have stimulated research efforts to discover replacement materials. In Chapter 2, we investigated pentavalent-ion doped SnO_2 materials with potential as TCOs. We found that phosphorus-doped SnO_2 (PTO) compares favorably with well-known TCO materials antimony-doped SnO_2 (ATO) and tantalum-doped SnO_2 (TTO), in terms of its *n*-type conductive electronic structure and moderate formation energy. In addition, we showed that iodine doping of SnO_2 leads to the formation of impurity states which narrow the optical band gap. Finally, we showed that the theoretical charge carrier density of the pentavalent-ion doped SnO_2 systems is nearly identical, which suggests that the order-of-magnitude variations reported in experimental studies are due to variations in experimental conditions during the materials synthesis or characterization steps. Future work on this research topic is experimental synthesis and characterization of phosphorus-doped SnO_2, to determine if its exciting theoretical potential can be translated into practical applications.

We next turned to the study of a perovskite oxide heterointerface, specifically the $LaAlO_3/SrTiO_3$ (LAO/STO) heterostructure (HS). The two-dimensional electron gas (2DEG) formed at this interface possesses a wide variety of exciting electronic and magnetic properties. In Chapter 3, we explored the possibility of enhancing the interfacial 2DEG properties in LAO/STO via *n*-type layer doping with transition metals near the interface. We found that 2DEG charge carrier density and magnetism can be significantly enhanced by layer doping with Nb or Ta at the interfacial Ti site in LAO/STO. Moreover, we showed that these layer-doped HS are energetically-favorable relative to the undoped LAO/STO HS. Finally, we demonstrated that Nb or Ta layer doping at the Al site of the LAO/STO HS can enhance the quantum confinement of the interfacial 2DEG.

Strain applied on the STO substrate is another method capable of modulating 2DEG properties in the LAO/STO HS. In particular, biaxial compressive strain has been shown to increase the LAO film critical thickness necessary for 2DEG formation. Prior theoretical study has also proposed that polarization in the LAO film is capable of neutralizing the polar discontinuity

in LAO/STO, giving rise to insulating behavior under certain conditions. In Chapter 4, we demonstrated that the LAO film polarization and critical thickness in LAO/STO are closely linked. In particular, we found that the LAO film polarization declines with film thickness, and identified a critical polarization value above which 2DEG cannot form in LAO/STO. We also resolved the long-standing discrepancy between the experimental and theoretical charge carrier density values of the interfacial 2DEG in LAO/STO through the use of an appropriate vacuum slab model. We also investigated the effects of strain in LAO/STO, and found that the interfacial charge carrier density, electron mobility, and conductivity can all be enhanced by the application of [100] uniaxial tensile strain applied on the STO substrate. Finally, we discovered that the quantum confinement of the interfacial 2DEG in LAO/STO is also enhanced by [100] uniaxial tensile strain.

In Chapters 3 and 4 we described methods of enhancing 2DEG properties in the LAO/STO HS. We next turned to the study of the substrate of this system, STO, which displays a wide variety of exciting properties in its own right. Grain boundaries (GB) and oxygen vacancies in STO have been shown to significantly influence the bulk material properties. In Chapter 5, we examined termination stability and oxygen vacancy formation energy in a $\Sigma 5$ [001] twist GB of STO. We found that the SrO/SrO (S/S) and SrO/TiO_2 (S/T) GB terminations can form within the chemical potential range necessary to maintain bulk STO stability, but that the TiO_2/TiO_2 (T/T) GB termination cannot. We discovered that the optimal position of oxygen vacancies with respect to the GB plane is dependent on GB termination. Specifically, we found that oxygen vacancies tend to segregate adjacent to the GB layer in the S/S-terminated GB system, but precisely at the GB layer in the S/T-terminated GB system. Finally, we investigated the temperature- and pressure-dependence of oxygen vacancy formation in the S/S- and S/T-terminated GB systems, and found that oxygen vacancies can form in a much wider range of experimental conditions in the latter system. Thus, we showed that both the average position and likely concentration of oxygen vacancies in STO twist GBs depend on the GB termination, which may open a new

avenue in GB engineering of STO. Future work on this topic is to study twist grain boundaries of other complex oxide systems, such as $SrZrO_3$ which has shown potential as a thermal barrier coating, with the goal of elucidating termination stability and likely defect distributions with respect to the GB plane.

In Chapter 5 we investigated the segregation of intrinsic defects, namely oxygen vacancies, to STO grain boundaries. The GB segregation of extrinsic defects is also of great importance in the materials realm, giving rise to a host of possible effects including embrittlement, strengthening, or differential inter- and intra-grain electronic/ionic conductivity. One example of the importance of GB segregation can be found in the field of thermal barrier coatings (TBC) for gas turbine engines, which typically employ yttria-stabilized zirconia (YSZ) as a refractory. TBCs are critical materials systems which protect the metal turbine blades in gas turbine engines from the intense heat of the combustion chamber, enabling dramatic increases in operating temperature and hence efficiency and performance. Sand or particulate ingestion by gas turbine engines leads to the formation of calcium-magnesium-alumino silicate (CMAS), which attacks and degrades the TBC leading to turbine blade failure. Crucially, CMAS attack has been shown to occur preferentially at grain boundaries, and involves segregation of impurity elements to the GBs. In Chapter 6, we investigated the segregation of substitutional impurities to $\Sigma 5$ (310)/[001] GBs of cubic ZrO_2, HfO_2, and YSZ. We discovered a fundamental difference in the characteristic segregation profiles of aliovalent and isovalent substitutional impurities in ZrO_2 and HfO_2, and proposed that the local electrostatic potential energy influences the segregation energy of the aliovalent impurities. In addition, we successfully generated and structurally-optimized a complex cubic YSZ GB system containing high concentrations of both oxygen vacancies and substitutional yttrium dopants, which is the first time this has been accomplished using DFT. Moreover, we investigated the segregation tendencies of substitutional impurities in this complex YSZ GB system, and found that Si and Ca are strong segregants while Al, Ti, and Y are not. This work provided some fundamental understanding of impurity segregation in TBC-relevant materials. Future research

directions in this area are threefold. First, DFT study of yttria-stabilized hafnia (YSH) has not yet been accomplished, despite the fact that YSH has shown promise in surpassing YSZ in thermal barrier coatings. Second, twist grain boundaries of ZrO_2 and HfO_2 have never been studied using DFT, and this could provide new insights into the bulk material properties of polycrystalline TBCs. Third, an analysis of the consequences of impurity segregation in these fluorite oxide grain boundary systems, particularly embrittlement/strengthening.

In summary, our work has explored the structural, energetic, and electronic properties of defect-bearing metal oxide materials using first-principles density functional theory calculations. While technically this thesis may be considered basic scientific research, our studies have been motivated by real-world technological challenges, and demonstrate the power of first-principles calculations to elucidate the properties of complex material systems.

Bibliography

[1] Y. Muto, S. Nakatomi, N. Oka, Y. Iwabuchi, H. Kotsubo, and Y. Shigesato, "High-rate deposition of Ta-doped SnO_2 films by reactive magnetron sputtering using a SnTa metal-sintered target", *Thin Solid Films* **520**, pp. 3746 – 3750 (2012).

[2] Shoichiro Nakao, Naoomi Yamada, Taro Hitosugi, Yasushi Hirose, Toshihiro Shimada, and Tetsuya Hasegawa, "High mobility exceeding 80 cm^2 V^{-1} s^{-1} in polycrystalline Ta-doped SnO_2 thin films on glass using anatase TiO_2 seed layers", *Appl. Phys. Express* **3**, pp. 031102 (2010).

[3] Shoichiro Nakao, Naoomi Yamada, Taro Hitosugi, Yasushi Hirose, Toshihiro Shimada, and Tetsuya Hasegawa, "Fabrication of highly conductive Ta-doped SnO_2 polycrystalline films on glass using seed-layer technique by pulse laser deposition", *Thin Solid Films* **518**, pp. 3093 – 3096 (2010).

[4] H. Toyosaki, M. Kawasaki, and Y. Tokura, "Electrical properties of Ta-doped SnO_2 thin films epitaxially grown on TiO_2 substrate", *Appl. Phys. Lett.* **93**, pp. 132109 (2008).

[5] E. Shanthi, A. Banerjee, V. Dutta, and K. L. Chopra, "Electrical and optical properties of tin oxide films doped with F and (Sb+F)", *J. Appl. Phys.* **53**, pp. 1615–1621 (1982).

[6] E. Elangovan and K. Ramamurthi, "Studies on micro-structural and electrical properties of spray-deposited fluorine-doped tin oxide thin films from low-cost precursor", *Thin Solid Films* **476**, pp. 231 – 236 (2005).

[7] A. E. Rakhshani, Y. Makdisi, and H. A. Ramazaniyan, "Electronic and optical properties of fluorine-doped tin oxide films", *J. Appl. Phys.* **83**, pp. 1049–1057 (1998).

[8] Yi Hu and S.-H Hou, "Preparation and characterization of Sb-doped SnO_2 thin films from colloidal precursors", *Mater. Chem. Phys.* **86**, pp. 21 – 25 (2004).

[9] Xianjin Feng, Jin Ma, Fan Yang, Feng Ji, Fujian Zong, Caina Luan, and Honglei Ma, "Transparent conducting SnO_2:Sb epitaxial films prepared on α-Al_2O_3 (0001) by MOCVD", *Mater. Lett.* **62**, pp. 1779 – 1781 (2008).

[10] E. Shanthi, V. Dutta, A Banerjee, and K. L. Chopra, "Electrical and optical properties of undoped and antimony doped tin oxide films", *J. Appl. Phys.* **51**, pp. 6243–6251 (1980).

[11] Tetsuo Tsuchiya, F. Kato, T. Nakajima, K. Igarashi, and T. Kumagai, "Direct conversion of a metal organic compound to epitaxial Sb-doped SnO_2 film on a TiO_2 substrate using a KrF laser, and its resulting electrical properties", *Appl. Sur. Sci.* **255**, pp. 9808 – 9812 (2009).

[12] ShyhLung Hwang and IWei Chen, "Grain size control of tetragonal zirconia polycrystals using the space charge concept", *J. Am. Ceram. Soc.* **73**, pp. 3269–3277 (1990).

[13] Elizabeth C. Dickey, Xudong Fan, and Stephen J. Pennycook, "Structure and chemistry of yttriastabilized cubiczirconia symmetric tilt grain boundaries", *J. Am. Ceram. Soc.* **84**, pp. 1361–1368 (2001).

[14] Jose Rajan, Thavasi Velmurugan, and Ramakrishna Seeram, "Metal oxides for dye-sensitized solar cells", *J. Am. Ceram. Soc.* **92**, pp. 289–301 (2009).

[15] P. D. Ye, G. D. Wilk, B. Yang, J. Kwo, S. N. G. Chu, S. Nakahara, H.-J. L. Gossmann, J. P. Mannaerts, M. Hong, K. K. Ng, and J. Bude, "GaAs metaloxidesemiconductor field-effect transistor with nanometer-thin dielectric grown by atomic layer deposition", *Appl. Phys. Lett.* **83**, pp. 180–182 (2003).

[16] Paolo Francesco Manicone, Pierfrancesco Rossi Iommetti, and Luca Raffaelli, "An overview of zirconia ceramics: Basic properties and clinical applications", *J. Dent.* **35**, pp. 819 – 826 (2007).

[17] X.Q. Cao, R. Vassen, and D. Stoever, "Ceramic materials for thermal barrier coatings", *J. Eur. Ceram. Soc.* **24**, pp. 1 – 10 (2004).

[18] Junhua Li, Huazhen Chang, Lei Ma, Jiming Hao, and Ralph T. Yang, "Low-temperature selective catalytic reduction of NO_x with NH_3 over metal oxide and zeolite catalysts–A review", *Catal. Today* **175**, pp. 147 – 156 (2011).

[19] Tonio Buonassisi, Andrei A. Istratov, Matthew A. Marcus, Barry Lai, Zhonghou Cai, Steven M. Heald, and Eicke R. Weber, "Engineering metal-impurity nanodefects for low-cost solar cells", *Nat. Mater.* **4**, pp. 676–679 (2005).

[20] M. K. Nowotny, L. R. Sheppard, T. Bak, and J. Nowotny, "Defect chemistry of titanium dioxide. Application of defect engineering in processing of TiO_2-based photocatalysts", *J. Phys. Chem. C* **112**, pp. 5275–5300 (2008).

[21] Harry L. Tuller and Sean R. Bishop, "Point defects in oxides: Tailoring materials through defect engineering", *Annu. Rev. Mater. Res.* **41**, pp. 369–398 (2011).

[22] Neil J. Lawrence, Joseph R. Brewer, Lu Wang, Tai-Sing Wu, Jamie Wells-Kingsbury, Marcella M. Ihrig, Gonghua Wang, Yun-Liang Soo, Wai-Ning Mei, and Chin Li Cheung, "Defect engineering in cubic cerium oxide nanostructures for catalytic oxidation", *Nano Lett.* **11**, pp. 2666–2671 (2011).

[23] David O. Scanlon, "Defect engineering of $BaSnO_3$ for high-performance transparent conducting oxide applications", *Phys. Rev. B* **87**, pp. 161201 (2013).

[24] Ning Zhang, Xiyu Li, Huacheng Ye, Shuangming Chen, Huanxin Ju, Daobin Liu, Yue Lin, Wei Ye, Chengming Wang, Qian Xu, Junfa Zhu, Li Song, Jun Jiang, and Yujie Xiong, "Oxide defect engineering enables to couple solar energy into oxygen activation", *J. Am. Ceram. Soc.* **138**, pp. 8928–8935 (2016).

[25] Fu Jing, Hassan Fathy M., Zhong Cheng, Lu Jun, Liu Han, Yu Aiping, and Chen Zhongwei, "Defect engineering of chalcogen-tailored oxygen electrocatalysts for rechargeable quasi-solid-state zinc-air batteries", *Adv. Mater.* **29**, pp. 1702526 (2017).

[26] Kenji Nomura, Hiromichi Ohta, Kazushige Ueda, Toshio Kamiya, Masahiro Hirano, and Hideo Hosono, "Thin-film transistor fabricated in single-crystalline transparent oxide semiconductor", *Science* **300**, pp. 1269–1272 (2003).

[27] K. K. Banger, Y. Yamashita, K. Mori, R. L. Peterson, T. Leedham, J. Rickard, and H. Sirringhaus, "Low-temperature, high-performance solution-processed metal oxide thin-film transistors formed by a 'sol-gel on chip' process", *Nat. Mater.* **10**, pp. 45–50 (2010).

[28] J. M. Caruge, J. E. Halpert, V. Wood, V. Bulovic, and M. G. Bawendi, "Colloidal quantum-dot light-emitting diodes with metal-oxide charge transport layers", *Nat. Photonics* **2**, pp. 247–250 (2008).

[29] Sang-Hee K. Park, Hwang Chi-Sun, Ryu Minki, Yang Shinhyuk, Byun Chunwon, Shin Jaeheon, Lee Jeong-Ik, Lee Kimoon, Oh Min Suk, and Im Seongil, "Transparent and photo-stable ZnO thin-film transistors to drive an active matrix organic-light-emitting-diode display panel", *Adv. Mater.* **21**, pp. 678–682 (2009).

[30] Guangru Li, Zhi-Kuang Tan, Dawei Di, May Ling Lai, Lang Jiang, Jonathan Hua-Wei Lim, Richard H. Friend, and Neil C. Greenham, "Efficient light-emitting diodes based on nanocrystalline perovskite in a dielectric polymer matrix", *Nano Lett.* **15**, pp. 2640–2644 (2015).

[31] R. A. Miller, "Thermal barrier coatings for aircraft engines: history and directions", *J. Therm. Spray Techn.* **6**, pp. 35 (1997).

[32] Robert Vassen, Cao Xueqiang, Tietz Frank, Basu Debabrata, and Stöver Detlev, "Zirconates as new materials for thermal barrier coatings", *J. Am. Ceram. Soc.* **83**, pp. 2023–2028 (2004).

[33] Wu Jie, Wei Xuezheng, Padture Nitin P., Klemens Paul G., Gell Maurice, Garca Eugenio, Miranzo Pilar, and Osendi Maria I., "Low-thermal-conductivity rare-earth zirconates for potential thermal-barrier-coating applications", *J. Am. Ceram. Soc.* **85**, pp. 3031–3035 (2004).

[34] F.S. Galasso, *Structure and Properties of Inorganic Solids*, International Series of Monographs in Solid State Physics e. Pergamon Press (1970).

[35] Akira Fujishima and Kenichi Honda, "Electrochemical photolysis of water at a semiconductor electrode", *Nature* **238**(5358), pp. 37–38 (1972).

[36] Meng Ni, Michael K.H. Leung, Dennis Y.C. Leung, and K. Sumathy, "A review and recent developments in photocatalytic water-splitting using TiO_2 for hydrogen production", *Renew. Sust. Energ. Rev.* **11**(3), pp. 401 – 425 (2007).

[37] Gongming Wang, Hanyu Wang, Yichuan Ling, Yuechao Tang, Xunyu Yang, Robert C. Fitzmorris, Changchun Wang, Jin Z. Zhang, and Yat Li, "Hydrogen-treated TiO_2 nanowire arrays for photoelectrochemical water splitting", *Nano Lett.* **11**, pp. 3026–3033 (2011).

[38] K.-I. Ishibashi, Akira Fujishima, Toshiya Watanabe, and Kazuhito Hashimoto, "Quantum yields of active oxidative species formed on TiO_2 photocatalyst", *J. Photochem. Photobiol., A* **134**, pp. 139 – 142 (2000).

[39] Cathy McCullagh, Jeanette M. C. Robertson, Detlef W. Bahnemann, and Peter K. J. Robertson, "The application of TiO_2 photocatalysis for disinfection of water contaminated with pathogenic micro-organisms: a review", *Res. Chem. Intermed.* **33**, pp. 359–375 (2007).

[40] Yawen Wang, Lizhi Zhang, Kejian Deng, Xinyi Chen, and Zhigang Zou, "Low temperature synthesis and photocatalytic activity of rutile TiO_2 nanorod superstructures", *J. Phys. Chem. C* **111**, pp. 2709–2714 (2007).

[41] Václav Štengl, Vendula Houšková, Snejana Bakardjieva, Nataliya Murafa, and Vladimír Havlín, "Optically transparent titanium dioxide particles incorporated in poly(hydroxyethyl methacrylate) thin layers", *J. Phys. Chem. C* **112**, pp. 19979–19985 (2008).

[42] C. Terrier, J.P. Chatelon, R. Berjoan, and J.A. Roger, "Sb-doped SnO_2 transparent conducting oxide from the sol-gel dip-coating technique", *Thin Solid Films* **263**, pp. 37 – 41 (1995).

[43] W. S. Choi, Suyoun Lee, V. R. Cooper, and H. N. Lee, "Fractionally δ-doped oxide superlattices for higher carrier mobilities", *Nano Lett.* **12**, pp. 4590–4594 (2012).

[44] F. Schoofs, M. Egilmez, T. Fix, J. L. MacManus-Driscoll, and M. G. Blamire, "Tuning the two-dimensional carrier density at $LaAlO_3/SrTiO_3$ interfaces via rare earth doping", *Solid State Commun.* **156**, pp. 35–37 (2013).

[45] Safdar Nazir, Camille Bernal, and Kesong Yang, "Modulated two-dimensional charge-carrier density in $LaTiO_3$layer-doped $LaAlO_3/SrTiO_3$ heterostructure", *ACS Appl. Mater. Interfaces* **7**(9), pp. 5305–5311 (2015).

[46] Thomas Götsch, Wolfgang Wallisch, Michael Stöger-Pollach, Bernhard Klötzer, and Simon Penner, "From zirconia to yttria: Sampling the YSZ phase diagram using sputter-deposited thin films", *AIP Adv.* **6**, pp. 025119 (2016).

[47] David R. Clarke and Simon R. Phillpot, "Thermal barrier coating materials", *Mater. Today* **8**, pp. 22 – 29 (2005).

[48] Susan Manning Meier, Dinesh K. Gupta, and Keith D. Sheffler, "Ceramic thermal barrier coatings for commercial gas turbine engines", *JOM* **43**, pp. 50–53 (1991).

[49] S. M. Meier and D. K. Gupta, "The evolution of thermal barrier coatings in gas turbine engine applications", *J. Eng. Gas. Turb. Power* **116**, pp. 250–257 (1994).

[50] Nitin P. Padture, Maurice Gell, and Eric H. Jordan, "Thermal barrier coatings for gas-turbine engine applications", *Science* **296**, pp. 280–284 (2002).

[51] D.R. Clarke and C.G. Levi, "Materials design for the next generation thermal barrier coatings", *Annu. Rev. Mater. Res.* **33**(1), pp. 383–417 (2003).

[52] Jeffrey W. Fergus, "Zirconia and pyrochlore oxides for thermal barrier coatings in gas turbine engines", *Metall. Mater. Trans. E* **1**, pp. 118–131 (2014).

[53] R. Moos and K. H. Menesklou, W.and Härdtl, "Hall mobility of undoped n-type conducting strontium titanate single crystals between 19 K and 1373 K", *Appl. Phys. A* **61**, pp. 389–395 (1995).

[54] A. Kalabukhov, R. Gunnarsson, J. Börjesson, E. Olsson, T. Claeson, and D. Winkler, "Effect of oxygen vacancies in the $SrTiO_3$ substrate on the electrical properties of the $LaAlO_3/SrTiO_3$ interface", *Phys. Rev. B* **75**, pp. 121404 (2007).

[55] Tor S. Bjørheim, Marco Arrigoni, Denis Gryaznov, Eugene Kotomin, and Joachim Maier, "Thermodynamic properties of neutral and charged oxygen vacancies in $BaZrO_3$ based on first principles phonon calculations", *Phys. Chem. Chem. Phys.* **17**, pp. 20765–20774 (2015).

[56] B. Thangaraju, "Structural and electrical studies on highly conducting spray deposited fluorine and antimony doped SnO_2 thin films from $SnCl_2$ precursor", *Thin Solid Films* **402**, pp. 71–78 (2002).

[57] Yude Wang, Torsten Brezesinski, Markus Antonietti, and Bernd Smarsly, "Ordered mesoporous Sb-, Nb-, and Ta-doped SnO_2 thin films with adjustable doping levels and high electrical conductivity", *ACS Nano* **3**, pp. 1373–1378 (2009).

[58] K.-H. Zum Gahr, W. Bundschuh, and B. Zimmerlin, "Effect of grain size on friction and sliding wear of oxide ceramics", *Wear* **162-164**, pp. 269 – 279 (1993).

[59] S. Raghavan, M.J. Mayo, H. Wang, R.B. Dinwiddie, and W.D. Porter, "The effect of grain size, porosity and yttria content on the thermal conductivity of nanocrystalline zirconia", *Scripta Mater.* **39(8)**, pp. 1119 – 1125 (1998).

[60] A. Tschöpe, E. Sommer, and R. Birringer, "Grain size-dependent electrical conductivity of polycrystalline cerium oxide: I. Experiments", *Solid State Ionics* **139**, pp. 255 – 265 (2001).

[61] CLEVELAND J. J. and BRADT R. C., "Grain size/microcracking relations for pseudo-brookite oxides", *J. Am. Ceram. Soc.* **61**, pp. 478–481 (1978).

[62] Chaonan Xu, Jun Tamaki, Norio Miura, and Noboru Yamazoe, "Grain size effects on gas sensitivity of porous SnO_2-based elements", *Sens. Actuators, B: Chem.* **3**, pp. 147 – 155 (1991).

[63] R. M. Latanision and H. Opperhauser, "The intergranular embrittlement of nickel by hydrogen: The effect of grain boundary segregation", *Metall. Trans.* **5**, pp. 483–492 (1974).

[64] H. Erhart and H. J. Grabke, "Equilibrium segregation of phosphorus at grain boundaries of Fe-P, Fe-C-P, Fe-Cr-P, and Fe-Cr-C-P alloys", *Met. Sci.* **15**, pp. 401–408 (1981).

[65] Masatake Yamaguchi, Motoyuki Shiga, and Hideo Kaburaki, "Grain boundary decohesion by impurity segregation in a nickel-sulfur system", *Science* **307**, pp. 393–397 (2005).

[66] G. S. Painter and F. W. Averill, "Effects of segregation on grain-boundary cohesion: A density-functional cluster model of boron and sulfur in nickel", *Phys. Rev. Lett.* **58**, pp. 234–237 (1987).

[67] J. P. Buban, K. Matsunaga, J. Chen, N. Shibata, W. Y. Ching, T. Yamamoto, and Y. Ikuhara, "Grain boundary strengthening in alumina by rare earth impurities", *Science* **311**, pp. 212–215 (2006).

[68] I. Denk, J. Claus, and J. Maier, "Electrochemical investigations of $SrTiO_3$ boundaries", *J. Electrochem. Soc.* **144**, pp. 3526–3536 (1997).

[69] Rainer Hagenbeck and Rainer Waser, "Influence of temperature and interface charge on the grain-boundary conductivity in acceptor-doped $SrTiO_3$ ceramics", *J. Appl. Phys.* **83**, pp. 2083–2092 (1998).

[70] James A. Dawson and Isao Tanaka, "Local structure and energetics of Pr- and La-doped $SrTiO_3$ grain boundaries and the influence on core-shell structure formation", *J. Phys. Chem. C* **118**, pp. 25765–25778 (2014).

[71] Dario Marrocchelli, Lixin Sun, and Bilge Yildiz, "Dislocations in $SrTiO_3$: Easy to reduce but not so fast for oxygen transport", *J. Am. Chem. Soc.* **137**, pp. 4735–4748 (2015).

[72] Si-Young Choi, Sung-Dae Kim, Minseok Choi, Hak-Sung Lee, Jungho Ryu, Naoya Shibata, Teruyasu Mizoguchi, Eita Tochigi, Takahisa Yamamoto, Suk-Joong L. Kang, and Yuichi Ikuhara, "Assessment of strain-generated oxygen vacancies using $SrTiO_3$ bicrystals", *Nano Lett.* **15**, pp. 4129–4134 (2015).

[73] Stephan P. Waldow and Roger A. De Souza, "Computational study of oxygen diffusion along *a*[100] dislocations in the perovskite oxide $SrTiO_3$", *ACS Appl. Mater. Interfaces* **8**, pp. 12246–12256 (2016).

[74] K.S. Shamala, L.C.S. Murthy, and K. Narasimha Rao, "Studies on tin oxide films prepared by electron beam evaporation and spray pyrolysis methods", *Bull. Mater. Sci.* **27**, pp. 295–301 (2004).

[75] David S. Ginley and Clark Bright, "Transparent conducting oxides", *MRS Bull.* **25**, pp. 15–18 (2000).

[76] H. Kim, C. M. Gilmore, A. Piqué, J. S. Horwitz, H. Mattoussi, H. Murata, Z. H. Kafafi, and D. B. Chrisey, "Electrical, optical, and structural properties of indium-tin-oxide thin films for organic light-emitting devices", *J. Appl. Phys.* **86**, pp. 6451–6461 (1999).

[77] Liang Wang, Dean W. Matson, Evgueni Polikarpov, James S. Swensen, Charles C. Bonham, Lelia Cosimbescu, Joseph J. Berry, David S. Ginley, Daniel J. Gaspar, and Asanga B. Padmaperuma, "Highly efficient blue organic light emitting device using indium-free transparent anode Ga:ZnO with scalability for large area coating", *J. Appl. Phys.* **107**, pp. 043103 (2010).

[78] Tadatsugu Minami, "Transparent conducting oxide semiconductors for transparent electrodes", *Semicond. Sci. Tech.* **20**, pp. S35 (2005).

[79] Yutaka Furubayashi, Taro Hitosugi, Yukio Yamamoto Kazuhisa Inaba, Go Kinoda, Yasushi Hirose, Toshihiro Shimada, and Tetsuya Hasegawa, "A transparent metal: Nb-doped anatase TiO_2", *Appl. Phys. Lett.* **86**, pp. 252101 (2005).

[80] Q. Wan and T. H. Wang, "Comment on A transparent metal: Nb-doped anatase TiO_2 [Appl. Phys. Lett. 86, 252101 (2005)]", *Appl. Phys. Lett.* **88**, pp. 226102 (2006).

[81] Yutaka Furubayashi, Taro Hitosugi, and Tetsuya Hasegawa, "Response to comment on A transparent metal: Nb-doped anatase TiO_2 [Appl. Phys. Lett. 86, 252101 (2005)]", *Appl. Phys. Lett.* **88**, pp. 226103 (2006).

[82] S. X. Zhang, D. C. Kundaliya, W. Yu, S. Dhar, S. Y. Young, L. G. Salamanca-Riba, S. B. Ogale, R. D. Vispute, and T. Venkatesan, "Niobium doped TiO_2: Intrinsic transparent metallic anatase versus highly resistive rutile phase", *J. Appl. Phys.* **102**, pp. 013701 (2007).

[83] A. Roy Barman, M. Motapothula, A. Annadi, K. Gopinadhan, Y. L. Zhao, Z. Yong, I. Santoso, Ariando, M. Breese, A. Rusydi, S. Dhar, and T. Venkatesan, "Multifunctional $Ti_{1-x}Ta_xO_2$: Ta doping or alloying?", *Appl. Phys. Lett.* **98**(7), pp. 072111 (2011).

[84] Kesong Yang, Ying Dai, Baibiao Huang, and Yuan Ping Feng, "First-principles gga+u study of the different conducting properties in pentavalent-ion-doped anatase and rutile TiO_2", *J. Phys. D: Appl. Phys.* **47**, pp. 275101 (2014).

[85] Takenori Yamamoto and Takahisa Ohno, "Screened hybrid density functional study on Nb- and Ta-doped tio_2", *Phys. Rev. B* **85**, pp. 033104 (2012).

[86] Maofeng Dou and Clas Persson, "Comparative study of rutile and anatase SnO_2 and TiO_2: Band-edge structures, dielectric functions, and polaron effects", *J. Appl. Phys.* **113**, pp. 083703 (2013).

[87] A.C. Camargo, J.A. Igualada, A. Beltrán, R. Llusar, E. Longo, and J. Andrés, "An *ab initio* perturbed ion study of structural properties of TiO_2, SnO_2 and GeO_2 rutile lattices", *Chem. Phys.* **212**, pp. 381 – 391 (1996).

[88] Sang woo Lee, Young-Woon Kim, and Haydn Chen, "Electrical properties of Ta-doped SnO_2 thin films prepared by the metalorganic chemical-vapor deposition method", *Appl. Phys. Lett.* **78**, pp. 350–352 (2001).

[89] Shoichiro Nakao, Naoomi Yamada, Yasushi Hirose, and Tetsuya Hasegawa, "Enhanced carrier generation in Nb-doped SnO_2 thin films grown on strain-inducing substrates", *Appl. Phys. Express* **5**, pp. 061201 (2012).

[90] Güven Turgut, Eyüp Fahri Keskenler, Serdar Aydin, Erdal Sönmez, Seydi Doğan, Bahattin Düzgün, and Mehmet Ertuğrul, "Effect of Nb doping on structural, electrical and optical properties of spray deposited SnO_2 thin films", *Superlattice Microst.* **56**, pp. 107 – 116 (2013).

[91] Z. Q. Li, Y. L. Yin, X. D. Liu, L. Y. Li, H. Liu, and Q. G. Song, "Electronic structure and optical properties of Sb-doped SnO_2", *J. Appl. Phys.* **106**, pp. 083701 (2009).

[92] Daojian Cheng, Minming Zhang, Jianfeng Chen, Chenxi Yang, Xiaofei Zeng, and Dapeng Cao, "Computer screening of dopants for the development of new SnO_2-based transparent conducting oxides", *J. Phys. Chem. C* **118**, pp. 2037–2043 (2014).

[93] J. Varley, A. Janotti, and C. Van de Walle, "Group-v impurities in sno_2 from first-principles calculations", *Phys. Rev. B* **81**, pp. 245216 (2010).

[94] Abhishek Kumar Singh, Anderson Janotti, Matthias Scheffler, and Chris G. Van de Walle, "Sources of electrical conductivity in SnO_2", *Phys. Rev. Lett.* **101**, pp. 055502 (2008).

[95] Risto M Nieminen, "Issues in first-principles calculations for defects in semiconductors and oxides", *Model. Simul. Mater. Sci. Eng* **17**, pp. 084001 (2009).

[96] Kalobaran Maiti and Ravi Shankar Singh, "Evidence against strong correlation in 4*d* transition-metal oxides $CaRuO_3$ and $SrRuO_3$", *Phys. Rev. B* **71**, pp. 161102 (2005).

[97] P.E. Blöchl, "Projector augmented-wave method", *Phys. Rev. B* **50**, pp. 17953–17979 (1994).

[98] J. P. Perdew, K. Burke, and M. Ernzerhof, "Generalized gradient approximation made simple", *Phys. Rev. Lett.* **77**, pp. 3865–3868 (1996).

[99] Peter E. Blöchl, O. Jepsen, and O. K. Andersen, "Improved tetrahedron method for Brillouin-zone integrations", *Phys. Rev. B* **49**, pp. 16223–16233 (1994).

[100] M. K. Y. Chan and G. Ceder, "Efficient band gap prediction for solids", *Phys. Rev. Lett.* **105**, pp. 196403 (2010).

[101] Yuhua Duan, "Electronic properties and stabilities of bulk and low-index surfaces of SnO in comparison with SnO_2: A first-principles density functional approach with an empirical correction of van der waals interactions", *Phys. Rev. B* **77**, pp. 045332 (2008).

[102] Jochen Heyd, Gustavo E. Scuseria, and Matthias Ernzerhof, "Hybrid functionals based on a screened Coulomb potential", *Chem. Phys.* **118**, pp. 8207–8215 (2003).

[103] G. Kresse and J. Furthmüller, "Efficiency of *ab-initio* total energy calculations for metals and semiconductors using a plane-wave basis set", *Comput. Mater. Sci.* **6**(1), pp. 15–50 (1996).

[104] G. Kresse and J. Furthmüller, "Efficient iterative schemes for *ab-initio* total-energy calculations using a plane-wave basis set", *Phys. Rev. B* **54**, pp. 11169–11186 (1996).

[105] R. O. Jones and O. Gunnarsson, "The density functional formalism, its applications and prospects", *Rev. Mod. Phys.* **61**, pp. 689–746 (1989).

[106] Thomas M. Henderson, Joachim Paier, and Gustavo E. Scuseria, "Accurate treatment of solids with the HSE screened hybrid", *Phys. Status Solidi B* **248**, pp. 767–774 (2011).

[107] Jochen Heyd, Juan E. Peralta, Gustavo E. Scuseria, and Richard L. Martin, "Energy band gaps and lattice parameters evaluated with the Heyd-Scuseria-Ernzerhof screened hybrid functional", *Chem. Phys.* **123**, pp. 174101 (2005).

[108] J. B. Varley, A. Janotti, A. K. Singh, and C. G. Van de Walle, "Hydrogen interactions with acceptor impurities in SnO_2: First-principles calculations", *Phys. Rev. B* **79**, pp. 245206 (2009).

[109] K. Reimann and M. Steube, "Experimental determination of the electronic band structure of SnO_2", *Solid State Commun.* **105**, pp. 649 – 652 (1998).

[110] Mehmet Aras and Cetin Kılıç, "Combined hybrid functional and dft+u calculations for metal chalcogenides", *J. Chem. Phys.* **141**, pp. 044106 (2014).

[111] Matthias Batzill and Ulrike Diebold, "The surface and materials science of tin oxide", **79**, pp. 47 – 154 (2005).

[112] F.J. Arlinghaus, "Energy bands in stannic oxide (SnO_2)", *J. Phys. Chem. Solids* **35**, pp. 931 – 935 (1974).

[113] K. C. Mishra, K. H. Johnson, and P. C. Schmidt, "Electronic structure of antimony-doped tin oxide", *Phys. Rev. B* **51**, pp. 13972–13976 (1995).

[114] V.M. Zainullina, "Electronic structure, chemical bonding and properties of $Sn_{1-x}M_xO_2$, M=As, Sb, Bi, V, Nb, Ta ($0.0 \leq x \leq 0.25$)", *Physica B* **391**, pp. 280 – 285 (2007).

[115] A. Schleife, J. Varley, F. Fuchs, C. Rödl, F. Bechstedt, P. Rinke, A. Janotti, and C. Van de Walle, "Tin dioxide from first principles: Quasiparticle electronic states and optical properties", *Phys. Rev. B* **83**, pp. 035116 (2011).

[116] B. A. Hamad, "First-principle calculations of structural and electronic properties of rutile-phase dioxides (mo_2), m = ti, v, ru, ir and sn", *Eur. Phys. J. B* **70**, pp. 163–169 (2009).

[117] Elias Burstein, "Anomalous optical absorption limit in InSb", *Phys. Rev.* **93**, pp. 632–633 (1954).

[118] T. S. Moss, "The interpretation of the properties of Indium Antimonide", *Proc. Phys. Soc. B* **67**, pp. 775–782 (1954).

[119] Jaehyeong Lee, "Effects of oxygen concentration on the properties of sputtered SnO_2:Sb films deposited at low temperature", *Thin Solid Films* **516**, pp. 1386 – 1390 (2008).

[120] J. Arbiol, J. Cerdà, G. Dezanneau, A. Cirera, F. Peiró, A. Cornet, and J. R. Morante, "XPS and XANES study of $Ti_{1-x}Nb_xO_2$ nanopowders for gas sensing applications.", *J. Appl. Phys.* **92**, pp. 853 (2002).

[121] Hassan Raza, *Graphene Nanoelectronics: Metrology, Synthesis, Properties and Applications*, Springer Science & Business Media (2012).

[122] Michael O'Keeffe, *Structure and Bonding in crystals, Volume 1*, Elsevier (2012).

[123] Lu Peng-Fei, Shen Yue, Yu Zhong-Yuan, Zhao Long, Li Qiong-Yao, Ma Shi-Jia, Han Li-Hong, and Liu Yu-Min, "Electronic structure and optical properties of antimony-doped sno_2 from first-principle study", *Commun. Theor. Phys.* **57**, pp. 145 (2012).

[124] Abdullah M. Al-Hamdi, Mika Sillanpää, and Joydeep Dutta, "Photocatalytic degradation of phenol by iodine doped tin oxide nanoparticles under uv and sunlight irradiation", *J. Alloys Compound.* **618**, pp. 366 – 371 (2015).

[125] Peter Gerhardinger and Dr. David Strickler, "Fluorine doped tin oxide coatings—over 50 years and going strong", *Key Eng. Mater.* **380**, pp. 169 – 178 (2008).

[126] Yong Jun Seo, Geun Woo Kim, Chang Hoon Sung, M.S. Anwar, Chan Gyu Lee, and Bon Heun Koo, "Characterization of transparent and conductive electrodes of Nb-doped SnO_2 thin film by pulsed laser deposition", **11**, pp. S310 – S313 (2011).

[127] Shihui Yu, Linghong Ding, Chuang Xue, Li Chen, and W.F. Zhang, "Transparent conducting Sb-doped SnO_2 thin films grown by pulsed laser deposition", *J. Non-Cryst. Solids* **358**, pp. 3137 – 3140 (2012).

[128] Wenhao Yang, Shihui Yu, Yang Zhang, and Weifeng Zhang, "Properties of Sb-doped SnO_2 transparent conductive thin films deposited by radio-frequency magnetron sputtering", *Thin Solid Films* **542**, pp. 285 – 288 (2013).

[129] David R. Lide, *CRC Handbook of Chemistry and Physics (90th ed.)*, CRC Press (2009).

[130] Kesong Yang, Ying Dai, Baibiao Huang, and Myung-Hwan Whangbo, "Density functional characterization of the band edges, the band gap states, and the preferred doping sites of halogen-doped TiO_2", *Chem. Mater.* **20**, pp. 6528–6534 (2008).

[131] J. A. Bert, B. Kalisky, C. Bell, M. Kim, Y. Hikita, H. Y. Hwang, and K. A. Moler, "Direct imaging of the coexistence of ferromagnetism and superconductivity at the $LaAlO_3/SrTiO_3$ interface", *Nat. Phys.* **7**, pp. 767–771 (2011).

[132] L. Li, C. Richter, J. Mannhart, and R. C. Ashoori, "Coexistence of magnetic order and two-dimensional superconductivity at $LaAlO_3/SrTiO_3$ interfaces", *Nat. Phys.* **7**, pp. 762–766 (2011).

[133] J. S. Lee, Y. W. Xie, H. K. Sato, C. Bell, Y. Hikita, H. Y. Hwang, and C. C. Kao, "Titanium d_{xy} ferromagnetism at the $LaAlO_3/SrTiO_3$ interface", *Nat. Mater.* **12**, pp. 703–706 (2013).

[134] S. Frank, A. C. Michael, E. V. Mary, E. Mehmet, F. Thomas, E. K. Josee, J. L. McManus-Driscoll, and G. B. Mark, "Carrier density modulation by structural distortions at modified $LaAlO_3/SrTiO_3$ interfaces", *J. Phys.: Condens. Matter* **25**, pp. 175005 (2013).

[135] T. Fix, J. L. MacManus-Driscoll, and M. G. Blamire, "Delta-Doped $LaAlO_3/SrTiO_3$ interfaces", *Appl. Phys. Lett.* **94**, pp. 172101 (2009).

[136] T. Fix, F. Schoofs, J. L. MacManus-Driscoll, and M. G. Blamire, "Influence of doping at the nanoscale at $LaAlO_3/SrTiO_3$ interfaces", *Appl. Phys. Lett.* **97**, pp. 072110 (2010).

[137] A. S. Disa, D. P. Kumah, A. Malashevich, H. Chen, D. A. Arena, E. D. Specht, S. Ismail-Beigi, F. J. Walker, and C. H. Ahn, "Orbital engineering in symmetry-breaking polar heterostructures", *Phys. Rev. Lett.* **114**, pp. 026801 (2015).

[138] A. Ohtomo and H. Y. Hwang, "A high-mobility electron gas at the $LaAlO_3/SrTiO_3$ heterointerface", *Nature* **427**, pp. 423–426 (2004).

[139] D. A. Dikin, M. Mehta, C. W., C. M. Folkman, C. B. Eom, and V. Chandrasekhar, "Coexistence of superconductivity and ferromagnetism in two dimensions", *Phys. Rev. Lett.* **107**, pp. 056802 (2011).

[140] B. Kalisky, J. A. Bert, B. B. Klopfer, C. Bell, H. K. Sato, M. Hosoda, Y. Hikita, H. Y. Hwang, and K. A. Moler, "Critical thickness for ferromagnetism in $LaAlO_3/SrTiO_3$ heterostructures", *Nat. Commun.* **3**, pp. 922 (2012).

[141] A. Brinkman, M. Huijben, M. van Zalk, J. Huijben, U. Zeitler, J. C. Maan, W. G. van der Wiel, G. Rijnders, D. H. A. Blank, and H. Hilgenkamp, "Magnetic effects at the interface between non-magnetic oxides", *Nat. Mater.* **6**, pp. 493–496 (2007).

[142] G. Herranz, M. Basletić, M. Bibes, C. Carrétéro, E. Tafra, E. Jacquet, K. Bouzehouane, C. Deranlot, A. Hamzi, J.-M. Broto, A. Barthélémy, and A. Fert, "High mobility in $LaAlO_3/SrTiO_3$ heterostructures: Origin, dimensionality, and perspectives", *Phys. Rev. Lett.* **98**, pp. 216803 (2007).

[143] S. Thiel, G. Hammerl, A. Schmehl, C. W. Schneider, and J. Mannhart, "Tunable quasi-two-dimensional electron gases in oxide heterostructures", *Science* **313**, pp. 1942–1945 (2006).

[144] A. D. Caviglia, S. Gariglio, N. Reyren, D. Jaccard, T. Schneider, M. Gabay, S. Thiel, G. Hammerl, J. Mannhart, and J. M. Triscone, "Electric field control of the $LaAlO_3/SrTiO_3$ interface ground state", *Nature* **456**, pp. 624–627 (2008).

[145] C. Cen, S. Thiel, G. Hammerl, C. W. Schneider, K. E. Andersen, C. S. Hellberg, J. Mannhart, and J. Levy, "Nanoscale control of an interfacial metal-insulator transition at room temperature", *Nat. Mater.* **7**, pp. 298–302 (2008).

[146] N. Pavlenko, T. Kopp, E. Y. Tsymbal, G. A. Sawatzky, and J. Mannhart, "Magnetic and superconducting phases at the $LaAlO_3/SrTiO_3$ interface: The role of interfacial ti $3d$ electrons", *Phys. Rev. B* **85**, pp. 020407 (2012).

[147] M. Salluzzo, S. Gariglio, D. Stornaiuolo, V. Sessi, S. Rusponi, C. Piamonteze, G. M. De Luca, M. Minola, D. Marré, A. Gadaleta, H. Brune, F. Nolting, N. B. Brookes, and G. Ghiringhelli, "Origin of interface magnetism in $BiMnO_3/SrTiO_3$ and $LaAlO_3/SrTiO_3$ heterostructures", *Phys. Rev. Lett.* **111**, pp. 087204 (2013).

[148] Liping Yu and Alex Zunger, "A polarity-induced defect mechanism for conductivity and magnetism at polar−nonpolar oxide interfaces", *Nat. Commun.* **5**, pp. 5118 (2014).

[149] Z. Liu, C. Li, W. Lü, X. Huang, Z. Huang, S. Zeng, X. Qiu, L. Huang, A. Annadi, J. Chen, J. Coey, T. Venkatesan, and Ariando, "Origin of the two-dimensional electron gas at $LaAlO_3/SrTiO_3$ interfaces: The role of oxygen vacancies and electronic reconstruction", *Phys. Rev. X* **3**, pp. 021010 (2013).

[150] N. Nakagawa, H. Y. Hwang, and D. A. Muller, "Why some interfaces cannot be sharp", *Nat. Mater.* **5**, pp. 204–209 (2006).

[151] L. Qiao, T. C. Droubay, V. Shutthanandan, Z. Zhu, P. V. Sushko, and S. A. Chambers, "Thermodynamic instability at the stoichiometric $LaAlO_3/SrTiO_3$ (001) interface", *J. Phys.: Condens. Matter* **22**, pp. 312201 (2010).

[152] Safdar Nazir, Maziar Behtash, and Kesong Yang, "Enhancing interfacial conductivity and spatial charge confinement of $LaAlO_3/SrTiO_3$ heterostructures via strain engineering", *Appl. Phys. Lett.* **105**, pp. 141602 (2014).

[153] C. W. Bark, D. A. Felker, Y. Wang, Y. Zhang, H. W. Jang, C. M. Folkman, J. W. Park, S. H. Baek, H. Zhou, D. D. Fong, X. Q. Pan, E. Y. Tsymbal, M. S. Rzchowski, and C. B. Eom, "Tailoring a two-dimensional electron gas at the $LaAlO_3/SrTiO_3$ (001) interface by epitaxial strain", *Proc. Natl. Acad. Sci. U.S.A.* **108**, pp. 4720–4724 (2011).

[154] Masayuki Hosoda, Christopher Bell, Yasuyuki Hikita, and H. Y Hwang, "Compositional and gate tuning of the interfacial conductivity in $LaAlO_3/LaTiO_3/SrTiO_3$ heterostructures", *Appl. Phys. Lett.* **102**, pp. 091601 (2013).

[155] B. Kalisky, E. M. Spanton, H. Noad, J. R. Kirtley, K. C. Nowack, C. Bell, H. K. Sato, M. Hosoda, Y. Xie, Y. Hikita, C. Woltmann, G. Pfanzelt, R. Jany, C. Richter, H. Y. Hwang, J. Mannhart, and K. A. Moler, "Locally enhanced conductivity due to the tetragonal domain structure in $LaAlO_3/SrTiO_3$ heterointerfaces", *Nat. Mater.* **12**, pp. 1091–1095 (2013).

[156] T. Yajima, Y. Hikita, and H. Y. Hwang, "A heteroepitaxial perovskite Metal-Base transistor", *Nat. Mater.* **10**, pp. 198–201 (2011).

[157] N. Reyren, S. Thiel, A. D. Caviglia, L. F. Kourkoutis, G. Hammer, C. Richter, C. W. Schneider, T. Kopp, A. S. Rüetschi, D. Jaccard, M. Gabay, D. A. Muller, J. M. Triscone, and J. Mannhart, "Superconducting interfaces between insulating oxides", *Science* **317**, pp. 1196–1199 (2007).

[158] A. Rastogi, A. K. Kushwaha, T. Shiyani, A. Gangawar, and R. C. Budhani, "Electrically tunable optical switching of a mott insulator-band insulator interface", *Adv. Mater.* **22**, pp. 4448–4451 (2010).

[159] A. Rastogi, J. J. Pulikkotil, and R. C. Budhani, "Enhanced persistent photoconductivity in δ-Doped $LaAlO_3/SrTiO_3$ heterostructures", *Phys. Rev. B* **89**, pp. 125127 (2014).

[160] Safdar Nazir and Kesong Yang, "First-principles characterization of the critical thickness for forming metallic states in strained $LaAlO_3/SrTiO_3$(001) heterostructure", *ACS Appl. Mater. Interfaces* **6**, pp. 22351–22358 (2014).

[161] Safdar Nazir, Maziar Behtash, and Kesong Yang, "The role of uniaxial strain in tailoring the interfacial properties of $LaAlO_3/SrTiO_3(001)$ heterostructure", *RSC Adv.,* **5**, pp. 15682–15689 (2015).

[162] Safdar Nazir, Jianli Cheng, Maziar Behtash, Jian Luo, and Kesong Yang, "Interface energetics and charge carrier density amplification by Sn-doping in $LaAlO_3/SrTiO_3$ heterostructure", *ACS Appl. Mater. Inter.* **7**(26), pp. 14294–14302 (2015).

[163] Safdar Nazir, Camille Berna, and Kesong Yang, "Modulated two-dimensional charge carrier density in $LaTiO_3$-layer-doped $LaAlO_3/SrTiO_3$ heterostructure", *ACS Appl. Mater. Interfaces* **7**, pp. 5305–5311 (2015).

[164] Y. Z. Chen, F. Trier, T. Wijnands, R. J. Green, N. Gauquelin, R. Egoavil, D. V. Christensen, G. Koster, M. Huijben, N. Bovet, S. Macke, F. He, R. Sutarto, N. H. Andersen, J. A. Sulpizio, M. Honig, G. E. D. K. Prawiroatmodjo, T. S. Jespersen, S. Linderoth, S. Ilani, J. Verbeeck, G. Van Tendeloo, G. Rijnders, G. A. Sawatzky, and N. Pryds, "Extreme mobility enhancement of two-dimensional electron gases at oxide interfaces by charge-transfer-induced modulation doping", *Nat. Mater.* **14**, pp. 801–806 (2015).

[165] Jianli Cheng, Yaqin Wang, and Kesong Yang, "Tuning the electron mobility of two-dimensional electron gas at the $LaAlO_3/SrTiO_3$ interface through transition-metal doping: First-principles design", *In Preparation* (2015).

[166] Kesong Yang, Ying Dai, Baibiao Huang, and Yuan Ping Feng, "First-principles GGA+U study of the different conducting properties in Pentavalent-Ion-Doped anatase and rutile TiO_2", *J. Phys. D: Appl. Phys.* **47**, pp. 275101 (2014).

[167] G. Kresse and J. Furthmüller, "Efficient iterative schemes for *ab initio* total-energy calculations using a plane-wave basis set", *Phys. Rev. B* **54**, pp. 11169–11186 (1996).

[168] Vladimir I. Anisimov, Jan Zaanen, and Ole K. Andersen, "Band theory and Mott insulators: Hubbard U instead of stoner I", *Phys. Rev. B* **44**(3), pp. 943–954 (1991).

[169] Kesong Yang, Ying Dai, Baibiao Huang, and Yuan Ping Feng, "Density functional characterization of the antiferromagnetism in Oxygen-Deficient anatase and rutile TiO_2", *Phys. Rev. B* **81**, pp. 033202 (2010).

[170] R. Pentcheva and W. E. Pickett, "Ionic relaxation contribution to the electronic reconstruction at the n-type $LaAlO_3/SrTiO_3$ interface", *Phys. Rev. B* **78**, pp. 205106 (2008).

[171] R. Arras, V. G. Ruiz, W. E. Pickett, and R. Pentcheva, "Tuning the two-dimensional electron gas at the $LaAlO_3/SrTiO_3(001)$ interface by metallic contacts", *Phys. Rev. B* **85**, pp. 125404 (2012).

[172] Y. S. Lee, S. J. Moon, Scott C. Riggs, M. C. Shapiro, I. R. Fisher, Bradford W. Fulfer, Julia Y. Chan, A. F. Kemper, and D. N. Basov, "Infrared study of the electronic structure of the metallic pyrochlore iridate $bi_2ir_2o_7$", *Phys. Rev. B* **87**, pp. 195143 (2013).

[173] B. G. Janesko, T. M. Henderson, and G. E. Scuseria, "Screened hybrid density functionals for Solid-State chemistry and physics", *J. Phys.: Condens. Matter* **11**, pp. 443–454 (2009).

[174] Fedwa El-Mellouhi, E. N. Brothers, M. J. Lucero, and G. E. Scuseria, "Modeling of the cubic and antiferrodistortive phases of $SrTiO_3$ with screened hybrid density functional theory", *Phys. Rev. B* **84**, pp. 115122 (2011).

[175] Fedwa El-Mellouhi, E. N. Brothers, M. J. Lucero, I. W. Bulik, and G. E. Scuseria, "Structural phase transitions of the metal oxide perovskites $SrTiO_3$, $LaAlO_3$, and $LaTiO_3$ studied with a screened hybrid functional", *Phys. Rev. B* **87**, pp. 035107 (2013).

[176] C. Franchini, "Hybrid functionals applied to perovskites", *J. Phys.: Condens. Matter* **26**, pp. 253202 (2014).

[177] F. Cossu, U. Schwingenschlögl, and V. Eyert, "Metal-insulator transition at the $LaAlO_3/SrTiO_3$ interface revisited: A hybrid functional study", *Phys. Rev. B* **88**, pp. 045119 (2013).

[178] H. W. Jang, D. A. Felker, C. W. Bark, Y. Wang, M. K. Niranjan, C. T. Nelson, Y. Zhang, D. Su, C. M. Folkman, S. H. Baek, S. Lee, K. Janicka, Y. Zhu, X. Q. Pan, D. D. Fong, E. Y. Tsymbal, M. S. Rzchowski, and C. B. Eom, "Metallic and insulating oxide interfaces controlled by electronic correlations", *Science* **331**, pp. 886–889 (2011).

[179] D. R. Hamann, D. A. Muller, and H. Y. Hwang, "Lattice-polarization effects on electron-gas charge densities in ionic superlattices", *Phys. Rev. B* **73**, pp. 195403 (2006).

[180] S. Okamoto, A. J. Millis, and N. A. Spaldin, "Lattice relaxation in oxide heterostructures: $LaTiO_3/SrTiO_3$ superlattices", *Phys. Rev. Lett.* **97**, pp. 056802 (2006).

[181] R. Pentcheva and W. E. Pickett, "Avoiding the polarization catastrophe in $LaAlO_3$ overlayers on $SrTiO_3$(001) through polar distortion", *Phys. Rev. Lett.* **102**, pp. 107602 (2009).

[182] S. V. Dudiy and B. I. Lundqvist, "First-principles density-functional study of metal-carbonitride interface adhesion: Co/TiC(001) and Co/TiN(001)", *Phys. Rev. B* **64**, pp. 045403 (2001).

[183] N. C. Bristowe, Emilio Artacho, and P. B. Littlewood, "Oxide superlattices with alternating *p* and *n* interfaces", *Phys. Rev. B* **80**, pp. 045425 (2009).

[184] P. Delugas, A. Filippetti, V. Fiorentini, D. I. Bilc, D. Fontaine, and P. Ghosez, "Spontaneous 2-dimensional carrier confinement at the *n*-type $SrTiO_3/LaAlO_3$ interface", *Phys. Rev. Lett.* **106**, pp. 166807 (2011).

[185] C. Cancellieri, M. L. Reinle-Schmitt, M. Kobayashi, V. N. Strocov, P. R. Willmott, D. Fontaine, Ph. Ghosez, A. Filippetti, P. Delugas, and V. Fiorentini, "Doping-dependent band structure of $laalo_3/srtio_3$ interfaces by soft x-ray polarization-controlled resonant angle-resolved photoemission", *Phys. Rev. B* **89**, pp. 121412 (2014).

[186] Safdar Nazir, Maziar Behtash, and Kesong Yang, "Towards enhancing two-dimensional electron gas quantum confinement effects in perovskite oxide heterostructures", *J. Appl. Phys.* **117**, pp. 115305 (2015).

[187] Karolina Janicka, J. P. Velev, and E. Y. Tsymbal, "Magnetism of $LaAlO_3/SrTiO_3$ superlattices", *J. Appl. Phys.* **103**, pp. 07B508 (2008).

[188] M. Salluzzo, J. C. Cezar, N. B. Brookes, V. Bisogni, G. M. De Luca, C. Richter, S. Thiel, J. Mannhart, M. Huijben, A. Brinkman, G. Rijnders, and G. Ghiringhelli, "Orbital reconstruction and the two-dimensional electron gas at the $LaAlO_3/SrTiO_3$ interface", *Phys. Rev. Lett.* **102**, pp. 166804 (2009).

[189] J. H. You and J. H. Lee, "Critical thickness for the two-dimensional electron gas in $LaTiO_3/SrTiO_3$ superlattices", *Phys. Rev. B* **88**, pp. 155111 (2013).

[190] C. W. Bark, D. A. Felker, Y. Wang, Y. Zhang, H. W. Jang, C. M. Folkman, J. W. Park, S. H. Baek, H. Zhou, D. D. Fong, X. Q. Pan, E. Y. Tsymbal, M. S. Rzchowski, and C. B. Eom, "Tailoring a two-dimensional electron gas at the $LaAlO_3/SrTiO_3$ (001) interface by epitaxial strain", *Proc. Natl. Acad. Sci.* **108**, pp. 4720–4724 (2011).

[191] R. Pentcheva and W. E. Pickett, "Avoiding the polarization catastrophe in $LaAlO_3$ overlayers on $SrTiO_3$(001) through polar distortion", *Phys. Rev. Lett.* **102**, pp. 107602 (2009).

[192] B. Kalisky, E. M. Spanton, H. Noad, J. R. Kirtley, K. C. Nowack, C. Bell, H. K. Sato, M. Hosoda, Y. Xie, Y. Hikita, C. Woltmann, G. Pfanzelt, R. Jany, C. Richter, H. Y. Hwang, J. Mannhart, and K. A. Moler, "Locally enhanced conductivity due to the tetragonal domain structure in $LaAlO_3/SrTiO_3$ heterointerfaces", *Nat. Mater.* **12**, pp. 1091–1095 (2013).

[193] C. Cen, S. Thiel, G. Hammerl, C. W. Schneider, K. E. Andersen, C. S. Hellberg, J. Mannhart, and J. Levy, "Nanoscale control of an interfacial metal−insulator transition at room temperature", *Nat. Mater.* **7**, pp. 298 (2008).

[194] C. Cen, S. Thiel, J. Mannhart, and J. Levy, "Oxide nanoelectronics on demand", *Science* **323**, pp. 1026–1030 (2009).

[195] D. Stornaiuolo, S. Gariglio, A. Fête, M. Gabay, D. Li, D. Massarotti, and J.-M. Triscone, "Weak localization and spin-orbit interaction in side-gate field effect devices at the $LaAlO_3/SrTiO_3$ interface", *Phys. Rev. B* **90**, pp. 235426 (2014).

[196] M. Huijben, G. Rijnders, D. H. A. Blank, S. Bals, S. V. Aert, J. Verbeeck, G. V. Tendeloo, A. Brinkman, and H. Hilgenkamp, "Electronically coupled complementary interfaces between perovskite band insulators", *Nat. Mater.* **5**, pp. 556–560 (2006).

[197] Wolter Siemons, Gertjan Koster, Hideki Yamamoto, Walter A. Harrison, Gerald Lucovsky, Theodore H. Geballe, Dave H. A. Blank, and Malcolm R. Beasley, "Origin of charge

density at $LaAlO_3$ on $SrTiO_3$ heterointerfaces: Possibility of intrinsic doping", *Phys. Rev. Lett.* **98**, pp. 196802 (2007).

[198] A. Annadi, A. Putra, Z. Q. Liu, X. Wang, K. Gopinadhan, Z. Huang, S. Dhar, T. Venkatesan, and Ariando, "Electronic correlation and strain effects at the interfaces between polar and nonpolar complex oxides", *Phys. Rev. B* **86**, pp. 085450 (2012).

[199] Liping Yu and Alex Zunger, "A polarity-induced defect mechanism for conductivity and magnetism at polar-nonpolar oxide interfaces", *Nat Commun* **5**, pp. 5118 (2014).

[200] K. Krishnaswamy, C. E. Dreyer, A. Janotti, and C. G. Van de Walle, "First-principles study of surface charging in laalo$_3$/srtio$_3$ heterostructures", *Phys. Rev. B* **92**, pp. 085420 (2015).

[201] Zoran S. Popović, Sashi Satpathy, and Richard M. Martin, "Origin of the two-dimensional electron gas carrier density at the $LaAlO_3$ on $SrTiO_3$ interface", *Phys. Rev. Lett.* **101**, pp. 256801 (2008).

[202] H. Chen, A. M. Kolpak, and Sohrab Ismail-Beigi, "Electronic and magnetic properties of $SrTiO_3$/$LaAlO_3$ interfaces from first principles", *Adv. Mater.* **22**, pp. 2881–2899 (2010).

[203] Yun Li and Jaejun Yu, "Polarization screening and induced carrier density at the interface of $LaAlO_3$ overlayer on $SrTiO_3$ (001)", *J. Appl. Phys.* **108**, pp. 013701 (2010).

[204] Safdar Nazir, Jianli Cheng, Maziar Behtash, Jian Luo, and Kesong Yang, "Interface energetics and charge carrier density amplification by Sn-doping in $LaAlO_3$/$SrTiO_3$ heterostructure", *ACS Appl. Mater. Interfaces* **7**(26), pp. 14294–14302 (2015).

[205] Safdar Nazir, Maziar Behtash, and Kesong Yang, "Enhancing interfacial conductivity and spatial charge confinement of $LaAlO_3$/$SrTiO_3$ heterostructures via strain engineering", *Appl. Phys. Lett.* **105**, pp. 141602 (2014).

[206] Safdar Nazir, Maziar Behtash, and Kesong Yang, "The role of uniaxial strain in tailoring the interfacial properties of $LaAlO_3$/$SrTiO_3$ heterostructure", *RSC Adv.* **5**, pp. 15682–15689 (2015).

[207] Safdar Nazir and Kesong Yang, "First-principles characterization of the critical thickness for forming metallic states in strained $LaAlO_3$/$SrTiO_3$(001) heterostructure", *ACS Appl. Mater. Interfaces* **6**, pp. 22351–22358 (2014).

[208] J. Seidel, L. W. Martin, Q. He, Q. Zhan, Y.-H. Chu, A. Rother, M. E. Hawkridge, P. Maksymovych, P. Yu, M. Gajek, N. Balke, S. V. Kalinin, S. Gemming, F. Wang, G. Catalan, J. F. Scott, N. A. Spaldinand J. Orenstein, and R. Ramesh, "Conduction at domain walls in oxide multiferroics", *Nat. Mater.* **8**, pp. 229–234 (2009).

[209] Jill Guyonnet, Iaroslav Gaponenko, Stefano Gariglio, and Patrycja Paruch, "Conduction at domain walls in insulating pb($zr_{0.2}ti_{0.8}$)o_3 thin films", *Adv. Mater.* **23**, pp. 5377–5382 (2011).

[210] Safdar Nazir, Jianli Cheng, and Kesong Yang, "Creating two-dimensional electron gas in nonpolar oxide interface via polarization discontinuity: First-principles analysis of $CaZrO_3/SrTiO_3$ heterostructure", *ACS Appl. Mater. Interfaces* **8**, pp. 390–399 (2016).

[211] Rémi Arras, Victor G. Ruiz, Warren E. Pickett, and Rossitza Pentcheva, "Tuning the two-dimensional electron gas at the $LaAlO_3/SrTiO_3(001)$ interface by metallic contacts", *Phys. Rev. B* **85**, pp. 125404 (2012).

[212] Rossitza Pentcheva and Warren E. Pickett, "Ionic relaxation contribution to the electronic reconstruction at the $n-type\ LaAlO_3/SrTiO_3$ interface", *Phys. Rev. B* **78**, pp. 205106 (2008).

[213] W. Zhong, R. D. King-Smith, and David Vanderbilt, "Giant LO-TO splittings in perovskite ferroelectrics", *Phys. Rev. Lett.* **72**, pp. 3618–3621 (1994).

[214] Xiaohui Liu, Yong Wang, Pavel V. Lukashev, J. D. Burton, and E. Y. Tsymbal, "Interface dipole effect on thin film ferroelectric stability: First-principles and phenomenological modeling", *Phys. Rev. B* **85**, pp. 125407 (2012).

[215] F. Cossu, U. Schwingenschlögl, and V. Eyert, "Metal-insulator transition at the $LaAlO_3/SrTiO_3$ interface revisited: A hybrid functional study", *Phys. Rev. B* **88**, pp. 045119 (2013).

[216] Won-joon Son, Eunae Cho, Bora Lee, Jaichan Lee, and Seungwu Han, "Density and spatial distribution of charge carriers in the intrinsic *n*-type $laalo_3$-$srtio_3$ interface", *Phys. Rev. B* **79**, pp. 245411 (2009).

[217] Won joon Son, Eunae Cho, Jaichan Lee, and Seungwu Han, "Hydrogen adsorption and carrier generation in $LaAlO_3-SrTiO_3$ heterointerfaces: A first-principles study", *J. Phys.: Condens. Matter* **22**, pp. 315501 (2010).

[218] E. Lesne, N. Reyren, D. Doennig, R. Mattana, H. Jaffrés, F. Petroff V. Cros, F . Choueikani, P. Ohresser, R. Pentcheva, A. Barthélémy, and M. Bibes, "Suppression of the critical thickness threshold for conductivity at the $LaAlO_3/SrTiO_3$ interface", *Nat. Commun.* **5**, pp. 4291 (2012).

[219] Y. U. Peter and Manuel Cardona, *Fundamentals of Semiconductors: Physics and Materials Properties*, Springer Science & Business Media (2010).

[220] Jianying Li, Shengtao Li, Fuyi Liu, M. A. Alim, and G. Chen, "The origin of varistor property of $SrTiO_3$-based ceramics", *J. Mater. Sci.: Materials in Electronics* **14**, pp. 483–486 (2003).

[221] Ying Luo, Xinyu Liu, Xvqiong Li, and Guohua Chen, "$BaBiO_3$-doped $SrTiO_3$-based NTC thermistors", *J. Alloy Compd.* **433**, pp. 221–224 (2007).

[222] K. Eisenbeiser, J. M. Finder, Z. Yu, J. Ramdani, J. A. Curless, J. A. Hallmark, R. Droopad, W. J. Ooms, L. Salem, S. Bradshaw, and C. D. Overgaard, "Field effect transistors with $SrTiO_3$ gate dielectric on si", *Appl. Phys. Lett.* **76**, pp. 1324–1326 (2000).

[223] M. Janousch, G.I. Meijer, U. Staub, B. Delley, S.F. Karg, and B.P. Andreasson, "Role of oxygen vacancies in Cr-doped $SrTiO_3$ for resistance-change memory", *Adv. Mater.* **19**, pp. 2232–2235 (2007).

[224] W. Jiang, M. Noman, Y. M. Lu, J. A. Bain, P. A Salvador, and M. Skowronski, "Mobility of oxygen vacancy in $SrTiO_3$ and its implications for oxygen-migration-based resistance switching", *J. Appl. Phys.* **110**, pp. 034509 (2011).

[225] R. F. Klie and N. D. Browning, "Atomic scale characterization of oxygen vacancy segregation at $SrTiO_3$ grain boundaries", *Appl. Phys. Lett.* **77**, pp. 3737–3739 (2000).

[226] Miyoung Kim, Gerd Duscher, Nigel D. Browning, Karl Sohlberg, Sokrates T. Pantelides, and Stephen J. Pennycook, "Nonstoichiometry and the electrical activity of grain boundaries in $SrTiO_3$", *Phys. Rev. Lett.* **86**, pp. 4056–4059 (2001).

[227] Kesong Yang, Safdar Nazir, Maziar Behtash, and Jianli Cheng, "High-throughput design of two-dimensional electron gas systems based on polar/nonpolar perovskite oxide heterostructures", *Sci. Rep.* **6**, pp. 34667 (2016).

[228] Maziar Behtash, Safdar Nazir, Yaqin Wang, and Kesong Yang, "Polarization effects on the interfacial conductivity in the $LaAlO_3/SrTiO_3$ heterostructure: First-principles study", *Phys. Chem. Chem. Phys.* **18**, pp. 6831–6838 (2016).

[229] Safdar Nazir, Jianli Cheng, and Kesong Yang, "Creating two-dimensional electron gas in nonpolar/nonpolar oxide interface via polarization discontinuity: First-principles analysis of $CaZrO_3/SrTiO_3$ heterostructure", *ACS Appl. Mater. Interfaces* **8**, pp. 390–399 (2016).

[230] Yaqin Wang, Wu Tang, Jianli Cheng, Maziar Behtash, and Kesong Yang, "Creating two-dimensional electron gas in polar/polar perovskite oxide heterostructures: First-principles characterization of $LaAlO_3/A^{+}B^{5+}O_3$", *ACS Appl. Mater. Interfaces* **8**, pp. 13659–13668 (2016).

[231] Ryoko Konta, Tatsuya Ishii, Hideki Kato, and Akihiko Kudo, "Photocatalytic activities of noble metal ion doped $SrTiO_3$ under visible light irradiation", *J. Phys. Chem. B* **108**(26), pp. 8992–8995 (2004).

[232] Yet-Ming Chiang and Touichi Takagi, "Grain-boundary chemistry of barium titanate and strontium titanate: I, high-temperature equilibrium space charge", *J. Am. Ceram. Soc.* **73**, pp. 3278–3285 (1990).

[233] V. Ravikumar and Vinayak P. Dravid, "Atomic structure of undoped $\Sigma = 5$ symmetrical tilt grain boundary in strontium titanate", *Ultramicroscopy* **52**, pp. 557–563 (1993).

[234] Oliver Kienzle and Frank Ernst, "Effect of shear stress on the atomistic structure of a grain boundary in strontium titanate", *J. Am. Ceram. Soc.* **80**, pp. 1639–1644 (1997).

[235] Roger A. De Souza, Jrgen Fleig, Joachim Maier, Oliver Kienzle, Zaoli Zhang, Wilfried Sigle, and Manfred Rhle, "Electrical and structural characterization of a low-angle tilt grain boundary in iron-doped strontium titanate", *J. Am. Ceram. Soc.* **86**, pp. 922–928 (2003).

[236] R Astala and P D Bristowe, "Ab initio study of the oxygen vacancy in $SrTiO_3$", *Model. Simul. Mater. Sc.* **9**(5), pp. 415 (2001).

[237] James P. Buban, Hakim Iddir, and Serdar Öğüt, "Structural and electronic properties of oxygen vacancies in cubic and antiferrodistortive phases of $SrTiO_3$", *Phys. Rev. B* **69**, pp. 180102 (2004).

[238] Euiyoung Choi, Joho Kim, D. Cuong, and Jaichan Lee, "Oxygen vacancies in $SrTiO_3$", In *2008 17th IEEE International Symposium on the Applications of Ferroelectrics* volume 1 , pp. 1–2 (2008).

[239] Paul C. McIntyre, "Equilibrium point defect and electronic carrier distributions near interfaces in acceptor-doped strontium titanate", *J. Am. Ceram. Soc.* **83** (2000).

[240] Roger A. De Souza, "The formation of equilibrium space-charge zones at grain boundaries in the perovskite oxide $SrTiO_3$", *Phys. Chem. Chem. Phys.* **11**, pp. 9939–9969 (2009).

[241] R. F. Klie, M. Beleggia, Y. Zhu, J. P. Buban, and N. D. Browning, "Atomic-scale model of the grain boundary potential in perovskite oxides", *Phys. Rev. B* **68**, pp. 214101 (2003).

[242] R. A. De Souza and R. Meyer, "Comment on "Atomic-scale model of the grain boundary potential in perovskite oxides"", *Phys. Rev. B* **72**, pp. 056101 (2005).

[243] M. Leonhardt, J. Jamnik, and J. Maier, "In situ monitoring and quantitative analysis of oxygen diffusion through Schottky-barriers in $SrTiO_3$ bicrystals", *Electrochem. Solid State Lett.* **2**, pp. 333–335 (1999).

[244] J. Jamnik, X. Guo, and J. Maier, "Field-induced relaxation of bulk composition due to internal boundaries", *Appl. Phys. Lett.* **82**, pp. 2820–2822 (2003).

[245] S Hutt, S Köstlmeier, and C Elsässer, "Density functional study of the $\Sigma 3$ (111) $[1\bar{1}0]$ symmetrical tilt grain boundary in $SrTiO_3$", *J. Phys.: Condens. Matter* **13**(18), pp. 3949 (2001).

[246] R Astala and P D Bristowe, "First-principles calculations of an oxygen deficient $\Sigma = 3(111)[10\bar{1}]$ grain boundary in strontium titanate", *J. Phys.: Condens. Matter* **14**(25), pp. 6455 (2002).

[247] K. J. Dudeck, N. A. Benedek, M. W. Finnis, and D. J. H. Cockayne, "Atomic-scale characterization of the $SrTiO_3$ Σ 3(112)[$\bar{1}$10] grain boundary", *Phys. Rev. B* **81**, pp. 134109 (2010).

[248] Blas P. Uberuaga, Samrat Choudhury, Xian-Ming Bai, and Nicole A. Benedek, "Grain boundary stoichiometry and interactions with defects in $SrTiO_3$", *Scr. Mater.* **66**, pp. 105 – 108 (2012).

[249] James A. Dawson and Isao Tanaka, "Local structure and energetics of Pr- and La-doped $SrTiO_3$ grain boundaries and the influence on coreshell structure formation", *J. Phys. Chem. C* **118**(44), pp. 25765–25778 (2014).

[250] D.A. Bonnell and I. Solomon, "Measurement of space charge adjacent to oxide grain boundaries by tunneling spectroscopy", *Ultramicroscopy* **42**, pp. 788 – 792 (1992).

[251] N. D. Browning, S. J. Pennycook, M. F. Chisholm, M. M. McGibbon, and A. J. McGibbon, "Observation of structural units at symmetric [001] tilt boundaries in $SrTiO_3$", *Interface Sci.* **2**(4), pp. 397–423 (1995).

[252] Hui Gu, M. Rühle, S. Stemmer, and Xuemin Pan, "Grain boundary structure and composition in strontium titanate", In *Intergranular and Interphase Boundaries in Materials* volume 207 of *Materials Science Forum* , pp. 421–424 (1996).

[253] Dawn A. Bonnell, "Local structure and properties of oxide surfaces: Scanning probe analyses of ceramics", *J. Am. Ceram. Soc.* **81**, pp. 3049–3070 (1998).

[254] M.M. McGibbon, N.D. Browning, A.J. McGibbon, M.F. Chisholm, and S.J. Pennycook, "Direct determination of grain boundary atomic structure in $SrTiO_3$", *MRS Proc.* **357** (1994).

[255] M. M. McGibbon, N. D. Browning, A. J. McGibbon, and S. J. Pennycook, "The atomic structure of asymmetric [001] tilt boundaries in $SrTiO_3$", *Philos. Mag. A* **73**, pp. 625–641 (1996).

[256] M. Imaeda, T. Mizoguchi, Y. Sato, H.-S. Lee, S. D. Findlay, N. Shibata, T. Yamamoto, and Y. Ikuhara, "Atomic structure, electronic structure, and defect energetics in $[001](310)\Sigma5$ grain boundaries of $SrTiO_3$ and $BaTiO_3$", *Phys. Rev. B* **78**, pp. 245320 (2008).

[257] Shang-Di Mo, W. Y. Ching, M. F. Chisholm, and G. Duscher, "Electronic structure of a grain-boundary model in $SrTiO_3$", *Phys. Rev. B* **60**, pp. 2416–2424 (1999).

[258] M. Nomura, N. Ichinose, K. Yamaji, H. Haneda, and J. Tanaka, "Structure simulation on twisted boundaries in $SrTiO_3$ bicrystals by molecular dynamics calculation", *J. Electroceram.* **4**, pp. 91–98 (1999).

[259] Masayuki Fujimoto, Yet-Ming Chiang, Alexana Roshko, and W. David Kingery, "Microstructure and electrical properties of sodium-diffused and potassium-diffused $SrTiO_3$ barrier-layer capacitors exhibiting varistor behavior", *J. Am. Ceram. Soc.* **68**, pp. C–300–C–303 (1985).

[260] Sung-Yoon Chung and Suk-Joong L. Kang, "Intergranular amorphous films and dislocations-promoted grain growth in $SrTiO_3$", *Acta Mater.* **51**(8), pp. 2345–2354 (2003).

[261] Roope K. Astala and Paul D. Bristowe, "The properties of a Na-doped twist boundary in $SrTiO_3$ from first principles", *MRS Proc.* **751**, pp. Z3.23.1–6 (2002).

[262] R Astala and P D Bristowe, "A computational study of twist boundary structures in strontium titanate", *J. Phys.: Condens. Matter* **14**, pp. 13635 (2002).

[263] Zhenpeng Hu and Horia Metiu, "Choice of U for DFT+U calculations for titanium oxides", *J. Phys. Chem. C* **115**(13), pp. 5841–5845 (2011).

[264] Paul Erhart, Andreas Klein, Daniel Åberg, and Babak Sadigh, "Efficacy of the DFT+U formalism for modeling hole polarons in perovskite oxides", *Phys. Rev. B* **90**, pp. 035204 (2014).

[265] Tridip Das, Jason D. Nicholas, and Yue Qi, "Long-range charge transfer and oxygen vacancy interactions in strontium ferrite", *J. Mater. Chem. A* **5**, pp. 4493–4506 (2017).

[266] Nazia Nafsin and Ricardo H.R. Castro, "Direct measurements of quasi-zero grain boundary energies in ceramics", *J. Mater. Res.* **32**, pp. 166173 (2017).

[267] Daniel A. Fumo, Jose R. Jurado, Ana M. Segades, and Jorge R. Frade, "Combustion synthesis of iron-substituted strontium titanate perovskites", *Mater. Res. Bull.* **32**(10), pp. 1459–1470 (1997).

[268] D. Lee, H. Lu, Y. Gu, S.-Y. Choi, S.-D. Li, S. Ryu, T. R. Paudel, K. Song, E. Mikheev, S. Lee, S. Stemmer, D. A. Tenne, S. H. Oh, E. Y. Tsymbal, X. Wu, L.-Q. Chen, A. Gruverman, and C. B. Eom, "Emergence of room-temperature ferroelectricity at reduced dimensions", *Science* **349**(6254), pp. 1314–1317 (2015).

[269] Ho Nyung Lee, Sung S. Ambrose Seo, Woo Seok Choi, and Christopher M. Rouleau, "Growth control of oxygen stoichiometry in homoepitaxial $SrTiO_3$ films by pulsed laser epitaxy in high vacuum", *Sci. Rep.* **6**, pp. 19941 (2016).

[270] Xue Li, Hailei Zhao, Wie Shen, Feng Gao, Xianliang Huang, Yue Li, and Zhiming Zhu, "Synthesis and properties of Y-doped $SrTiO_3$ as an anode material for SOFCs", *J. Power Sources* **166**, pp. 47–52 (2007).

[271] V. E. Loginov, A. V. Tumarkin, M. V. Sysa, O. U. Buslov, M. M. Gaidukov, A. I. Ivanov, and A. B. Kozyrev, "The influence of synthesis temperature on structure properties of $SrTiO_3$ ferroelectric films", *Integr. Ferroelectr.* **39**(1-4), pp. 375–381 (2001).

[272] Wattaka Sitaputra, Nikhil Sivadas, Marek Skowronski, Di Xiao, and Randall M. Feenstra, "Oxygen vacancies on SrO-terminated $SrTiO_3$ surfaces studied by scanning tunneling spectroscopy", *Phys. Rev. B* **91**, pp. 205408 (2015).

[273] Hisao Yamada and G.R. Miller, "Point defects in reduced strontium titanate", *J. Solid State Chem.* **6**(1), pp. 169–177 (1973).

[274] Yuki Yamaguchi, Yoshihiro Kanamaru, Minori Fukushima, Kenjiro Fujimoto, and Shigeru Ito, "Preparation of highly crystallized strontium titanate powders at room temperature", *J. Am. Ceram. Soc.* **98**, pp. 3054–3061 (2015).

[275] D. A. Johnson, *Metals and Chemical Change*, Royal Society of Chemistry (2002).

[276] I. D. Brown, *The Chemical Bond in Inorganic Chemistry: The Bond Valence Model*, International Union of Crystallography Monographs on Crystallography (Book 12). Oxford University Press (2006).

[277] Florian Voigts, Tanja Damjanovic, Gnter Borchardt, Christos Argirusis, and Wolfgang Maus-Friedrichs, "Synthesis and characterization of strontium titanate nanoparticles as potential high temperature oxygen sensor material", *J. Nanomat.* **2006**, pp. 1–6 (2006).

[278] R. C. Weast and M. J. Astle, *CRC Hand of Chemistry and Physics*, CRC Press, Boca Raton 60th edition (1979).

[279] Karsten Reuter and Matthias Scheffler, "Composition, structure, and stability of RuO_2 (110) as a function of oxygen pressure", *Phys. Rev. B* **65**, pp. 035406 (2001).

[280] J. Osorio-Guillén, S. Lany, S. V. Barabash, and A. Zunger, "Magnetism without magnetic ions: Percolation, exchange, and formation energies of magnetism-promoting intrinsic defects in CaO", *Phys. Rev. Lett.* **96**, pp. 107203 (2006).

[281] Sung-Yoon Chung, Suk-Joong L. Kang, and Vinayak P. Dravid, "Effect of sintering atmosphere on grain boundary segregation and grain growth in niobium-doped $SrTiO_3$", *J. Am. Ceram. Soc.* **85**, pp. 2805–2810 (2002).

[282] Zaoli Zhang, Wilfried Sigle, and Wolfgang Kurtz, "HRTEM and EELS study of screw dislocation cores in $SrTiO_3$", *Phys. Rev. B* **69**, pp. 144103 (2004).

[283] S.B. Lee, J.-H. Lee, P.-S. Cho, D.-Y. Kim, W. Sigle, and F. Phillipp, "High-temperature resistance anomaly at a strontium titanate grain boundary and its correlation with the grain-boundary faceting-defaceting transition", *Adv. Mater.* **19**, pp. 391–395 (2007).

[284] X.Q. Cao, R. Vassen, and D. Stoever, "Ceramic materials for thermal barrier coatings", *J. Eur. Ceram. Soc.* **24**(1) (2004).

[285] Robert L. Jones and Derek Mess, "Improved tetragonal phase stability at 1400°C with scandia, yttria-stabilized zirconia", *Surf. Coat. Technol.* **86-87**, pp. 94 – 101 (1996).

[286] R. W. Trice, Y. Jennifer Su, J. R. Mawdsley, K. T. Faber, A. R. De Arellano-López, Hsin Wang, and W. D. Porter, "Effect of heat treatment on phase stability, microstructure, and thermal conductivity of plasma-sprayed YSZ", *J. Mater. Sci.* **37**, pp. 2359–2365 (2002).

[287] James L. Smialek, "The chemistry of Saudi Arabian sand: A deposition problem on helicopter turbine airfoils", In *Gordon Conference on Corrosion* (1991), NASA Technical Memorandum 105234.

[288] R. L. Jones, "Some aspects of the hot corrosion of thermal barrier coatings", *J. Therm. Spray Techn.* **6**, pp. 77–84 (1997).

[289] R. Wellman, G. Whitman, and J.R. Nicholls, "CMAS corrosion of EB PVD TBCs: Identifying the minimum level to initiate damage", *Int. J. Refract. Met. Hard Mater.* **28**, pp. 124 – 132 (2010).

[290] F.H. Stott, D.J. de Wet, and R. Taylor, "Degradation of thermal-barrier coatings at very high temperatures", *MRS Bull.* **19**, pp. 4649 (1994).

[291] Stephan Krämer, James Yang, Carlos G. Levi, and Curtis A. Johnson, "Thermochemical interaction of thermal barrier coatings with molten CaO–MgO–Al_2O_3–SiO_2 (CMAS) deposits", *J. Am. Ceram. Soc.* **89**(10), pp. 3167–3175 (2006).

[292] Jing Wu, Hong-bo Guo, Yu-zhi Gao, and Sheng-kai Gong, "Microstructure and thermophysical properties of yttria stabilized zirconia coatings with CMAS deposits", *J. Eur. Ceram. Soc.* **31**, pp. 1881–1888 (2011).

[293] K. W. Schlichting, N. P. Padture, and P. G. Klemens, "Thermal conductivity of dense and porous yttria-stabilized zirconia", *J. Mater. Sci.* **36**, pp. 3003–3010 (2001).

[294] Alexandra Navrotsky, "Thermochemical insights into refractory ceramic materials based on oxides with large tetravalent cations", *J. Mater. Chem.* **15**, pp. 1883–1890 (2005).

[295] M.J. Stiger, N.M. Yanar, M.G. Topping, Fred Pettit, and Gerald Meier, "Thermal barrier coatings for the 21st century", *Zeitschrift fuer Metallkunde* **90**, pp. 1069–1078 (1999).

[296] Jong-Heun Lee, Toshiyuki Mori, Ji-Guang Li, Takayasu Ikegami, John Drennan, and Doh-Yeon Kim, "Scavenging of siliceous grain-boundary phase of 8-mol%-ytterbia-stabilized zirconia without additive", *J. Am. Ceram. Soc.* **84**, pp. 2734–2736 (2001).

[297] Giacomo Giorgi, Anatoli Korkin, and Koichi Yamashita, "Zirconium and hafnium oxide interface with silicon: Computational study of stress and strain effects", *Comp. Mater. Sci.* **43**, pp. 930 – 937 (2008).

[298] C. Mercer, S. Faulhaber, A.G. Evans, and R. Darolia, "A delamination mechanism for thermal barrier coatings subject to calciummagnesiumalumino-silicate (CMAS) infiltration", *Acta Mater.* **53**, pp. 1029 – 1039 (2005).

[299] Xi Chen, "Calciummagnesiumaluminasilicate (CMAS) delamination mechanisms in EB-PVD thermal barrier coatings", *Surf. Coat. Technol.* **200**, pp. 3418–3427 (2006).

[300] Guo Lei, Li Mingzhu, Cheng Yuxian, Zhang Chenglong, He Sixian, Zhang Yuchen, and Ye Fuxing, "Plasma sprayed nanostructured gdpo4 thermal barrier coatings: Preparation microstructure and CMAS corrosion resistance", *J. Am. Ceram. Soc.* **100**(9), pp. 4209–4218 (2017).

[301] R. Bürgel and I. Kvernes, *Thermal Barrier Coatings, High Temperature Alloys for Gas Turbines and Other Applications*, D. Reidel Publishing Co. (1986).

[302] Robert Vassen, Alexandra Stuke, and Detlev Stöver, "Recent developments in the field of thermal barrier coatings", *J. Therm. Spray Technol.* **18**, pp. 181–186 (2009).

[303] M Matsuda, J Nowotny, Z Zhang, and C.C Sorrell, "Lattice and grain boundary diffusion of Ca in polycrystalline yttria-stabilized ZrO_2 determined by employing SIMS technique", *Solid State Ionics* **111**, pp. 301 – 306 (1998).

[304] K. Kowalski, A. Bernasik, and A. Sadowski, "Diffusion of calcium in yttria stabilized zirconia ceramics", *J. Eur. Ceram. Soc.* **20**, pp. 2095–2100 (2000).

[305] Xin Guo, Chao-Qun Tang, and Run-Zhang Yuan, "Grain boundary ionic conduction in zirconia-based solid electrolyte with alumina addition", *J. Eur. Ceram. Soc.* **15**, pp. 25 – 32 (1995).

[306] Makoto Aoki, YetMing Chiang, Igor Kosacki, L. JongRen Lee, Harry Tuller, and Yaping Liu, "Solute segregation and grainboundary impedance in highpurity stabilized zirconia", *J. Am. Ceram. Soc.* **79**, pp. 1169–1180 (1996).

[307] Y. Oishi and H. Ichimura, "Grainboundary enhanced interdiffusion in polycrystalline CaOstabilized zirconia system", *TheJ. Chem. Phys.* **71**, pp. 5134–5139 (1979).

[308] E.D. Hondros and M.P. Seah, "Grain boundary activity measurements by auger electron spectroscopy", *Scripta Metall. Mater.* **6**(10), pp. 1007 – 1012 (1972).

[309] M. P. Seah and E. D. Hondros, "Grain boundary segregation", *P. Roy. Soc. Lond. A Mat.* **335**(1601), pp. 191–212 (1973).

[310] C. L. Briant, "On the chemistry of grain boundary segregation and grain boundary fracture", *Metall. Trans. A* **21**, pp. 2339–2354 (1990).

[311] Hark B. Lee, Friedrich B. Prinz, and Wei Cai, "Atomistic simulations of grain boundary segregation in nanocrystalline yttria-stabilized zirconia and gadolinia-doped ceria solid oxide electrolytes", *Acta Mater.* **61**, pp. 3872 – 3887 (2013).

[312] Jihwan An, Joong Sun Park, Ai Lee Koh, Hark B. Lee, Joop Schoonman, Robert Sinclair, Turgut M. Gür, and Fritz B Prinz, "Atomic scale verification of oxide-ion vacancy distribution near a single grain boundary in YSZ", *Sci. Rep.* **3**, pp. 2680 (2013).

[313] A. Predith, G. Ceder, C. Wolverton, K. Persson, and T. Mueller, "*Ab initio* prediction of ordered ground-state structures in ZrO_2-Y_2O_3", *Phys. Rev. B* **77**, pp. 144104 (2008).

[314] Cotton F. A., Wilkinson G., Mutillo C. A., and Bochmann M., *Advanced Inorganic Chemistry, 6th Edition*, Wiley-Interscience (2000).

[315] Robert Ruh and Peter W. R. Corfield, "Crystal structure of monoclinic hafnia and comparison with monoclinic zirconia", *J. Am. Ceram. Soc.* **53**, pp. 126–129 (1970).

[316] Xinyuan Zhao and David Vanderbilt, "First-principles study of structural, vibrational, and lattice dielectric properties of hafnium oxide", *Phys. Rev. B* **65**, pp. 233106 (2002).

[317] I. A. El-Shanshoury, V. A. Rudenko, and I. A. Ibrahim, "Polymorphic behavior of thin evaporated films of zirconium and hafnium oxides", *J. Am. Ceram. Soc.* **53**, pp. 264–268 (1970).

[318] K. Parlinski, Z. Q. Li, and Y. Kawazoe, "First-principles determination of the soft mode in cubic ZrO_2", *Phys. Rev. Lett.* **78**, pp. 4063–4066 (1997).

[319] K.-H. Xue, P. Blaise, L. R. C. Fonseca, G. Molas, E. Vianello, B. Traore, B. De Salvo, G. Ghibaudo, and Y. Nishi, "Grain boundary composition and conduction in HfO_2: An ab initio study", *Appl. Phys. Lett.* **102**, pp. 201908 (2013).

[320] G. M. Wolten, "Diffusionless phase transformations in zirconia and hafnia", *J. Am. Ceram. Soc.* **46**, pp. 418–422 (1963).

[321] Craig A.J Fisher and Hideaki Matsubara, "Molecular dynamics investigations of grain boundary phenomena in cubic zirconia", *Comput. Mater. Sci* **14**, pp. 177 – 184 (1999).

[322] Shannon R. D., "Revised effective ionic radii and systematic studies of interatomic distances in halides and chalcogenides", *Acta Crystallogr.* **A32**, pp. 751–767 (1976).

[323] Boutz Michel M. R., Chen Chu Sheng, Winnubst Louis, and Burggraaf Anthonie J., "Characterization of grain boundaries in superplastically deformed Y-TZP ceramics", *J. Am. Ceram. Soc.* **77**, pp. 2632–2640 (1994).

[324] Langmuir Irving, "The adsorption of gases on plane surfaces of glass, mica and platinum", *J. Am. Chem. Soc.* **40 (9)**, pp. 1361–1403 (1918).

[325] McLean Donald, *Grain boundaries in metals*, Oxford University Press (1957).

[326] Maziar Behtash, Yaqin Wang, Jian Luo, and Kesong Yang, "Oxygen vacancy formation in the $SrTiO_3$ $\Sigma 5$ [001] twist grain boundary from firstprinciples", *J. Am. Ceram. Soc.* **0**, pp. 1–12 (2018).

[327] Jianli Cheng, Jian Luo, and Kesong Yang, "Aimsgb: An algorithm and open-source python library to generate periodic grain boundary structures", *submitted* (2018).

[328] C. R. A. Catlow, A. V. Chadwick, G. N. Greaves, and L. M. Moroney, "EXAFS study of yttriastabilized zirconia", *J. Am. Ceram. Soc.* **69**, pp. 272–277 (1986).

[329] M.H. Tuilier, J. Dexpert-Ghys, H. Dexpert, and P. Lagarde, "X-ray absorption study of the ZrO_2-Y_2O_3 system", *J. Solid State Chem.* **69**, pp. 153–161 (1987).

[330] Zugang Mao, Susan B. Sinnott, and Elizabeth C. Dickey, "Ab initio calculations of pristine and doped zirconia σ5 (310)/[001] tilt grain boundaries", *J. Am. Ceram. Soc.* **85**(6), pp. 1594–1600 (2002).

[331] K. Kowalski, A. Bernasik, and A. Sadowski, "Bulk and grain boundary diffusion of titanium in yttria-stabilized zirconia", *J. Eur. Ceram. Soc.* **20**, pp. 951 – 958 (2000).

[332] Simona Somacescu, Jose Maria Calderon Moreno, Petre Osiceanu, Bao-Lian Su, and Viorica Parvulescu, "Single-phase solid solution (TiO_2)x-(YSZ)1-x mesoporous nanoparticles with catalytic activity in the oxidation of methane", *J. Phys. Chem. C* **114**, pp. 19365–19372 (2010).